

Birgit Krenn, BSc.

Bifunctional NiCo₂O₄-spinel as catalyst for rechargeable zinc-air redox flow batteries in alkaline and neutral media

MASTER´S THESIS

to achieve the university degree of
Diplom-Ingenieurin

Master´s degree programme: Technical Chemistry

submitted to

Graz University of Technology

Ass. Prof. Dipl.-Ing. Dr. techn. Waltraud Taucher-Mautner

Institute for Chemistry and Technology of Materials

Graz, October 2017

AFFIDAVIT

I declare that I have authored this thesis independently, that I have not used other than the declared sources/resources, and that I have explicitly indicated all material which has been quoted either literally or by content from the sources used. The text document uploaded to TUGRAZonline is identical to the present master's thesis.

20th October 2017

A handwritten signature in black ink that reads "Birgit Kun". The signature is written in a cursive style with a long horizontal stroke at the end.

Acknowledgments

First and foremost, I would like to thank Waltraud Taucher-Mautner. She gave me the freedom for my independence, but whenever I needed she had a good advice for me.

Thank you for the great time!

I would also thank Bernhard Gollas for his support during my thesis as well as Brigitte Bitschnau and Franz Mautner for the XRD measurements. Bernhard Berner, Richard Hueber, Christan Zelger were always ready to help me, especially Daniel Schloffer, thank you!

Last but not least I would like to thank my family and friends for their support during my whole studies.

Zusammenfassung

Ziel dieser Masterarbeit ist die Untersuchung von bifunktionellen NiCo_2O_4 -Spinellen hinsichtlich ihrer katalytischen Eigenschaften in alkalischen und neutralen Medien für die Verwendbarkeit als Katalysator in Lufterlektroden von wiederaufladbaren Zink-Luft-Redox-Fließbatterien. Die verschiedenen bifunktionellen NiCo_2O_4 -Katalysatoren werden mit zwei unterschiedlichen Methoden (Nitrat- und Hydroxidmethode) und bei verschiedenen Kalzinierungsbedingungen hergestellt. Die elektrochemischen Eigenschaften dieser Katalysatoren werden in stark konzentrierter Kalilauge und in neutralen Cholin-Elektrolyten untersucht. Es werden drei unterschiedliche Cholin-Elektrolyte hergestellt: Cholin-Acetat, Cholin-Sulfat und Cholin-Carbonat. Die Oxidationsstufenänderung des Nickels und des Kobalts im Spinell wird mittels zyklischer Voltammetrie bestimmt. Die katalytische Wirkung der Spinelle bezüglich der Sauerstoffentwicklungs- (OER) und Sauerstoffreduktionsreaktion (ORR) wird mittels rotierender Scheibenelektrode untersucht. Außerdem wird der Anteil an Peroxid, der während der ORR in Kalilauge und Cholin-Acetat entsteht, bestimmt. Zusätzlich werden die NiCo_2O_4 -Katalysatoren auf ihre physikalisch-chemischen Eigenschaften bezüglich Kristallstruktur, spezifischer Oberfläche, Partikelgröße, Partikelgrößenverteilung, Morphologie und Homogenität untersucht.

Die Experimente der OER in Kaliumhydroxid haben gezeigt, dass die mit der Hydroxidmethode hergestellten Katalysatoren eine niedrigere Überspannung für die Sauerstoffentwicklung haben. Die Katalysatoren des Nitratverfahrens zeigen höhere Grenzstromdichten für die ORR, aber kein Katalysator hatte eine eindeutig bessere katalytische Aktivität als alle anderen. Die Überspannung für die OER war in den Cholin-Elektrolyten deutlich höher als in Kaliumhydroxid. Das niedrigste Potential wurde in Cholin-Carbonat gemessen. Die Untersuchungen der ORR in den neutralen Elektrolyten zeigten in Cholin-Acetat die höchsten Stromdichten im Vergleich zur unbeschichteten Elektrode. Die Menge an gebildetem Peroxid war in 8 M KOH größer als in Cholin-Acetat. Die XRD-Messungen zeigten, dass alle NiCo_2O_4 -Katalysatorproben eine Spinellstruktur haben. Die BET-Bestimmung ergab die höchsten spezifischen Oberflächen für die Proben der Hydroxidmethode. Die Partikelgrößenverteilungsmessungen zeigten eine polydisperse Verteilung für Proben der Nitratmethode und eine monodisperse Verteilung für Proben der Hydroxidmethode. Die REM-Bilder haben gezeigt, dass Katalysatoren der

Nitratmethode kleinere kugelförmige Partikel haben und dass die der Hydroxidmethode größere plattenförmige Agglomerate aufweisen.

Abstract

The aim of this master thesis is the investigation of bifunctional NiCo_2O_4 spinels concerning their catalytic properties in alkaline and neutral media for the usability as catalyst in air electrodes of rechargeable zinc-air redox flow batteries. The synthesis of the different bifunctional NiCo_2O_4 spinel catalysts is done with two different methods, the nitrate and hydroxide method, under different calcination conditions. The electrochemical properties of these catalysts are investigated in highly concentrated potassium hydroxide solution and in neutral choline electrolytes. Three different neutral choline electrolytes are prepared: choline acetate, choline sulphate and choline carbonate. The transition of the oxidation states of nickel and cobalt in the spinels are determined with cyclic voltammetry. The catalytic activity of the spinels for the oxygen evolution reaction (OER) and the oxygen reduction reaction (ORR) are investigated with a rotating disc electrode. Furthermore, the amount of peroxide formed during the ORR in potassium hydroxide and choline acetate is determined. In addition, the physicochemical properties of NiCo_2O_4 catalysts regarding their crystal structure, specific surface area, particle size, particle size distribution, morphology and homogeneity were also examined.

The experiments of OER in potassium hydroxide have shown that the catalysts prepared with the hydroxide method have a lower overvoltage. The catalysts of the nitrate method show higher limiting current densities for the ORR, but no particular catalyst could be determined to exhibit better catalytic activity than all others. The overvoltage for the OER was considerably higher in the choline electrolytes than in potassium hydroxide. The lowest overvoltage was yielded in choline carbonate. The studies of ORR in the neutral electrolytes showed the highest current densities in comparison to the uncoated RDE in choline acetate. The amount of formed peroxide was higher in 8 M KOH than in choline acetate. The XRD measurements showed that all NiCo_2O_4 catalyst samples have a spinel structure. The results of the BET measurements illustrated the highest specific surface area for samples of the hydroxide method. The particle size distribution measurements showed a

polydisperse distribution for samples of the nitrate method and a monodisperse distribution of the samples of the hydroxide method. The SEM images have shown that catalysts of the nitrate method have smaller spherical particles and samples of the hydroxide method exhibit larger plate-shaped agglomerates.

Table of contents

1	Introduction	1
2	Theory.....	3
2.1	Redox flow battery.....	3
2.2	Zinc-air redox flow battery	4
2.2.1	Zinc electrode	5
2.2.2	Air electrode.....	6
2.2.3	Electrolyte	7
2.3	Oxygen reduction reaction and oxygen evolution reaction	7
2.4	Electrochemical methods	9
2.4.1	Cyclic voltammetry.....	9
2.4.2	Rotating disc electrode	12
2.4.2.1	Koutecky-Levich analysis	13
2.4.3	Rotating ring-disc electrode	15
2.4.3.1	Collection efficiency.....	16
2.4.3.2	Peroxide Formation	16
2.5	Physicochemical measurements	17
2.5.1	X-ray diffractometry.....	17
2.5.2	Specific surface area - Brunauer, Emmett, Teller method	19
2.5.3	Particle size distribution	22
2.5.4	Scanning electron microscopy	23
2.6	Spinel	25
3	Experimental	26
3.1	Catalyst preparation	26
3.1.1	Nitrate method	26
3.1.2	Hydroxide method.....	27
3.2	Preparation of the neutral electrolytes	28
3.2.1	Choline acetate	29
3.2.2	Choline sulphate	29
3.2.3	Choline carbonate.....	29
3.3	Electrochemical characterisation.....	30

3.3.1	Catalyst slurry preparation and application to the electrode	30
3.3.2	Cyclic voltammetry and rotating disc electrode experiment	30
3.3.3	Rotating ring-disc electrode experiment.....	31
3.3.3.1	Collection efficiency.....	31
3.3.3.2	Detection of peroxide formation.....	32
3.4	Physicochemical characterisations.....	33
3.4.1	X-ray diffractometry.....	33
3.4.2	BET measurements - specific surface area	33
3.4.3	Particle size distribution measurements.....	34
3.4.4	Scanning electron microscopy	34
4	Results and discussion.....	35
4.1	Electrochemical measurements - rotating disc electrode	35
4.1.1	Cyclic voltammetry in 8 M KOH	35
4.1.2	Cyclic voltammetry in C-OAc, C-SO ₄ and C-CO ₃	40
4.1.3	ORR and OER in 8 M KOH.....	41
4.1.4	Koutecky-Levich analysis.....	47
4.1.5	ORR and OER in C-OAc, C-SO ₄ and C-CO ₃	48
4.2	Electrochemical measurements – rotating ring-disc electrode	51
4.2.1	Collection efficiency	51
4.2.2	Peroxide detection	53
4.3	Physicochemical characterisations.....	57
4.3.1	XRD measurements.....	57
4.3.2	BET measurements	59
4.3.3	Particle size distribution	61
4.3.4	Scanning electron microscopy	64
5	Summary.....	66
6	References.....	69
7	Chemicals	73
8	List of symbols and abbreviations	74
9	List of figures.....	76
10	List of tables.....	80

1 Introduction

The energy use and electricity consumption have increased worldwide rapidly in the last few decades. The two main reasons for this are the rapid growth of the world population and the variation of the consumer habits. The negative effects of the high demand for energy are depletion of fossil fuels reserves, climate change, global warming, ozone layer depletion, etc. These are all reasons for development of energy storage and conversion systems to use energy from renewable sources for electromobility, grids, and power delivery systems. Renewable energy sources are, for example, solar energy, wind energy, biomass, ocean, wave energy, and thermal springs [1,2].

Energy storage is fundamental for the integration of renewable sources into the electricity system. The power grid has profits with higher efficiency and cost-effectiveness from the integration of an energy storage system. Problems of the electrical energy system such as the supply at peak demand can be solved by grid energy storage. There are different types of energy storage technologies: mechanical systems, electrochemical energy storage, electromagnetic systems and liquid storage. Their individual characteristics make them suitable for different applications. Electrochemical energy storage, such as fuel cells, batteries and supercapacitors, are one of the oldest and widely used storage technology systems [3].

Redox flow batteries (RFBs) are one of the latest technologies of electrochemical systems and provide properties to be a good assistant for electricity generation from renewable sources. The main attractive features are: fast responsiveness, high depth of discharge, scalability and flexibility, long durability, independent sizing of power and energy and reduced environmental impact. RFBs are based on the conversion of electrochemical energy from a redox couple into electric energy. The ions of the couple are in liquid form in solution, which are stored in external tanks [4].

The zinc-air redox flow battery has the design of a hybrid flow cell with the difference of having only one single tank. The main compounds of such batteries are: an air electrode with a catalyst on a gas diffusion layer (positive electrode), a zinc electrode (negative electrode), an alkaline electrolyte and a separator. Electricity can be generated by the electrochemical reaction of the zinc metal with oxygen from the air in the presence of an alkaline electrolyte. The zinc-air RFB is an attractive candidate

as a future energy storage system: the reactant oxygen is taken from the ambient air and does not have to be stored, zinc is safe, has low costs and a high capacity. The main challenges of the zinc-air RFB are: to find a catalyst, which is able to accelerate oxygen redox reactions at the air electrode, to avoid carbonation of the electrolyte, to prevent dendrite formation and shape change of the zinc electrode [5].

In this master thesis bifunctional NiCo_2O_4 spinels are studied concerning their catalytic properties to be an attractive candidate as catalyst for air electrodes in rechargeable zinc-air redox flow batteries. The investigations are performed in concentrated potassium hydroxide (KOH) solution as well as in neutral choline based electrolytes. The usage of KOH as electrolyte in zinc-air RFB has the disadvantage of carbonation due to the presence of carbon dioxide in the air. Consequently, carbonates are formed and block the pores of the electrode and the air diffusion path. For this reason, new electrolytes were studied. Three different choline electrolytes are investigated: choline acetate, choline sulphate and choline carbonate. Choline based electrolytes were chosen because of good results of zinc deposition of previous investigations [6].

The electrochemical and physicochemical properties of a catalyst have an influence on their catalytic behaviour. Therefore, in this master thesis different catalysts are prepared and several electrochemical and physicochemical measurements are performed to get an overview of their suitability as catalyst for zinc-air redox flow batteries. The different NiCo_2O_4 catalysts are prepared with two different methods: the nitrate and hydroxide method. These catalysts are investigated concerning their catalytic activity for the oxygen evolution reaction (OER) and oxygen reduction reaction (ORR). Experiments for the determination of the amount of peroxide formed during the ORR are also carried out. In addition, the crystal structure is investigated via XRD measurements. The specific surface area is determined with the BET-method and also the particle size distribution is specified. SEM images are recorded to illustrate the morphology, the homogeneity and the particle size of the different catalysts.

2 Theory

2.1 Redox flow battery

The redox flow battery (RFB) is a rechargeable battery where a liquid electrolyte with a dissolved redox couple is used as an active material for energy storage. Such batteries have two different electrolytes, a positive electrolyte (catholyte) and a negative electrolyte (analyte), which are stored in external tanks. The electrolytes are continuously pumped from the tanks through a porous electrode into the electrochemical cell ("stack"). The stack consists of two electrodes respectively two half-cells with a separator between. The separator is an ion exchange membrane, which enables on one hand the ionic transfer between the two half-cells and prevents the mixing of the analyte and the catholyte on the other hand. In the RFB the power and energy can be separated. The power of the battery depends on the number of cells in the stack while the ability of energy storage is determined by the concentration and volume of the electrolytes. This separation makes the RFB suitable for different energy storage applications [7,8]. The principle design of a RFB is shown in Figure 1.

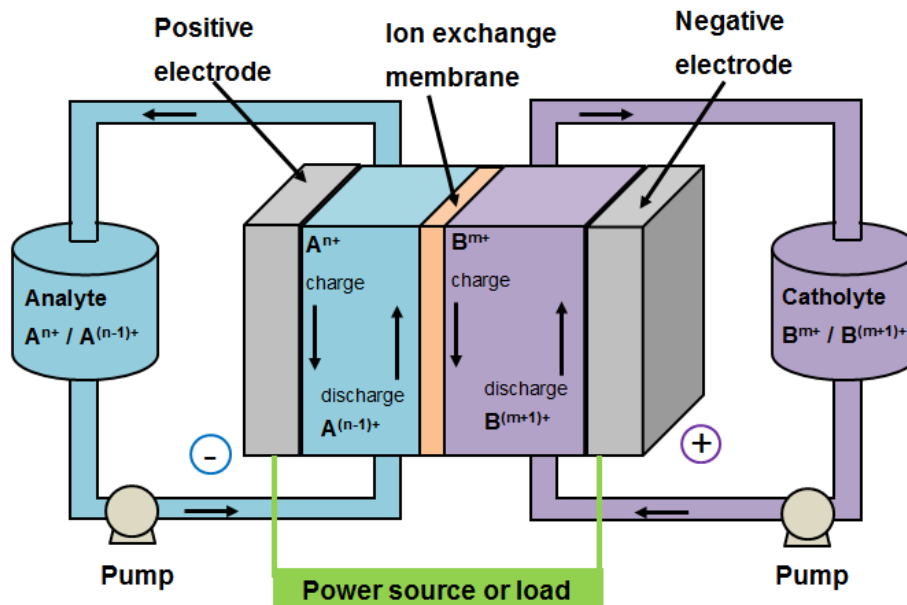


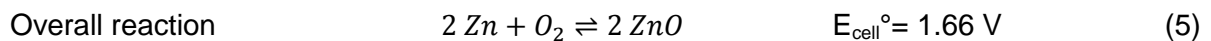
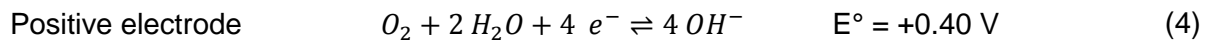
Figure 1: Principle design of a redox flow battery [8].

2.2 Zinc-air redox flow battery

The design of a zinc-air redox flow battery is similar to that of hybrid flow cells, with the difference of having only one electrolyte tank. The negative electrode of the battery is zinc and the positive electrode is a gas diffusion electrode (GDE) with a catalytic active layer. The electrolyte of this RFB is in most cases an alkaline one, e.g. potassium hydroxide (KOH). Both electrodes are connected to current collectors, respectively. During the discharging process the zinc from the anode is oxidized to zinc ions (Zn^{2+}), while on the cathode the oxygen from the ambient air is reduced to form hydroxide ions (OH^-) (oxygen reduction reaction (ORR)). The OH^- migrates to the zinc electrode and forms zincate ions ($Zn(OH)_4^{2-}$). In the reverse process the oxygen is evolved on the positive electrode (oxygen evolution reaction (OER)) and zinc is deposited on the negative electrode. If the electrolyte is supersaturated with $Zn(OH)_4^{2-}$, insoluble zinc oxide (ZnO) is formed [5,9]. The catalyst of the oxygen electrode must enable both reactions, the OER and the ORR. If one catalyst is able to accelerate both reactions it is bifunctional [10]. The electrochemical reactions of a zinc-air RFB with alkaline electrolyte are shown below in equation (2)-(5). Figure 2 illustrates the schematic of a zinc-air redox flow battery. The theoretical voltage of such a cell is calculated by the difference of the standard electrode potentials as follows [5]:

$$E_{cathode}^{\circ} - E_{anode}^{\circ} = E_{cell}^{\circ} \quad (1)$$

$$0.40 \text{ V} - (-1.26 \text{ V}) = 1.66 \text{ V}$$



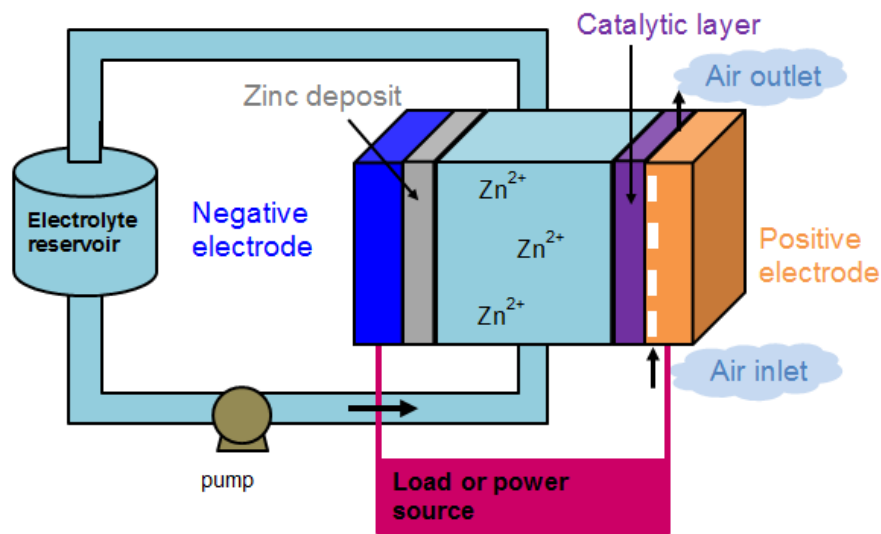


Figure 2: A schematic diagram of a zinc-air redox flow battery [6].

2.2.1 Zinc electrode

Zinc has several properties that make it suitable to utilise it as electrode material. The metal is relatively stable in alkaline solutions and it has a low electrical resistivity ($5.96 \mu\Omega$) [10,11]. Furthermore, the corrosion of zinc in alkaline media is low. Also the low cost and toxicity, the easy handling and availability, as well as the high specific energy are reasons for the usage [11,12]. Despite the positive sides there are also some negative one. The formation of dendrites (Figure 3, a) happens during electrodeposition under certain conditions. The dendrites can break from the electrode and result in loss of capacity. They can also grow as large as they break through the separator and reach the positive electrode and thus cause a short circuit. Another phenomenon that influences the performance of the zinc electrode is the so called shape change (Figure 3, b). During the discharging/charging process the zinc is dissolved and deposited. The deposition takes place at different locations on the zinc electrode and thus several charge/discharge cycles lead to densification of the electrode and to a loss of capacity. The hydrogen evolution (Figure 3, d) and associated corrosion of the electrode presents a further challenge.

Hydrogen is evolved because the standard reduction potential at pH 14 is lower (-0.83 V vs. standard hydrogen electrode (SHE)) than that of Zn/ZnO (-1.26 V vs. SHE). Passivation (Figure 3, c) and internal resistance is also a critical topic of the zinc electrode. Passivation means that the surface of the electrode is blocked by an insulating layer and thus prevents the movement of the discharging product.

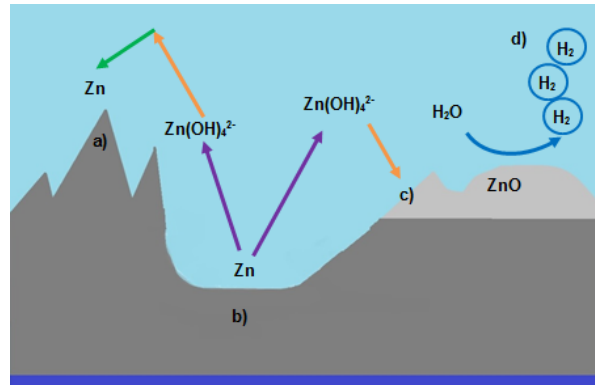


Figure 3: Illustration of the troubles of the zinc electrode: a) dendrite formation, b) shape change, c) passivation and, d) hydrogen evolution [5].

During the discharging process, Zn(OH)_4^{2-} is formed and when the solubility limit of zincate in the electrolyte is reached, ZnO is precipitated on the surface of the zinc electrode. The ZnO precipitate reduces the pore size of the electrode and passivates the zinc. ZnO is nonconductive and so the internal resistance of the zinc electrode is increased and this results in increased voltage during charging and voltage losses during discharging [5].

2.2.2 Air electrode

The air electrode of a zinc-air RFB is an important component that determines the power density of the battery. The electrode is usually composed of a hydrophobic gas diffusion layer (GDL), a hydrophilic catalytic layer and a current collector. The hydrophobic property of the GDL is important to avoid electrode flooding. The ORR occurs at the three-phase interface between the gaseous O_2 , the liquid electrolyte and the solid catalyst. The OER occurs at the two-phase reaction zone between the liquid electrolyte and the solid catalyst. During the ORR the oxygen and electrolyte must have the possibility to enter into the reaction zone. This causes the slow penetration of the GDL with electrolyte and flooding of the electrode. This problem can be avoided by a hydrophobic character of the gas diffusion layer [5,12].

The catalyst of the electrode must enhance the ORR and OER and both reactions have a high overpotential. For example, platinum is the best catalyst for the oxygen reduction but is poor in the evolution reaction because of the formation of a low

electrically conductive stable oxide layer on the surface at the positive potential during OER. Therefore, a bifunctional oxygen catalyst or the combination of catalysts are needed to solve this problem. Unfortunately, the perfect material is not prepared yet but active research is ongoing [5,9,10].

2.2.3 Electrolyte

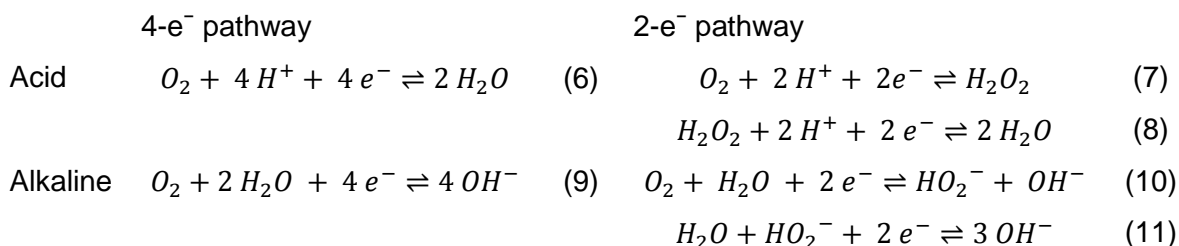
The most popular electrolyte in zinc-air batteries is potassium hydroxide. Benefits of 30wt% KOH in comparison with sodium hydroxide (NaOH) are higher ionic conductivity, maximum of $\text{Zn}(\text{OH})_4^{2-}$ solubility, lower viscosity, and higher oxygen solubility. Concentrated KOH shows also low H_2 evolution and thus minimised zinc corrosion [5,9,10]. However, there are also problems by using aqueous alkaline electrolyte in zinc-air RFBs. The performance of the battery under atmospheric conditions leads to the carbonation of the electrolyte due to the presence of carbon dioxide (CO_2) in the air. Consequently, the conductivity of the air electrode is reduced by the precipitation of the formed carbonates in the pores of the electrode. This induces also the blocking of the air diffusion path. Using ionic liquids as electrolyte shows the benefits of avoiding carbonation, zinc corrosion, and electrolyte evaporation. The research for the utilization as electrolyte is only at the beginning and an acceptable one is not yet found [5].

2.3 Oxygen reduction reaction and oxygen evolution reaction

The air electrode of a rechargeable zinc-air battery, where oxygen reduction reaction and oxygen evolution reaction takes place, can be bifunctional. During the discharging process, O_2 molecules are reduced and the metal is oxidised and vice versa during the charging process. Also in other renewable energy storage and conversion systems such as fuel cells, water splitting, and other metal-air batteries, the performance of both reactions is important. The research of catalysts for oxygen chemistry and understanding the mechanism of OER and ORR is an important topic in the field of electrochemical energy conversion and storage systems. Especially,

the catalysis of ORR is essential due to the fact that the oxygen reduction reaction is sluggish in nature [13-15].

The ORR pathways in aqueous acidic and alkaline solutions can result from a four-electron reduction or a two-electron reduction [16]:



There are different possible scenarios of O₂ adsorption on the active sites of a catalyst (Figure 4). The surface geometry (crystallographic structure) and the binding energy are determining the way how the oxygen adsorbs. The pathway of the ORR is influenced by the oxygen adsorption configurations and the oxygen surface interactions. In the case of the end-on (Figure 4 a, b) coordinated O atom to the catalyst surface, a one electron transfer is favoured and so the 2e⁻ pathway with peroxide generation. On the other hand, the direct 4-e⁻ ORR pathway without peroxide formation is preferred when two O atoms are adsorbed and coordinated at the surface of the catalyst (Figure 4 c, d) [17].

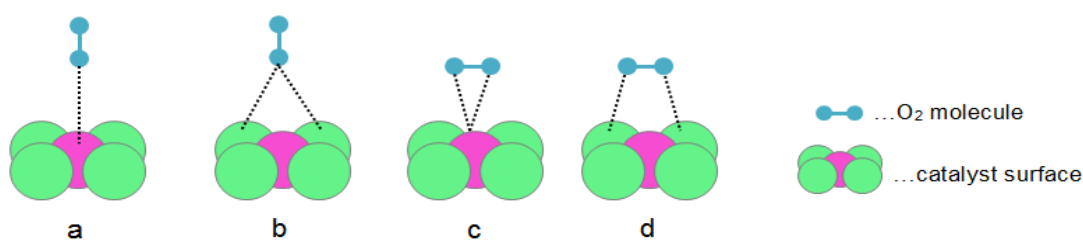


Figure 4: Schematic of four different possibilities of the adsorption of O₂ (blue) on catalyst surfaces: a) on-top end-on, b) bridge end-on, c) bridge side-on one site, and d) bridge side-on two sites [17].

2.4 Electrochemical methods

2.4.1 Cyclic voltammetry

Cyclic voltammetry is an investigation method to characterize electrochemical processes at the interface between electrode and electrolyte. The potential of the electrode is changed with a constant rate between two turning points (Figure 5). The turning points are typically the decomposition potential of the solvent, in the case of water between the oxygen and the hydrogen evolution [18,19]. The measurement is carried out in a three electrode configuration with a working electrode (WE), a counter electrode (CE) and a reference electrode (RE). The voltage is changing continuously over time and this course has a triangular shape and therefore, the technique is also called triangular voltage method. The potential against the RE is recorded. The measured electrode potential and the current give a diagram, the so called cyclic voltammogram (CV) (Figure 7). Cyclic voltammetry is typically used for the investigations of metal deposition and redox systems [19]. In the linear sweep voltammetry (LSV) the potential of the electrode proceeds from a start value to positive or negative direction and stops then (Figure 6) [20].

For the interpretation of CVs, the peak current of the forward scan (anodic peak) and the reverse scan (cathodic peak) and the corresponding two peak potentials are important parameters. For a reversible couple the peak current is expressed by the Randles–Sevcik equation:

$$i_p = (2.69 * 10^5)n^{3/2}ACD^{1/2}\nu^{1/2} \quad (12)$$

with

i_p ...Peak current / A

n ...Number of transferred electrons

A ...Area of electrode / cm²

C ...Concentration / mol cm⁻³

D ...Diffusion coefficient / cm² s⁻¹

ν ...Scan rate / V s⁻¹

Therefore, the peak current of a reversible system increases with the square root of the scan rate, which indicates that the electrode reaction is controlled by mass transport. The peak current is also directly proportional to the concentration. The peak current ratio of the anodic to the cathodic peak is unity for a simple reversible redox couple. The separation of the anodic and the cathodic peak potentials for a reversible system is given by

$$\Delta E_p = E_{p,a} - E_{p,c} = \frac{0.059}{n} V \quad (13)$$

with

ΔE_p ...Separation potential / V

$E_{p,a}$...Anodic peak potential / V

$E_{p,c}$...Cathodic peak potential / V

n ...Number of transferred electrons

For a fast one-electron process ΔE_p is about 59 mV and the anodic and the cathodic peak potential are not depending on the scan rate.

In the case of sluggish electron transfer processes (irreversible process), the different peaks of the CV are widely separated and have reduced peak size (graph A in Figure 8). In a totally irreversible system, the peak potential is shifted with the scan rate. In the CV of a quasi-reversible system (graph B in Figure 8), the separation in peak potentials is larger than in reversible systems. At high values of the scan rate, the behaviour of the system is like an irreversible one and at a slower scan rate it behaves like a reversible system [21].

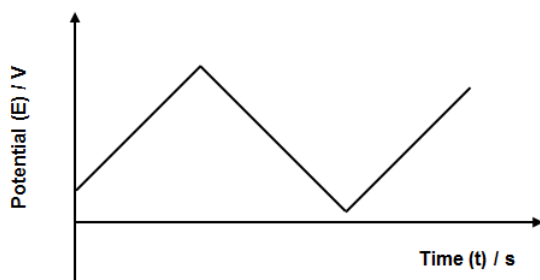


Figure 5: Schematic of the potential course of a CV [19].

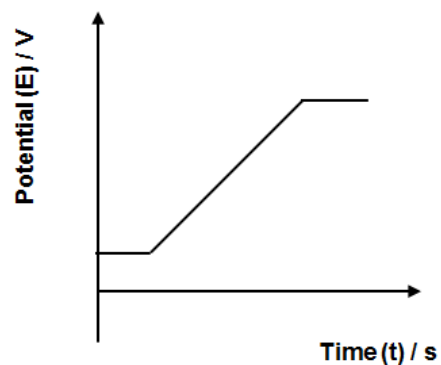


Figure 6: Schematic of potential course of LSV [20].

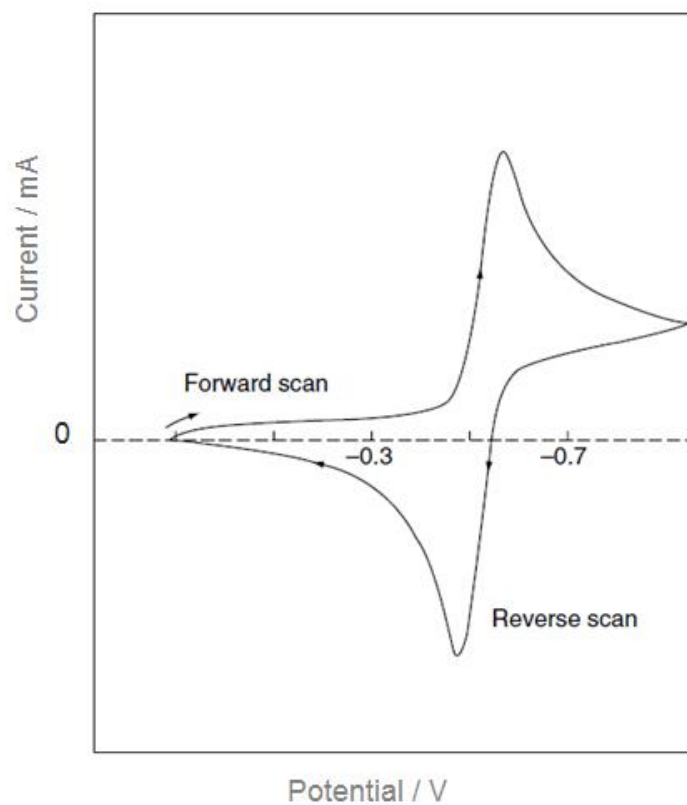


Figure 7: Illustration of a cyclic voltammogram [21].

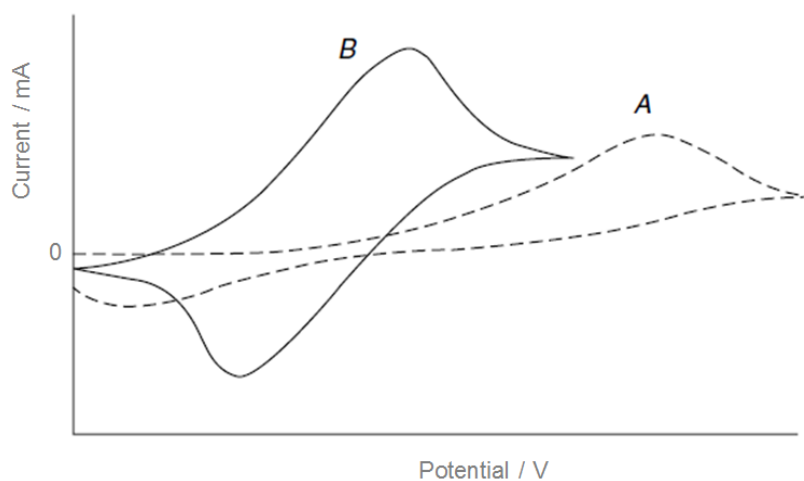


Figure 8: Illustration of a cyclic voltammogram of an irreversible (graph A) and a quasi-reversible (graph B) redox process [21].

2.4.2 Rotating disc electrode

A rotating disc electrode (RDE) consists of a disc with a certain diameter surrounded by an insulating coat. Experiments with RDE's are a widely used tool to investigate electrochemical reactions to determine stoichiometric number of electron transferred, diffusion coefficients of electroactive species, mass transfer and kinetic parameter. During the performance, the rotation of the RDE leads to the flow of the electrolyte in vertical direction to the surface of the disk and then throwing it outward (illustration shown in Figure 9) in a radial direction [22-24].

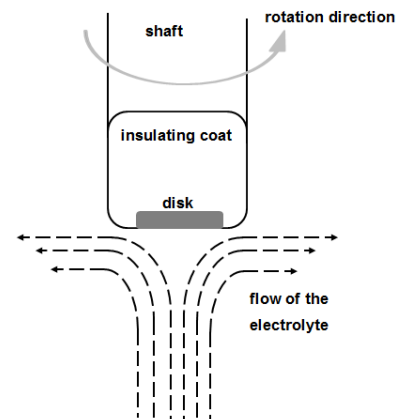


Figure 9: Schematic of the RDE [22].

Thus, two regions of the electrolyte are created according to the Nernst diffusion layer model:

- 1) The first zone has the thickness δ . This area is close to the surface of the RDE. Here the mass transport is the only diffusion due to the assumption of a totally stagnant layer.
- 2) In the second region strong convection arises and the concentration of all species is constant. This area is outside of the first zone [22].

The thickness δ can be expressed as:

$$\delta = 1.6 * \nu^{0.166} * D^{0.33} \omega^{-0.5} \quad (14)$$

with

ν ...Viscosity of the electrolyte / $\text{m}^2 \text{s}^{-1}$

D ...Diffusion coefficient / $\text{m}^2 \text{s}^{-1}$

ω ...Rotation speed of the electrode / rad s^{-1} [22].

The rotation speed of the electrode ω (rad s^{-1}) is obtained from the experimental rotation rate rev (rpm) [23]:

$$\omega = \frac{2\pi * rev}{60} \quad (15)$$

When the concentration of the electroactive species on the surface is zero and the electrode is mass-transport controlled, the current does not increase and is constant, which is called limiting current. The limiting current density ($j_L / \text{A m}^{-2}$) is given by

$$j_L = n * F * D * \frac{c}{\delta} \quad (16)$$

with

n ...Number of electrons involved

F ...Faraday constant (96,500 / C mol⁻¹)

c ...Concentration of electroactive species / mol m⁻³

The Levich equation is the combination of (14) and (16):

$$j_L = 0.62 * n * F * D^{0.67} * \nu^{-0.166} * c * \omega^{0.5} \quad (17)$$

If the plot of j_L against $\omega^{0.5}$ is linear and passes through the origin, the reaction is mass-transport controlled [22].

2.4.2.1 Koutecky-Levich analysis

The Koutecky-Levich analysis can be used to determine the overall electron-transfer number of a reaction, the diffusion coefficient, or the standard rate constant. For the ORR, the analysis can be used to estimate if the reduction results from the four- or two-electron pathway (see 2.3). The RDE is utilized to record voltammograms of the ORR at different rotations rates of the electrode. Figure 10 shows the plot of the current density vs. potential of such measurements. The range of 0.85-0.93 V shows that the current densities of all rotation rates are similar and are only determined by the applied potential. Here the current densities are dictated by electron-transfer kinetics. In the potential range of < 0.80 V the current densities start to increase with increasing rotation rate and reach a constant value at potential < 0.63 V (limiting current density) [25]. In this zone the current densities are limited by mass transport [26].

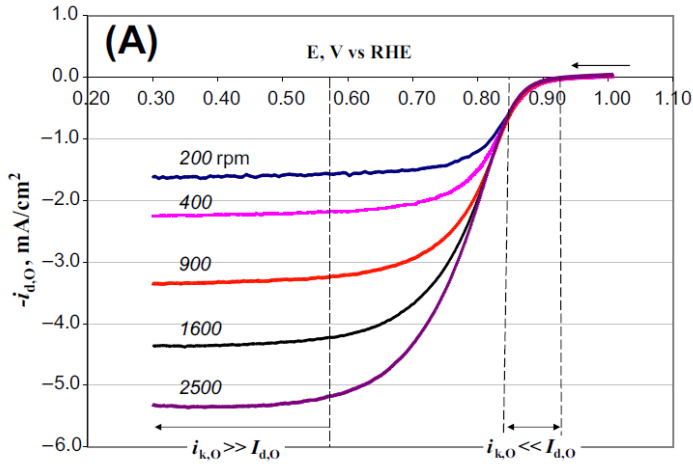


Figure 10: Voltammograms of ORR of a Pt disk electrode in O₂-saturated 0.5 M H₂SO₄ at 30°C with v of 5 mV s⁻¹ and different ω [25].

The plot of reciprocal limiting current density against the reciprocal square root of the rotation rate is the Koutecky-Levich plot. The plots of the voltammograms of Figure 10 at different electrode potentials are shown in Figure 11. When the extrapolation of the straight line to the y-axis intercepts with zero (means infinite rotation rate), the reaction is only mass transport limited and not kinetically limited (0.6 V in Figure 11). In the case of non-zero intercept (0.7-0.8 V in Figure 11) the reaction is also kinetically limited [25,26].

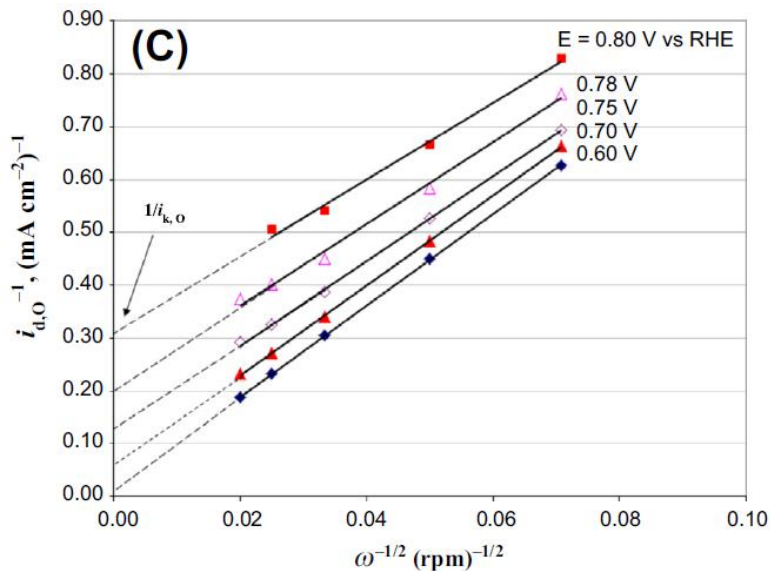


Figure 11: Koutecky-Levich plot of the voltammograms (Figure 9) at different electrode potentials [25].

The Koutecky-Levich equation is the reciprocal of the Levich equation (17) [26]:

$$\frac{1}{i} = \frac{1}{i_k} + \left(\frac{1}{0.62 * n * F * D^{0.67} * \nu^{-0.166} * c} \right) \omega^{-0.5} \quad (18)$$

with

i_k ...Kinetic current / A

ν ...Viscosity of the electrolyte / m² s⁻¹

D ...Diffusion coefficient / m² s⁻¹

ω ...Rotation speed of the electrode / rad s⁻¹

n ...Number of transferred electrons

F ...Faraday constant (96,500 / C mol⁻¹)

c ...Concentration of electroactive species / mol m⁻³

The electron-transfer number (n) can be determined from the slope, if all other parameters are known [25].

2.4.3 Rotating ring-disc electrode

The usage of a rotating ring-disc electrode (RRDE) allows the determination of intermediates or side-products during an electrochemical reaction. Throughout the ORR, the reduction of oxygen to OH⁻ or H₂O results from the 4-e⁻ or 2-e⁻ pathway (see 2.3). In the case of the 2-e⁻ reaction the intermediate peroxide is formed. The RRDE has two WEs: a disc (WE1) surrounded by a ring (WE2) [27,28]. The ORR measurement is carried out by linear sweep voltammetry (LSV). The potential (vs. RE) of the disc is changing over of certain potential range while the potential (vs. RE) of the ring is fixed at a potential where the oxidation of H₂O₂ (HO₂⁻ in alkaline media) occurs. When the ORR takes place and H₂O₂ (HO₂⁻ in alkaline media) is generated at the disc, the peroxide is detected at the ring by oxidation [28,29]:



2.4.3.1 Collection efficiency

The collection efficiency (N) of a RRDE is the ratio of the number of moles of a product collected at the ring to the number of moles of this product produced at the disc. The calculation is carried out by dividing the ring current by the disc current (equation (20)). The collection efficiency of the RRDE is typically determined by using a simple one-electron redox pair (e.g. ferrocyanide/ferricyanide). The measurements are performed with LSV using different rotation rates of the RRDE. On the disc ferricyanide is reduced to ferrocyanide $Fe(CN)_6^{3-} + e^- \rightarrow Fe(CN)_6^{4-}$ which is then collected by the ring and oxidized to ferricyanide $Fe(CN)_6^{4-} \rightarrow Fe(CN)_6^{3-} + e^-$. N is then calculated with

$$N = -\frac{I_R}{I_D} \quad (20)$$

with

I_R ...Limiting current ring / A

I_D ...Limiting current disc / A

at the same voltage [30,31].

2.4.3.2 Peroxide Formation

During the O_2 reduction process the reduction of oxygen can result from the four-electron and/or the two-electron pathway (see 2.3). In the case of the $2e^-$ pathway H_2O_2 (in acidic media) or HO_2^- (in alkaline media) is formed as intermediate. The amount of peroxide can be calculated from the measured limiting ring current for peroxide oxidation, (I_R), the limiting disc current (I_D) and the collection efficiency (N) of the RRDE with [16]

$$H_2O_2\% = 100 * \frac{2I_R/N}{I_D + \frac{I_R}{N}} \quad (21)$$

2.5 Physicochemical measurements

2.5.1 X-ray diffractometry

X-ray diffraction (XRD) can be used to determine crystal structures. Crystals have the property to diffract X-rays in a characteristic way. The position, intensity and shape of the peaks of the recorded diffraction patterns provide several information about the specimen. For example, peak position: space group, lattice parameters, chemical composition; peak intensity: crystal structure or texture; and shape: microstrains and crystallite size [32]. It can also be seen from the diffraction patterns (Figure 12) whether it is an amorphous or a crystalline solid [33].

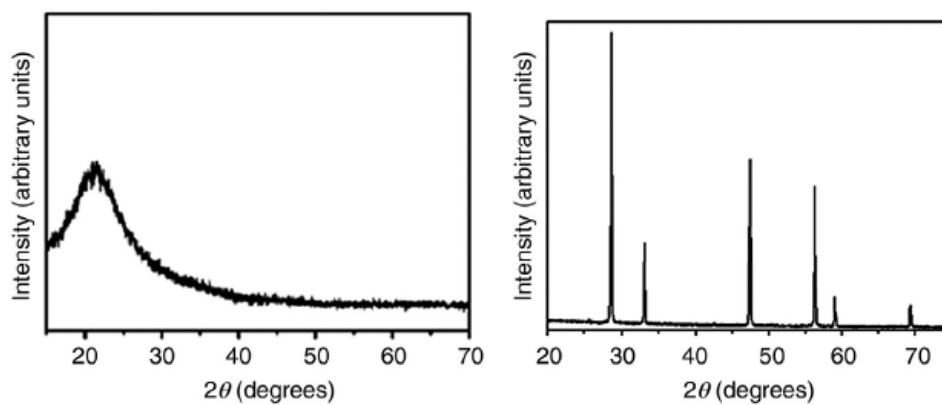


Figure 12: Schematic of XRD patterns of an amorphous (left) and a crystalline (right) solid [33].

The interaction of X-ray photons with electrons in a material results in different adsorption and scattering effects. In the case of electrons surrounding the atomic nuclei the interaction with photons results in an elastic and coherent scattering (Rayleigh scattering). The scattered wave has no energy losses and the same phase relationship to the incident wave. Thus, each atom scatters photons in all directions. In a crystalline structure the periodic arrangement of the atoms leads to constructive and destructive scattering effects and thus to characteristic diffraction pattern of the peaks [32,33].

Constructive interference occurs when two beams have a phase difference of $n\lambda$ (reinforce each other) and destructive by $n\lambda/2$ (cancel each other). The XRD method is based on the constructive interference of a X-ray beam on the planes of the crystal lattice of the specimen.

The diffraction of two beams on the crystallographic planes is shown in Figure 13. Bragg's law describes the geometrical conditions for constructive interference [34]:

$$n\lambda = 2d_{hkl} * \sin\theta \quad (22)$$

with

n ...Order of diffraction

λ ...Wavelength of the incident beam / nm

d_{hkl} ...Lattice spacing / nm

θ ...Angle of diffracted beam / °

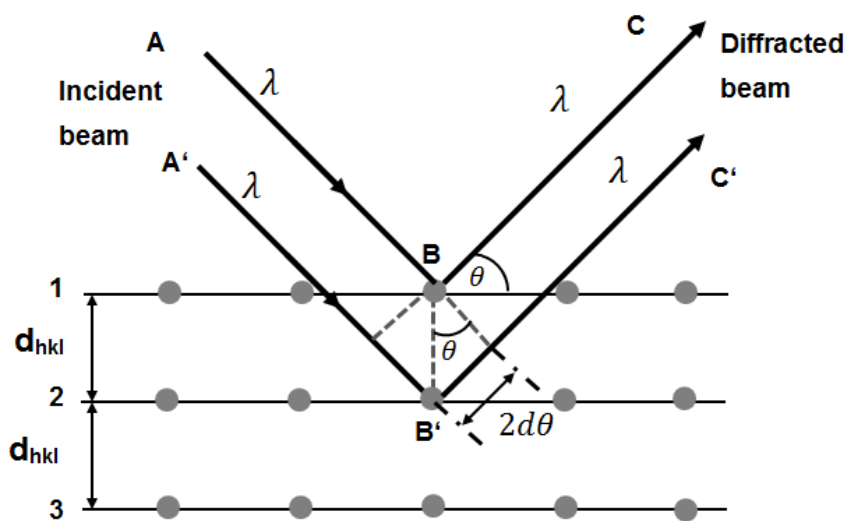


Figure 13: Schematic of the diffraction of X-ray beam on the crystallographic planes under Bragg's law condition [34].

The resulting diffraction data are then used to create a diffractogram, where the intensity is plotted against the 2θ angle (Figure 14). The background is subtracted and the maximum peak intensity (I_{max}), the integrated intensity (I_{int}), the full width at half maximum (FWHM), and the integral breadth (IB) can be determined [32].

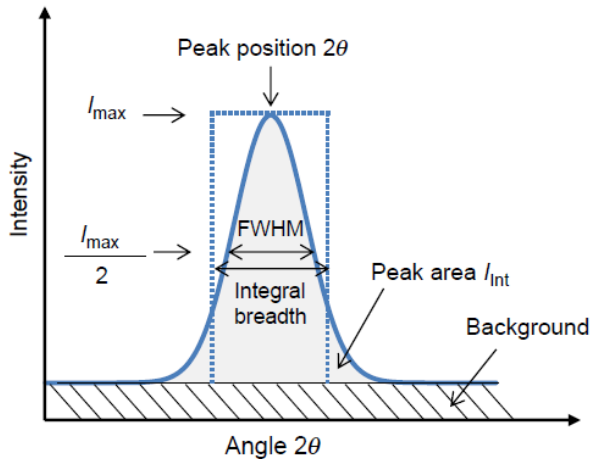


Figure 14: Schematic of a diffraction peak with a few parameters [32].

With the Scherrer equation (23) the average crystallite size (D) can be calculated [33]:

$$D = \frac{K\lambda}{FWHM(2\theta) \cos\theta} \quad (23)$$

with

λ ...Wavelength of the incident radiation / nm

K ...Constant close to 1

θ ...Bragg angle / rad

$FWHM$...Width at half height of the diffraction peak /nm

2.5.2 Specific surface area - Brunauer, Emmett, Teller method

The surface characteristics of heterogeneous catalysts are strongly influencing their performance, especially the catalytic activity, and therefore, the specific surface area is an important property [35,36]. The Brunauer, Emmett, Teller (BET) method is the mostly used one for the determination of the specific surface area (SSA) [37]. The adsorption method evaluates the amount of gas which is necessary to form a monolayer by physical adsorption on the surface of the solid. The amount of adsorbed gas on a surface is described by the adsorption isotherm. The adsorption isotherm represents the dependence of the amount of adsorbed gas to the partial

pressure at constant temperature. There are two different adsorption mechanisms: physisorption and chemisorption. In physisorption van der Waals forces bind the adsorbate on the surface while in chemisorption chemical valence forces occur. For the removal of the adsorbed species from the surface with physisorption less energy (1–2 kcal/mol) is necessary in comparison to chemisorption (10–100 kcal/mol). Physisorption is reversible and also nondissociative while the chemisorption mechanism is perhaps irreversible and often dissociative. Physisorption is able to accommodate multilayer of molecules while chemisorption is limited to monolayers [38].

According to the IUPAC classification there are five types of adsorption isotherms. The isotherm shapes are determined by the solid texture. In the isotherms type II and IV (Figure 15) there is first a monolayer formed followed by the formation of multilayers and therefore, they are the only one which are applicable for the BET equation (24) and thus for determination of the SSA [38,39].

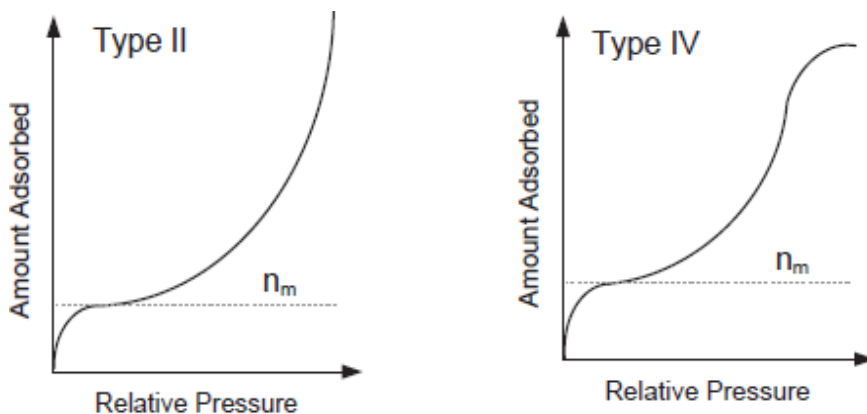


Figure 15: Schematic diagrams of the adsorption isotherms type II and IV [38].

From the course of the adsorption isotherm, the number of gas molecules which are necessary to form a complete monolayer on the solid surface can be calculated. The number of adsorbed molecules (equilibrium between adsorption and desorption) multiplied by the surface requirement of the molecule yields the surface area [40].

BET equation:

$$\frac{\frac{P}{P_0}}{V(1 - \frac{P}{P_0})} = \frac{1}{V_m * c_{BET}} + \frac{\frac{P}{P_0} * (c_{BET} - 1)}{V_m * c_{BET}} \quad (24)$$

with

V ...Volume of adsorbed molecules

V_m ...Volume of monolayer

c_{BET} ...BET constant

$\frac{P}{P_0}$...Relative pressure

From the plot $\frac{\frac{P}{P_0}}{V(1 - \frac{P}{P_0})}$ against $\frac{P}{P_0}$, V_m can be determined by

$$Slope = \frac{c_{BET} - 1}{V_m * c_{BET}} \quad (25)$$

$$Intercept = \frac{1}{V_m * c_{BET}} \quad (26)$$

$$V_m = \frac{1}{slope + intercept} \quad (27)$$

The SSA can then be calculated with:

$$SSA = \frac{V_m * N_A * a_m}{v_m * m_s} \quad (28)$$

with

N_A ...Avogadro's number ($6.022 * 10^{23} \text{ mol}^{-1}$)

a_m ...Molecule cross section area

v_m ...Molar volume of one adsorbed molecule (22.4 L by 1 mol of adsorbate gas at standard condition)

m_s ...Mass of substrate/adsorbent

2.5.3 Particle size distribution

Laser diffraction measurements are the common technique for the determination of the particle size distribution (PSD). The method is based on illuminating of the particles with a laser and the scattered light from the particles is then measured by series of detectors [41]. Depending on the size of the particle, the scattered light differs in intensity (small one weak, larger one strong) and scattering angle θ (small particles broad, larger particle small). Therefore, evaluation of the resulting angle scattering intensity pattern leads to the particle size and distribution [42]. The concept of a laser diffractometer is illustrated in Figure 16.

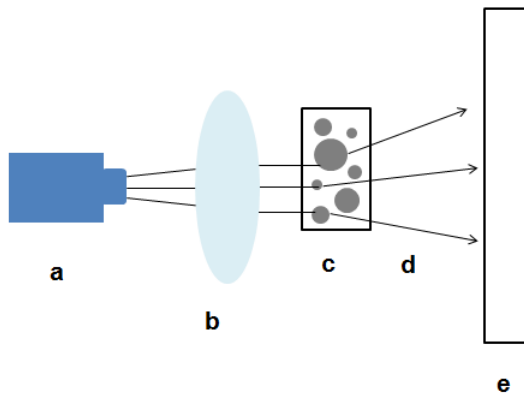


Figure 16: Schematic of the measuring unit of a laser diffractometer with a) laser, b) optical lens, c) sample cell, d) scattered beam, and e) detector array [42].

2.5.4 Scanning electron microscopy

A scanning electron microscope is a widely used tool to visualize micro- and nanostructures of the surface of a sample. In scanning electron microscopy (SEM) electrons are generated in a so called electron gun. The electron gun (cathode) has a filament (tungsten wire or LaB_6 crystal), which is heated to emit electrons. The electron cloud is then focused by a metallic cylinder (Wehnelt cylinder). The potential of the Wehnelt element is much more negative than those of the cathode and so the electrons are accelerated towards the anode. Below the anode, electromagnetic condenser lenses reduce the electron beam to a diameter of a few nanometers. Next, an objective lens focuses the electron beam and the sample is scanned in a line by-line pattern [43,44].

Finally, the beam of electrons reaches the specimen and scatters. Primary electrons, secondary electrons, and X-rays can be emitted depending on the used method. These signals are collected by appropriate detectors and build the basis for the formation of the structural image of the sample. The schematic assembly of a SEM is shown in Figure 17. Backscattered electrons (BSEs) are primary electrons (PEs) which are obtained due to elastic interaction of the electron beam with the atoms of the sample.

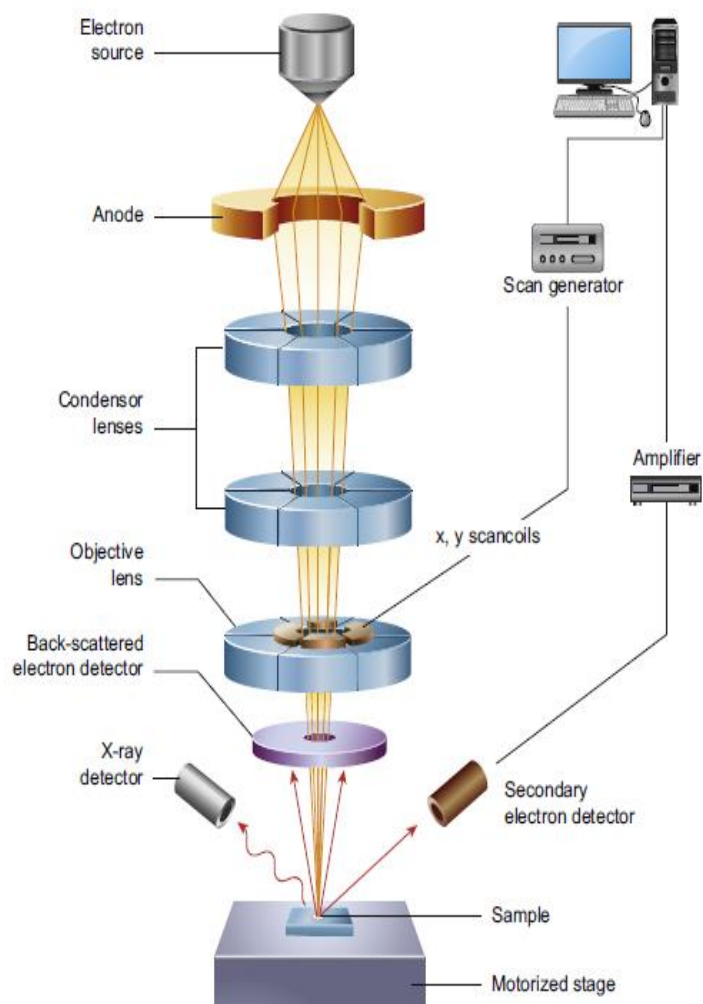


Figure 17: Schematic of the compounds of a scanning electron microscope [44].

BSEs have a high energy and are from deeper areas of the sample. When the PEs of the electron beam collide with weakly outer shell or valence electrons of an atom of the specimen and knock them out, these electrons are called secondary electrons (SEs). SEs have an energy of 3-50 eV and arise from areas near to the surface. Also Auger electrons can occur. They have specific energies and result from electron transitions between energy levels. X-rays are generated when primary electrons knock out an electron of an inner shell of an atom. The electron gap is then refilled by an electron of an outer shell. This electron has a higher energy and by occupying the vacancy the excess energy is released by emission of a photon. If the knocked out electron is in an outer electron shell, the energy difference between excited state and refilling is smaller. The emitted photon has the wavelength in the range of visible light and so cathodoluminescence phenomena happen.

The measurement is carried out under vacuum (low vacuum of 0.1 to 10^{-4} Pa) to avoid collision of the electron beam with air molecules [44,45]. In Figure 18 the different signals and the respective interaction volume of the sample are displayed.

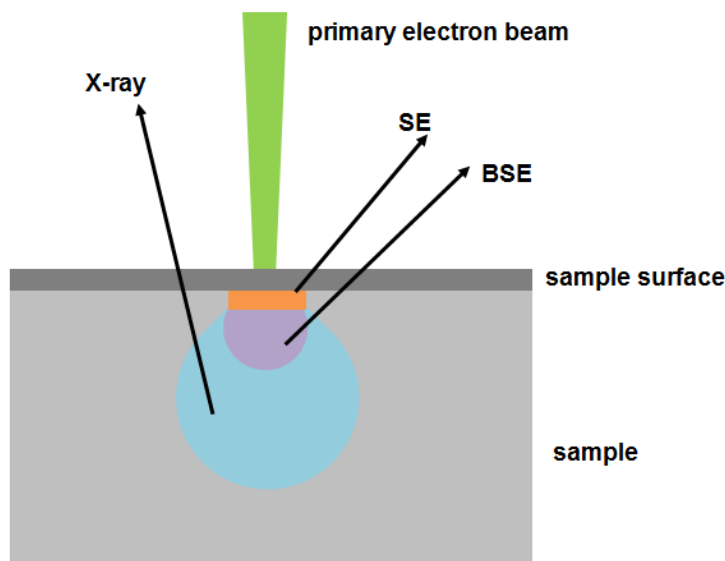


Figure 18: Schematic of origin and interaction volume of the different signals during SEM measurements [45].

2.6 Spinel

The general formula of the spinel is AB_2X_4 , where A and B are positive metal ions and X is a negative ion (mostly O^{2-} , but also S, Se or Te). There are various types of different combinations of cations with different oxidation states $A^{II}B^{III}_2X^{-II}_4$, $A^{IV}B^{II}_2X^{-II}_4$, $A^{VI}B^I_2X^{-II}_4$, $A^{II}B^I_2X^{-I}_4$. The anions build a cubic close-packing and therefore, the spinel has a face centred cubic (fcc) unit cell. One conventional cubic unit cell consists therefore of 32 anions and 24 cations (8 A ions and 16 B ions). There are two kinds of spinels with different configurations of cations: the normal spinel and inverse spinel. In the case of the normal spinel (e.g. $MgAl_2O_4$), the A cations reside every eight tetrahedral interstices and the B cations occupy octahedral holes. In contrast, in an inverse spinel ($TiMg_2O_4$ for instance), the B ions and one half of the A ions occupy the octahedral interstice. The remaining B ions fill every eight tetrahedral interstice. The formation of a normal or an inverse spinel is depending on, inter alia, the ligand field stabilization energy, the lattice energy and the size of the ions [46,47]. $NiCo_2O_4$ is an inverse spinel in which the divalent nickel ions occupy the octahedral sites and the trivalent cobalt ions are distributed over both octahedral and tetrahedral sites [48]. The cubic unit cell of $NiCo_2O_4$ is shown in Figure 19. In Figure 20 the unit cell with the tetrahedral and octahedral sites is displayed.

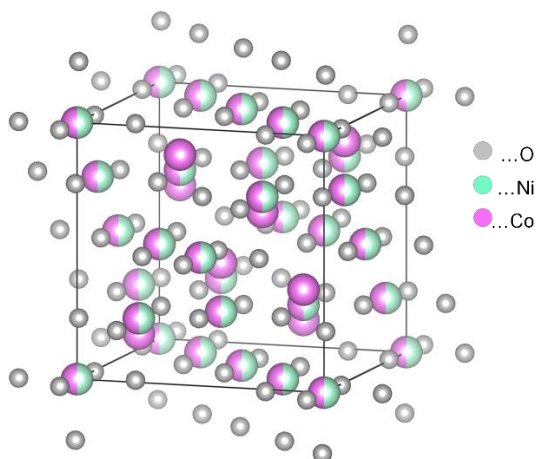


Figure 19: Schematic of ions (pink: Co, green: Ni and grey: O) of a $NiCo_2O_4$ spinel arranged in a cubic unit cell [49].

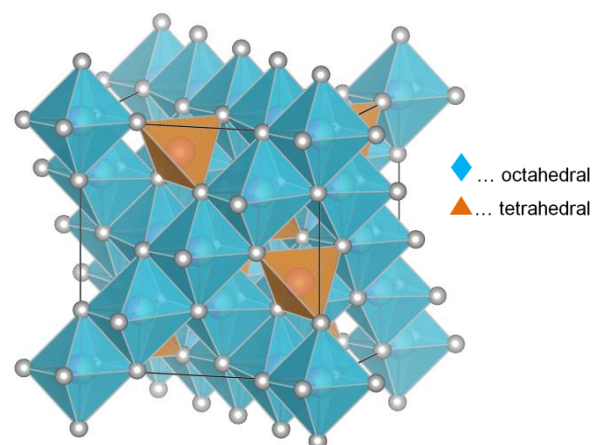


Figure 20: Schematic of tetrahedral (orange) and octahedral (blue) sites and ions (pink: Co, green: Ni and grey: O) of a $NiCo_2O_4$ spinel in a cubic unit cell [49].

3 Experimental

3.1 Catalyst preparation

The catalysts were prepared with two different thermal decomposition methods: the nitrate method and the hydroxide method. The starting materials for both were nickel and cobalt nitrate hexahydrate salts in the stoichiometric ratio of 1:2. For the nitrate method, the salts were dissolved in methanol, then the solvent was evaporated and the resulting solid was finally crushed and sieved before calcination. For the hydroxide method, the salts were dissolved in deionised water and precipitated with sodium hydroxide. Afterwards, the precipitate was filtrated, washed, dried and also crushed and sieved before calcination. For both methods different calcination temperatures and times were applied.

3.1.1 Nitrate method

At first 14.51 g (0.05 mol) of $\text{Ni}(\text{NO}_3)_2 \cdot 6 \text{H}_2\text{O}$ and 29.09 g (0.10 mol) of $\text{Co}(\text{NO}_3)_2 \cdot 6 \text{H}_2\text{O}$ were dissolved in 100 ml MeOH under stirring until a dark red brown solution was obtained. Subsequently, the solution was filled in a crystallizing dish and dried in an oven at about 80°C overnight.



Figure 21: The spinel P8 after calcination.

The obtained bright pink precipitate was crushed in a mortar and afterwards sieved (mesh width 63 μm) via grinding balls ($\varnothing = 5 \text{ mm}$, overall: 43.2781 g, yttrium stabilized ZrO_2). The resulting powder was then divided into two parts: the first part (P7) was calcined at 350°C for 20 hours (heating rate: 2.2°C/min) and the second part (P8) was calcined at 300°C for 20 hours (heating rate: 1.9°C/min). In both cases the spinel has a kind of crust with metallic shine (Figure 21) after calcination. Both calcined catalysts were then finely ground in an agate mortar. The samples P3 and P4 (prepared by E. Domian) were also prepared according to the nitrate method with the difference that these spinels were not sieved before calcination. Sample P3 was calcined at 300°C and P4 at 350°C for 2 hours, respectively.

3.1.2 Hydroxide method

At the beginning 3.63 g (12.48 mmol) of $\text{Ni}(\text{NO}_3)_2 \cdot 6 \text{H}_2\text{O}$ and 7.26 g (24.94 mmol) of $\text{Co}(\text{NO}_3)_2 \cdot 6 \text{H}_2\text{O}$ were dissolved in 25 ml deionised water (deion. H_2O) under stirring until the solution was clear and dark red violet. Then 10.00 g of NaOH were dissolved in 375 ml of deion. H_2O under stirring. Subsequently, the metal salt solution was added dropwise to the NaOH solution under stirring and at the end the solution was blue/yellow with blue/violet precipitate (Figure 22). After precipitation the solution was stirred for 1.5 h at room temperature (RT).

Afterwards, the solution was clear with a blue/yellow precipitate. Then, the clear supernatant was decanted and the olive green precipitate was filtrated with a cellulose filter (45 μm pore size) under vacuum (Figure 23). The precipitate was washed with deion. H_2O and transferred to a crystallizing dish and dried in an oven at about 100°C overnight (~ 17.5 h). The dried precipitate has a dark brown colour and was crushed in an agate mortar and sieved (mesh width 63 μm) by grinding balls. The resulting powder (sample P9) was calcined at 375°C for 2 hours (heating rate: 2.4°C/min).



Figure 22: Solution after metal salt addition.



Figure 23: Arrangement of the filtration equipment.

The sample P2_BK (prepared by Elisabeth Domian) was also prepared with the hydroxide method in the same way and calcined at 375°C for 20 hours.

In the further description the samples are named P2_BK (375°C/OH/s), P3 (300°C/NO₃/u), P4 (350°C/NO₃/u), P7 (350°C/NO₃/s), P8 (300°C/NO₃/s), and P9 (375°C/OH/s) with **NO₃**...nitrate preparation method, **OH**...hydroxide preparation method, **s**...sieved before calcination, **u**... unsieved before calcination.

Details of the sample preparation are summarised in Table 1.

Table 1: Preparation details of the catalysts.

Sample	Method	Sieved ¹⁾	Calci. temp / °C	Calci. time / h	Prepared by Domian	Prepared by Krenn
P2_BK	OH	yes	375	20	x	
P3	NO ₃	no	300	2	x ²⁾	
P4	NO ₃	no	350	2	x ²⁾	
P7	NO ₃	yes	350	20		x ²⁾
P8	NO ₃	yes	300	20		x ²⁾
P9	OH	yes	375	2		x

¹⁾ before calcination

²⁾ same sample

3.2 Preparation of the neutral electrolytes

Due to the problems with KOH electrolyte in zinc-air redox flow batteries (see 2.2.3) neutral choline electrolytes were also investigated. Good results of zinc deposition were determined in

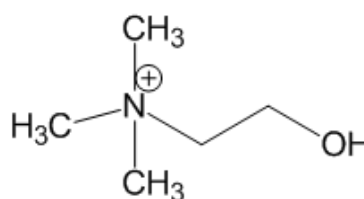


Figure 24: Structure of the choline cation.

choline acetate and therefore, also the electrochemical properties of the NiCo₂O₄ spinel in choline electrolytes were investigated.

For the experiments of OER and ORR in choline acetate a higher potential range (in comparison to KOH) was necessary to study the electrochemical behaviour. Experiments with two other anions (sulphate and carbonate) were also done. In Figure 24 the structure of the choline cation is shown.

3.2.1 Choline acetate

For the preparation of the choline acetate (C-OAc) electrolyte 30 wt% of choline acetate (98%) were diluted with deion. H₂O under stirring. The resulting electrolyte was clear and has a pH value of 7.1.

3.2.2 Choline sulphate

The choline sulphate (C-SO₄) electrolyte was produced by neutralisation of choline hydroxide (C-OH, 46% w/w aq. soln.) with sulfuric acid (> 95%). At first, 10 ml H₂SO₄ and 20 ml deion. H₂O were mixed. Then, 40 ml choline hydroxide were added in an argon gas counterflow with an Ar flushed syringe. Then, 5.5 ml of the 1:2 H₂SO₄ dilution were added under stirring. Finally, the electrolyte was a dark yellow solution with a pH value of 6.6. After one to two days the electrolyte was dark orange and has a pH value of 7.8.

3.2.3 Choline carbonate

Preparation of the choline carbonate (C-CO₃) electrolyte was done by heating 75 ml of a choline bicarbonate solution (~80% in H₂O, pH=10.5) at 60°C for 60 min under stirring. The resulting C-CO₃ was diluted 1:1 with deion. H₂O because it was too viscous. The C-CO₃ electrolyte was clear and has a pH of 9.9.

3.3 Electrochemical characterisation

For the investigation of the electrochemical properties of the catalysts cyclic voltammetry (CV) and linear sweep voltammetry with rotating disc electrode and rotating ring-disc electrode were carried out. The CV measurements were utilised to determine the transition of the oxidation states of the nickel and cobalt in the spinel. For the investigation of the catalytic properties of the spinels concerning the kinetics and mechanisms of the OER and ORR linear sweep voltammetry was carried out.

3.3.1 Catalyst slurry preparation and application to the electrode

For the catalyst slurry, 2 mg of the respective spinel was dispersed in 6 ml of deion. H₂O. The suspension was then homogenised in an ultrasonic bath for 30 minutes. In the meantime the glassy carbon disc ($\varnothing = 5\text{mm}$) of the RDE or RRDE was polished with aluminium oxide (Al₂O₃) powder (particle size 0.3 μm) on a moistened polishing cloth.

15 μl of the homogenised catalyst suspension were applied three times on the surface of the electrode and each time dried with an infrared (IR) lamp (100 W). For the protection of the catalyst layer against damaging, Nafion was used. Therefore, 15 μl of a Nafion solution (1 w% in deion. H₂O) were applied on the electrode and also dried with the IR lamp.

3.3.2 Cyclic voltammetry and rotating disc electrode experiment

The studies of the electrochemical performance of the catalyst were carried out in a three electrode arrangement. A GC-RDE from Pine Instruments was used as working electrode (WE) and as counter electrode (CE) a Pt-grid was applied. The reference electrode (RE) was a Hg/HgO electrode for the alkaline electrolyte and an Ag/AgCl electrode for neutral electrolytes. The RE's were placed in a Haber-Luggin capillary that was filled with 8 M KOH or 3 M KCl. The electrolytes were 8 M KOH, C-OAc, C-SO₄ and C-CO₃.

All experiments were carried at room temperature (RT). Before the CV measurements and the studies of OER, the electrolyte was flushed with nitrogen for 30 minutes. During the experiments the electrolytes were purged with N₂. In a series of three successive measurements, the electrolyte was flushed with N₂ for 5-10 minutes after each OER measurement. The CV's were recorded with different scan rates. The OER measurements were always carried out at constant scan rate (5 mV s⁻¹) and rotation rate (400 rpm). The studies of the ORR were performed in oxygen saturated electrolytes and therefore, the electrolyte was flushed with O₂ before measurements for 30 minutes. During the measurements, O₂ was blown over the solution and after each recorded voltammogram the electrolyte was flushed again with oxygen for 30 minutes. The ORR measurements were performed at constant scan rate (5 mV s⁻¹) and different rotation rates.

An Autolab PGSTAT (AUT83568 and AUT86739) and the software NOVA 1.11 for data analysis were used for electrochemical experiments.

3.3.3 Rotating ring-disc electrode experiment

3.3.3.1 Collection efficiency

The determination of the collection efficiency of the RRDE was performed using a four electrode arrangement. The CE was a Pt-grid, the RE was an Ag/AgCl (3 M KCl) electrode and the WE1 and WE2 was an uncoated GC/Pt RRDE with a glassy carbon disc ($\varnothing = 5\text{mm}$, WE1) and a Pt ring (WE2) from Pine Instruments (Figure 25). The measuring unit is shown in Figure 26. The electrolyte was a 0.1 M KCl solution with 5 mM K₃Fe(CN)₆.



Figure 25: Rotating ring-disc electrode with Pt ring and glassy carbon disc.

The experiment was carried out at RT and before measurements the electrolyte was flushed with nitrogen for 30 minutes. At first, a CV was recorded to monitor the redox reaction of the Fe(CN)₆³⁻ / Fe(CN)₆⁴⁻ redox couple. Afterwards, the LSV was performed with different rotation rates of the RRDE at the potential range of the disc

from 0.4 to -0.7 V vs. Ag/AgCl. The potential of the ring was fixed at 0.5 V vs. Ag/AgCl, where the oxidation of $\text{Fe}(\text{CN})_6^{4-}$ to $\text{Fe}(\text{CN})_6^{3-}$ occurs.

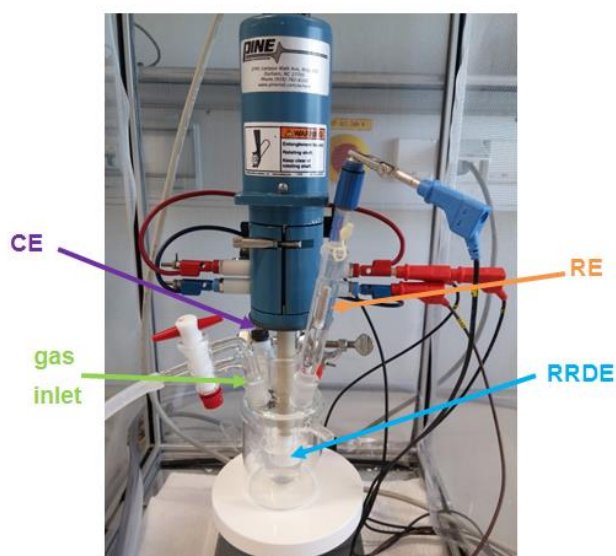


Figure 26: Measuring unit of RRDE experiments with the RE, CE, RRDE, gas inlet and measuring cell.

3.3.3.2 Detection of peroxide formation

Experiments with the RRDE were performed to determine the peroxide formation during ORR. The catalyst P7 was investigated in 8 M KOH and in C-OAc. The spinel was applied to the RRDE as described in 3.3.1. The RE was a Hg/HgO (8 M KOH) electrode for the alkaline electrolyte and a Ag/AgCl (3 M KCl) electrode for neutral electrolytes in a Haber-Luggin capillary, respectively. The applied CE was a Pt-grid in both cases. The WE was the RRDE with the GC disc as WE1 and the Pt ring as WE2. The investigations were carried out with different rotation rates at RT and O_2 saturated electrolytes. During measurements in 8 M KOH, the ring potential was fixed at 0.2 V vs. Hg/HgO [50] and in choline acetate at 0.7 V vs. Ag/AgCl.

3.4 Physicochemical characterisations

For the investigation of the physicochemical properties of the spinels, different measurements were performed. The crystal structure was investigated via XRD measurements. The specific surface area was determined by the BET method and the particle size distribution was also specified. SEM images were recorded to illustrate the morphology, the homogeneity and the particle size of the different catalysts.

3.4.1 X-ray diffractometry

The structural characterisation of the synthesized NiCo_2O_4 catalysts was performed with X-ray powder diffractometry at the Institute for Physical Chemistry. The measurements were done by using Bruker D8 Advance and Philips PW1700 powder diffractometer equipment. $\text{Cu-K}\alpha$ was used as radiation source in the 2θ range of 15° to 80° . For data analysis the software program X'Pert HighScore plus (PANalytical) was used.

3.4.2 BET measurements - specific surface area

The measurements were carried out at the Institute for Process and Particle Engineering. The determination of the specific surface area (SSA) of the NiCo_2O_4 spinels was carried out through nitrogen adsorption using TriStar II 3020 (Micromeritics, Norcross, Georgia). The samples were outgassed under vacuum at RT for 24 hours and the volume of adsorbed N_2 was recorded between a relative pressure range of 0.01 and 0.99. The SSA was then calculated according to the Brunauer-Emmett-Teller (BET) theory using 8 points in the relative pressure range of 0.05 - 0.2.

3.4.3 Particle size distribution measurements

The measurements of particle size distribution (PSD) were also carried out at the Institute for Process and Particle Engineering. The PSD tests of the NiCo_2O_4 catalysts were conducted on a HELOS(H2395)/KR Laser diffraction sensor. The measurements were performed in a CUVETTE wet dispersion system of Sympatec GmbH with a cuvette size of 50 ml, stirring speed of 1000 rpm, optical concentration of 1% - 20%, and a measuring range of combined R2+R5 (0.25/ 0.45 – 875 μm). The evaluation was done according to Fraunhofer approximation. The software was WINDOX 5.

3.4.4 Scanning electron microscopy

The morphology, homogeneity, and particle size of the different NiCo_2O_4 spinels were determined by recording images with a scanning electron microscope (SEM). The investigations were performed by ESEM Tescan 500 PA. For the sample preparation a double-sided carbon tape was glued onto a specimen holder and the catalyst powder was applied to the tape with a spatula.

4 Results and discussion

4.1 Electrochemical measurements - rotating disc electrode

4.1.1 Cyclic voltammetry in 8 M KOH

The cyclic voltammograms (CVs) of the catalysts P2_BK, P3, P4, P7, P8 and P9 are compared in Figure 27. The measurements were performed in 8 M KOH with the scan rate of 10 mV s^{-1} , respectively. The weaker pronounced peaks at about 0.25 V vs. Hg/HgO are assigned to the reversible oxidation of Co(II)/Co(III) and the peaks at $\sim 0.43 \text{ V}$ vs. Hg/HgO to the transition of Ni(II)/Ni(III) and Co(III)/Co(IV) [51]. The sample P9 displays the highest current density. The CVs of the samples of the nitrate method with the same calcination temperature (sieved/unsieved) show very similar peak sizes and those with the lower temperature are much larger. The CV of the sample P2_BK shows an anodic peak that is higher than for the samples P4 and P7. The cathodic peak is more or less in the same height as for sample P4 and P7.

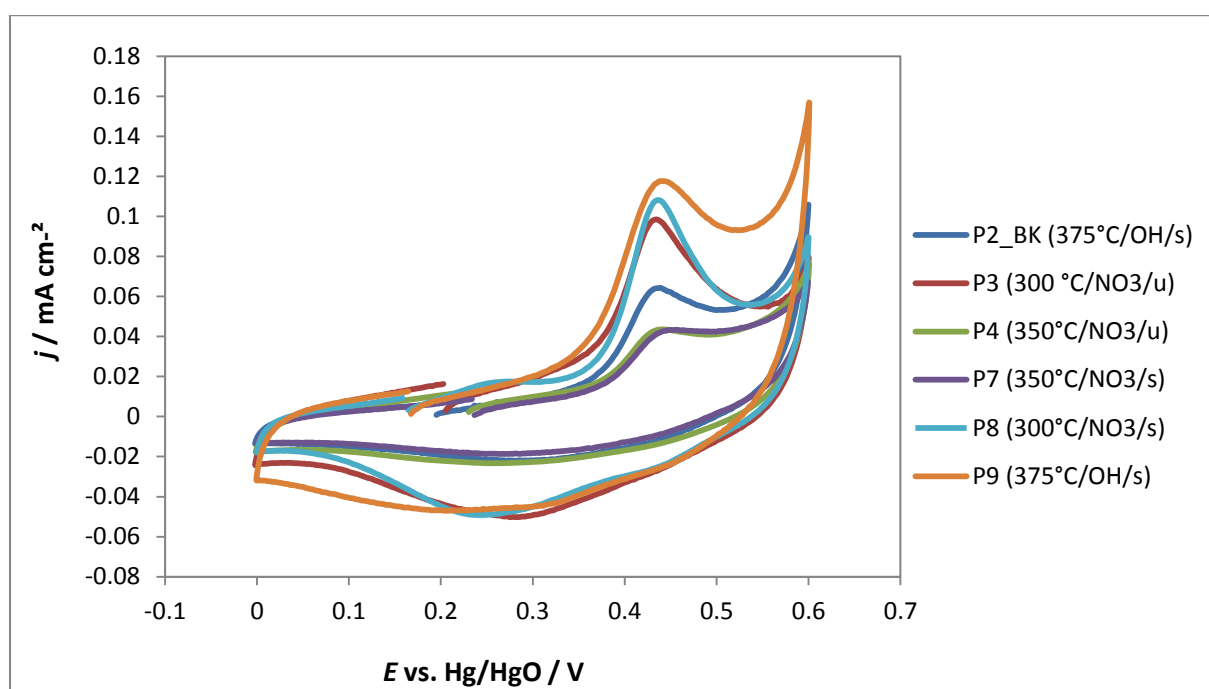


Figure 27: Comparison of the cyclic voltammograms of the different NiCo_2O_4 spinels in 8 M KOH at RT with ν of 10 mV s^{-1} .

The CVs of the samples P7 to P9 with different scan rates are shown in Figure 28 to Figure 30. The current density of all three samples increases with increasing scan rate while the shape of the curves remain unchanged. The sample of the nitrate method (P7, 350°C) shows much lower current densities than the other two catalysts.

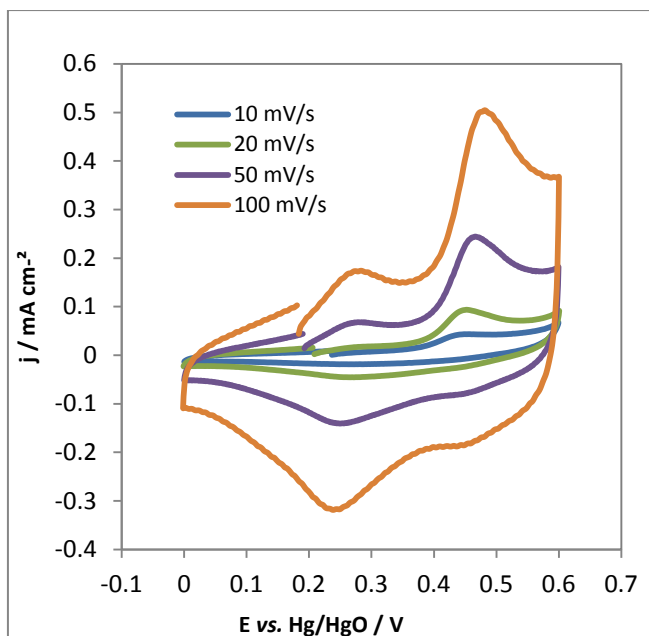


Figure 28: Cyclic voltammograms of P7 (350°C/NO₃/s) in 8 M KOH at RT with different scan rates.

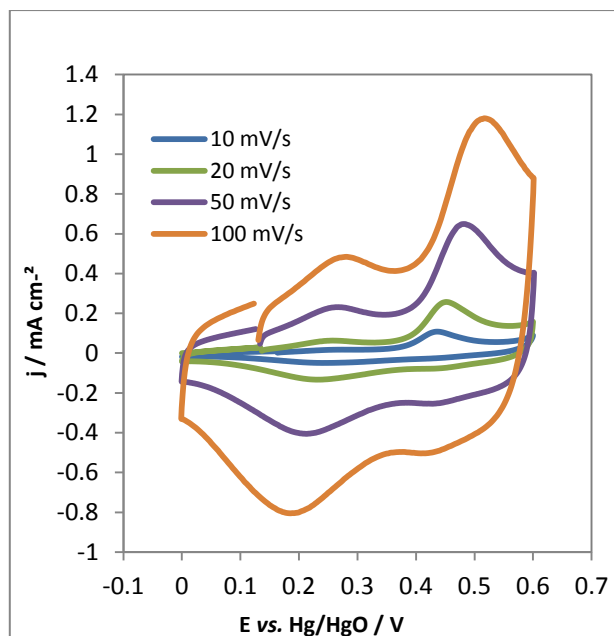


Figure 29: Cyclic voltammograms of P8 (300°C/NO₃/s) in 8 M KOH at RT with different scan rates.

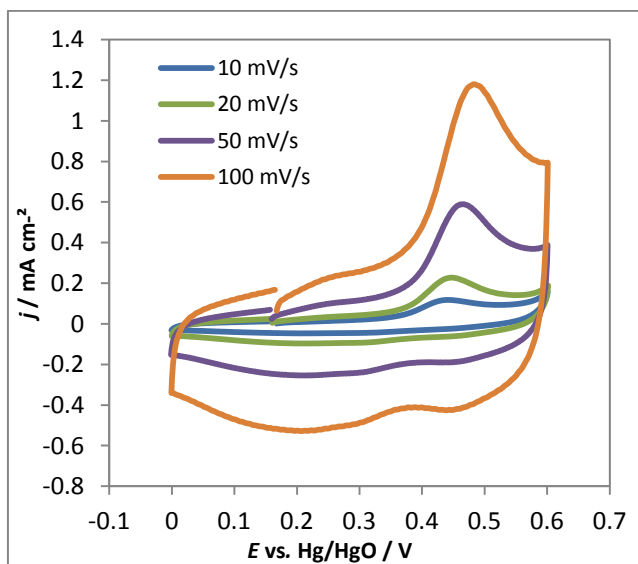


Figure 30: Cyclic voltammograms of P9 (375°C/OH/s) in 8 M KOH at RT with different scan rates.

Figure 31 displays the plot of the anodic peak current density vs. scan rate of the samples P7 to P9. For all three samples a linear dependence can be observed. The values of the catalyst of the nitrate method (P7, 350°C) are lower than those of the other two catalysts.

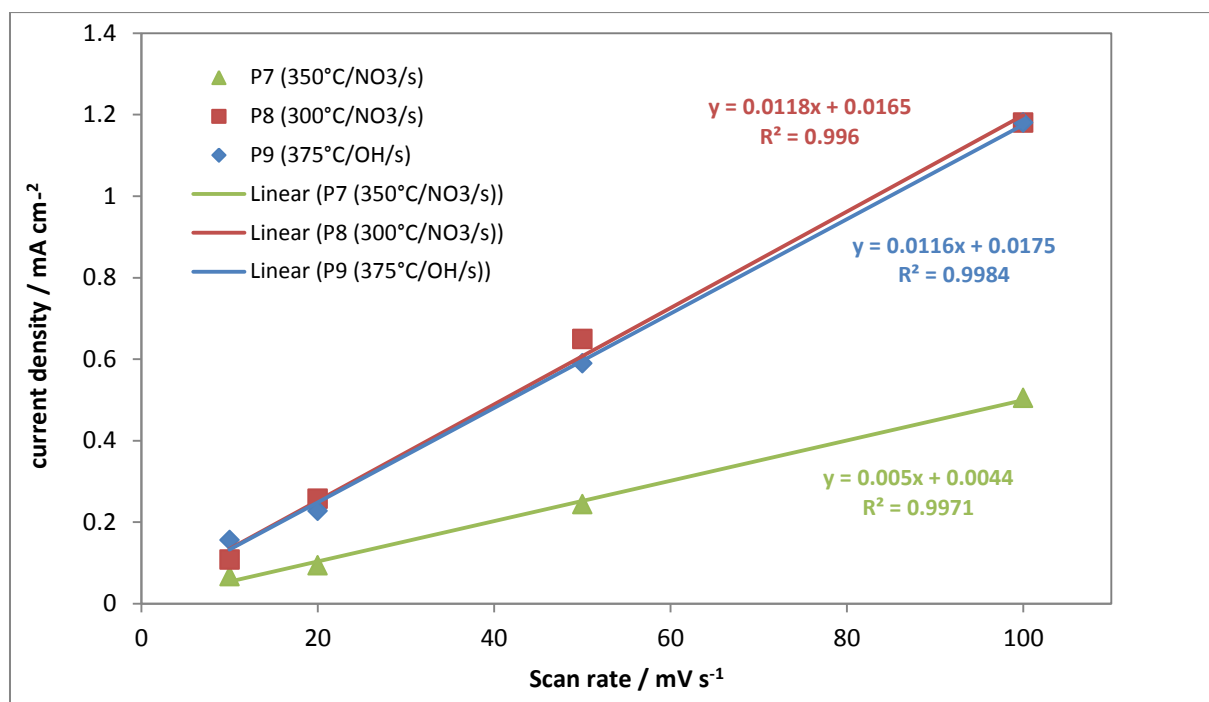


Figure 31: Plot of peak current density vs. scan rate of P7 (350°C/NO₃/s), P8 (300°C/NO₃/s) and P9 (375°C/OH/s) in 8 M KOH at RT.

A series of ten successive cycles of each catalyst was performed to investigate the stability. The CVs were recorded after the CVs with different scan rates. A comparison of the first and the tenth cycle of spinel samples are shown in Figure 32 - Figure 37. The sample P3 (Figure 33) shows the largest change in peak size. The reductive as well as the oxidative peak in the tenth cycle is larger. The shape of the oxidative peak of the samples P2_BK (Figure 32), P8 (Figure 36) and P9 (Figure 37) is more or less stable. P4 (Figure 34) and P7 (Figure 35) show a bit higher oxidative peaks. The reductive peak of all catalysts is slightly higher in the tenth cycle than in the first cycle.

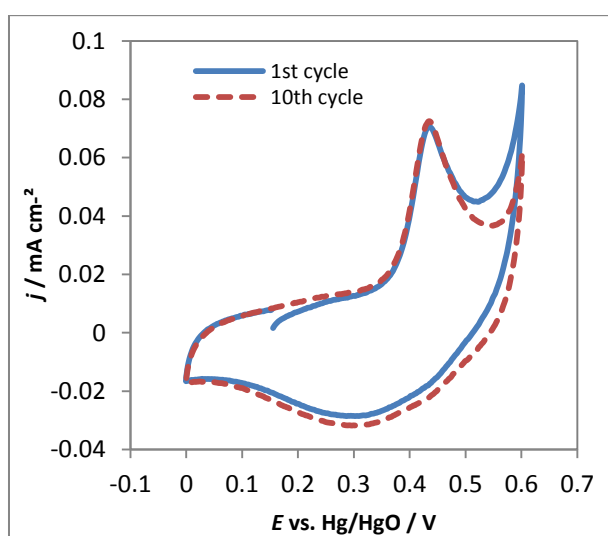


Figure 32: Cyclic voltammograms of the 1st and 10th cycle of P2_BK (375/OH/s) in 8 M KOH at RT with v of 10 mV s^{-1} .

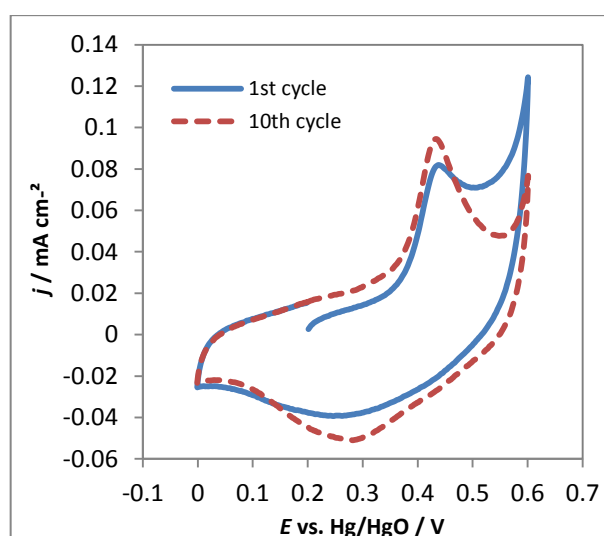


Figure 33: Cyclic voltammograms of the 1st and 10th cycle of P3 (300°C/NO₃/u) in 8 M KOH at RT with v of 10 mV s^{-1} .

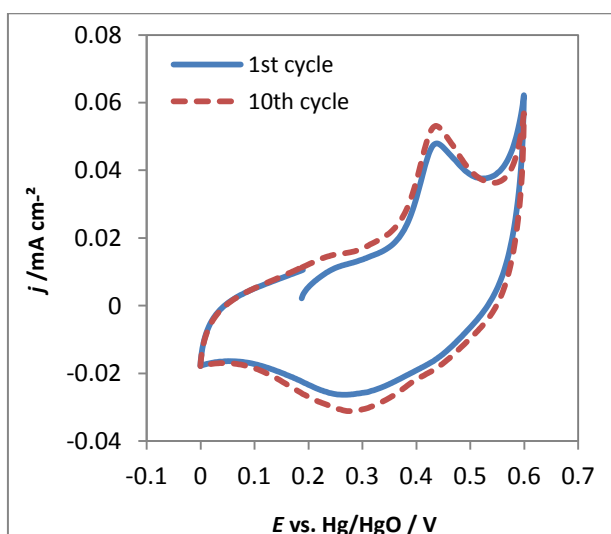


Figure 34: Cyclic voltammograms of the 1st and 10th cycle of P4 (350°C/NO₃/u) in 8 M KOH at RT with v of 10 mV s^{-1} .

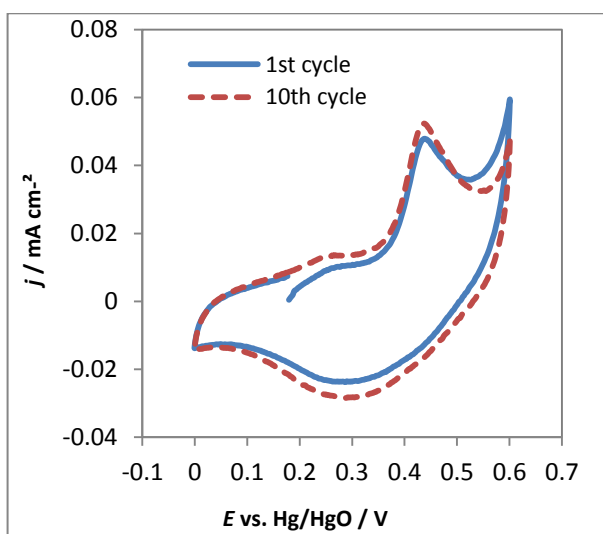


Figure 35: Cyclic voltammograms of the 1st and 10th cycle of P7 (350°C/NO₃/s) in 8 M KOH at RT with v of 10 mV s^{-1} .

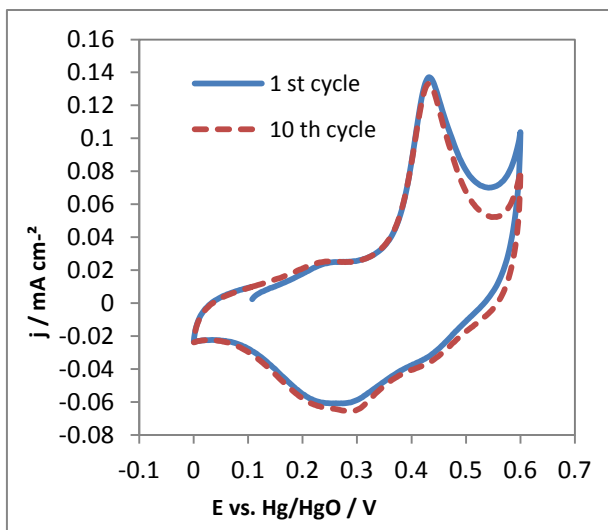


Figure 36: Cyclic voltammograms of the 1st and 10th cycle of P8 (300°C/NO₃/s) in 8 M KOH at RT with ν of 10 mV s⁻¹.

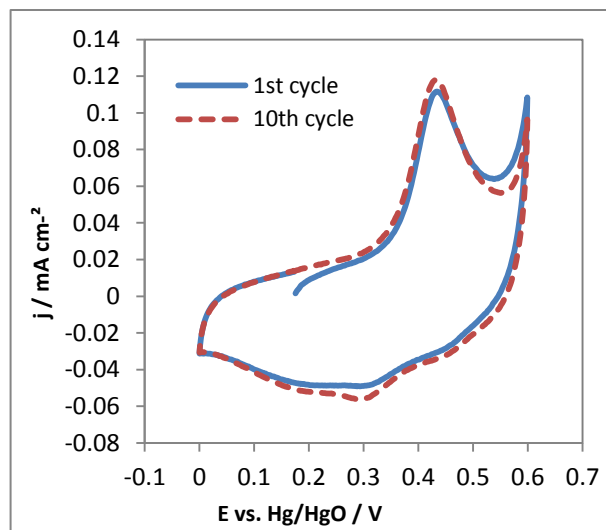


Figure 37: Cyclic voltammograms of the 1st and 10th cycle of P9 (375°C/OH/s) in 8 M KOH at RT with ν of 10 mV s⁻¹.

4.1.2 Cyclic voltammetry in C-OAc, C-SO₄ and C-CO₃

The catalyst P7 was arbitrary chosen to investigate its electrochemical properties in the choline electrolytes. A comparison of the CVs of the catalyst P7 in the three different choline electrolytes is shown in Figure 38. The Figure 39 displays another scale of this comparison. These CVs show the first cycle of a measuring series of five cycles. A reductive peak at about -0.3 to -0.4 V vs. Ag/AgCl occurs only in the first cycle. The comparison of the CVs in the three different electrolytes shows that the onset potential of the O₂ evolution is lowest in C-CO₃ and in C-SO₄ it is highest. The potential in C-OAc is between. In contrast to the CVs recorded in 8 M KOH a larger potential range for the CVs was necessary for the observation of peaks. The potential range of the CVs in 8 M KOH was 0.6 V and in the choline electrolytes it was 2 V.

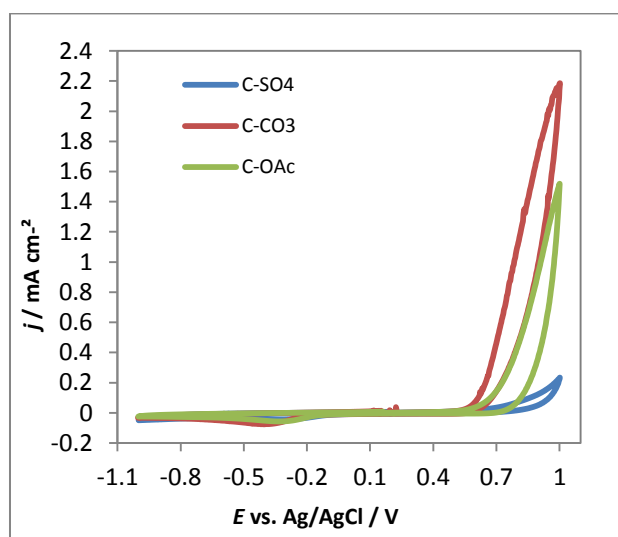


Figure 38: Comparison of the cyclic voltammograms of P7 (350°C/NO₃/s) in choline acetate, - sulphate and - carbonate at RT with ν of 10 mV s⁻¹.

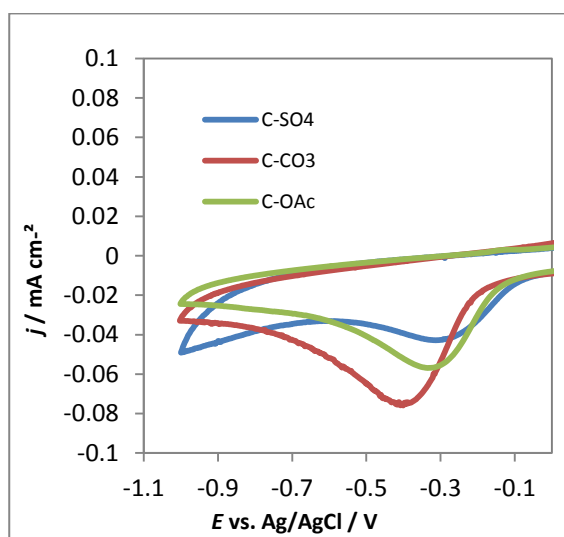


Figure 39: Comparison of the cyclic voltammograms of P7 (350°C/NO₃/s) in choline acetate, - sulphate and - carbonate at RT with ν of 10 mV s⁻¹ in another scale.

4.1.3 ORR and OER in 8 M KOH

Voltammograms of the ORR of the different catalyst samples in 8 M KOH were recorded at different rotation rate (Figure 40 -Figure 43). The trend of increasing limiting current densities with increasing rotation rates of the different catalysts could only be observed for sample P2_BK, P3, P8 and P9 (not shown for other samples). The current densities of the catalysts P2_BK (Figure 40) and P3 (Figure 41) show an equal distance between different rotation rates. For the sample P8 (Figure 42) the curves are more closer to each other, especially between 2000 and 2300 rpm. The current densities of the catalyst P9 (Figure 43) also increase with increasing rotation rate and the distance between 1300 and 1600 rpm is smaller.

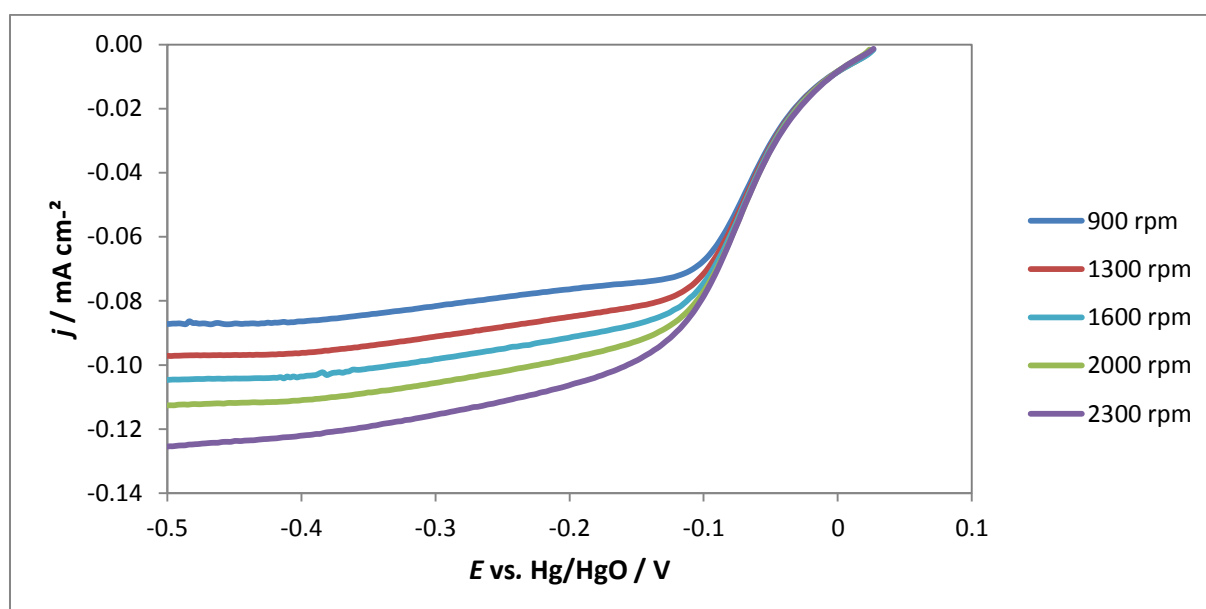


Figure 40: Voltammograms for ORR of P2_BK (375°C/OH/s) in 8 M KOH at RT with v of 5 mV s^{-1} and different ω .

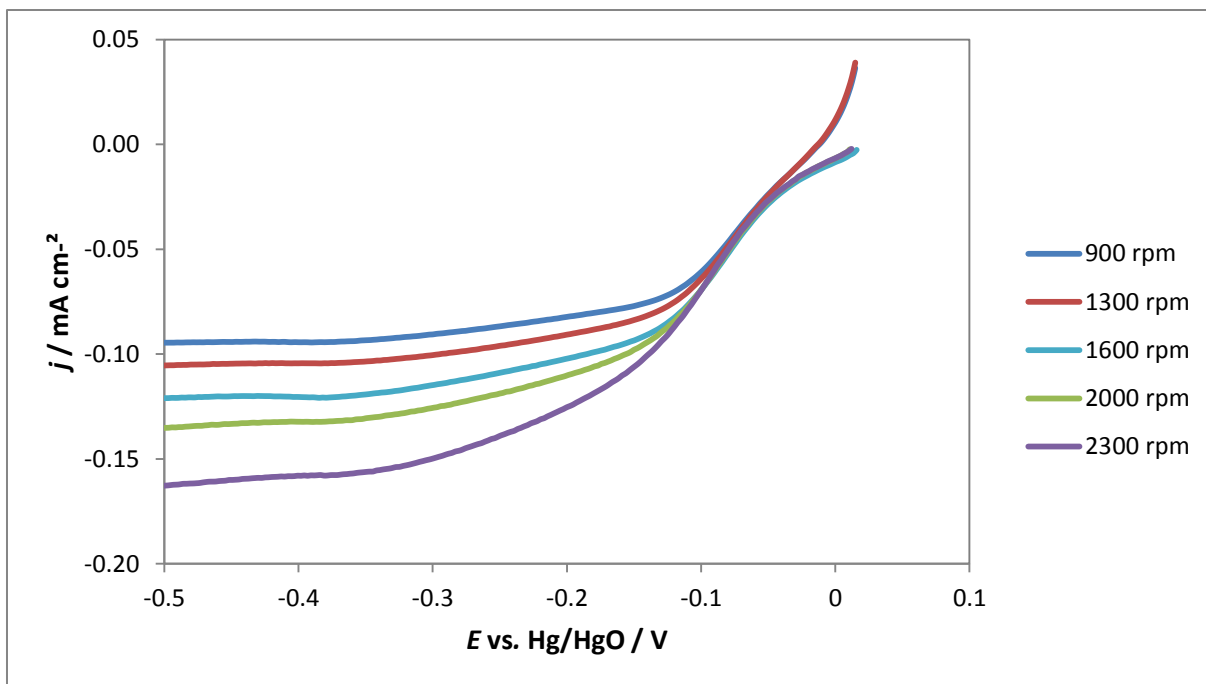


Figure 41: Voltammograms for ORR of P3 (300°C/NO₃/u) in 8 M KOH at RT with v of 5 mV s⁻¹ and different ω .

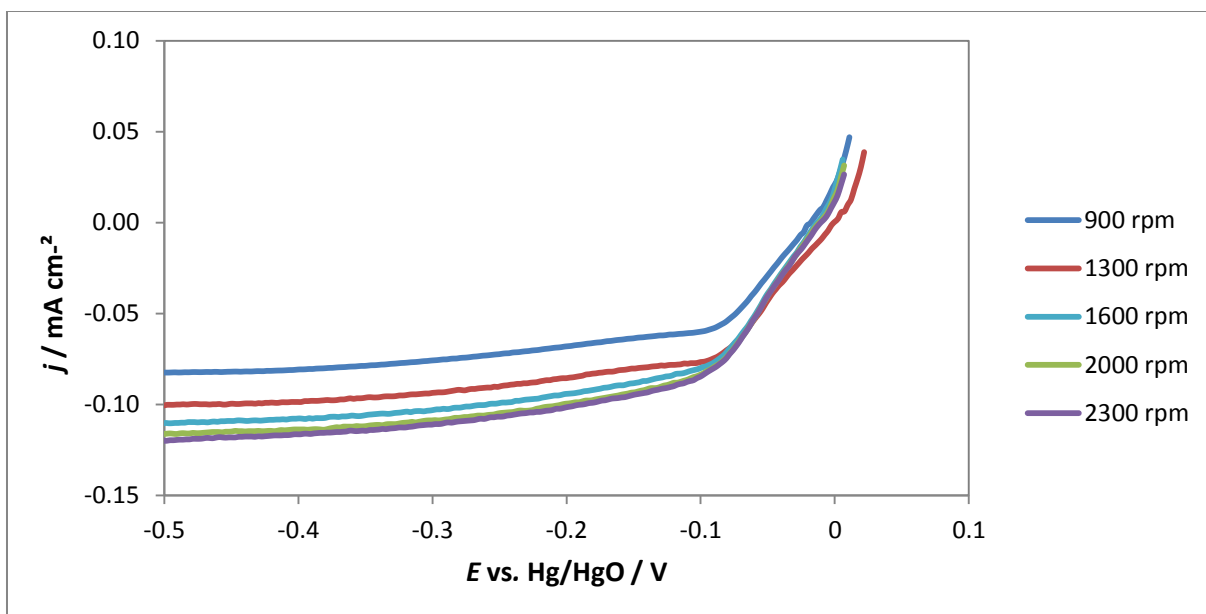


Figure 42: Voltammograms for ORR of P8 (300°C/NO₃/s) in 8 M KOH at RT with v of 5 mV s⁻¹ and different ω .

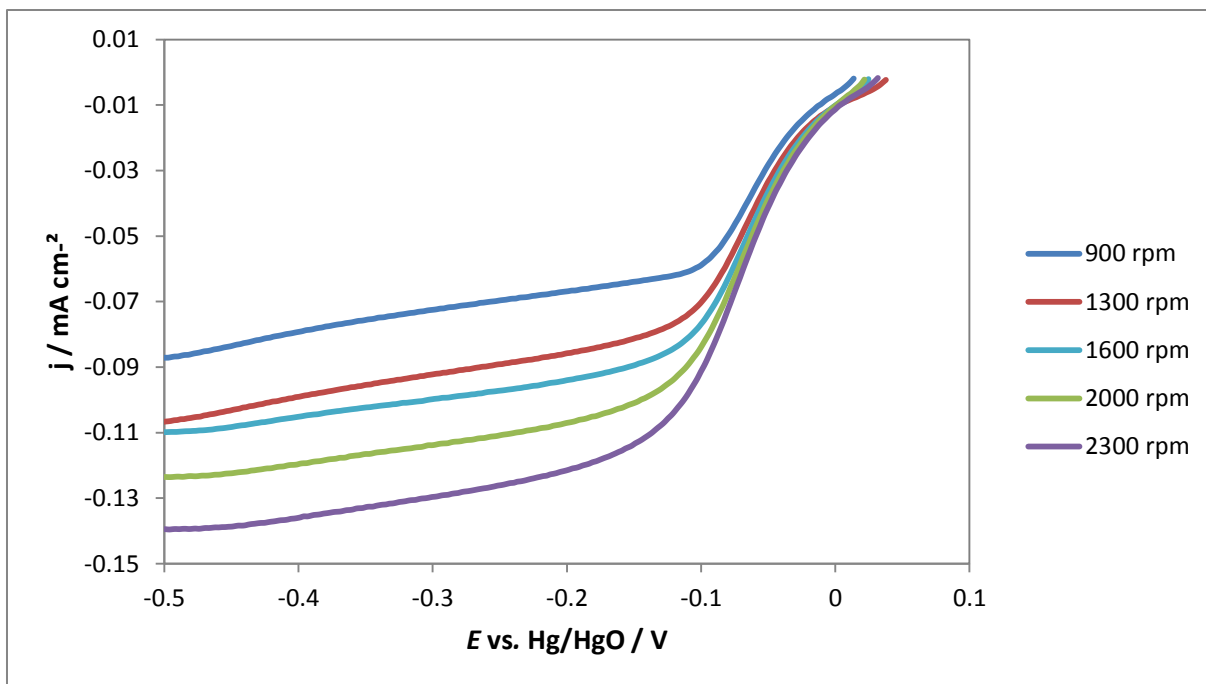


Figure 43: Voltammograms for ORR of P9 (375°C/OH/s) in 8 M KOH at RT with ν of 5 mV s^{-1} and different ω .

The comparison of the different catalysts at different rotation rates are shown in Figure 44 to Figure 46. No particular catalyst could be determined to be the best for the ORR but approximate trends could be observed. The catalyst P4 nearly shows higher limiting current densities at all rotation rates, especially at 900 rpm. The current densities of the sample P3 are also in the higher range. The catalysts P2_BK and P8 show lower current densities while that of the sample P7 is in the middle range.

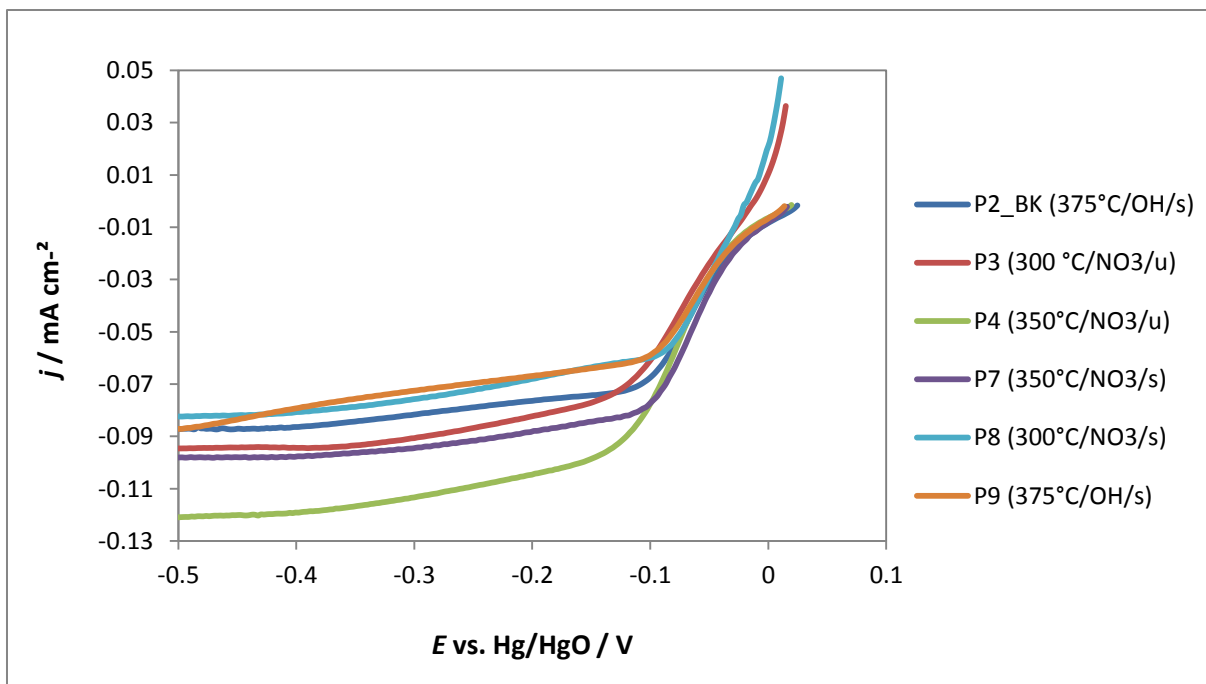


Figure 44: Comparison of the voltammograms of ORR of the different NiCo_2O_4 spinels in 8 M KOH at RT with v of 5 mV s^{-1} and ω of 900 rpm.

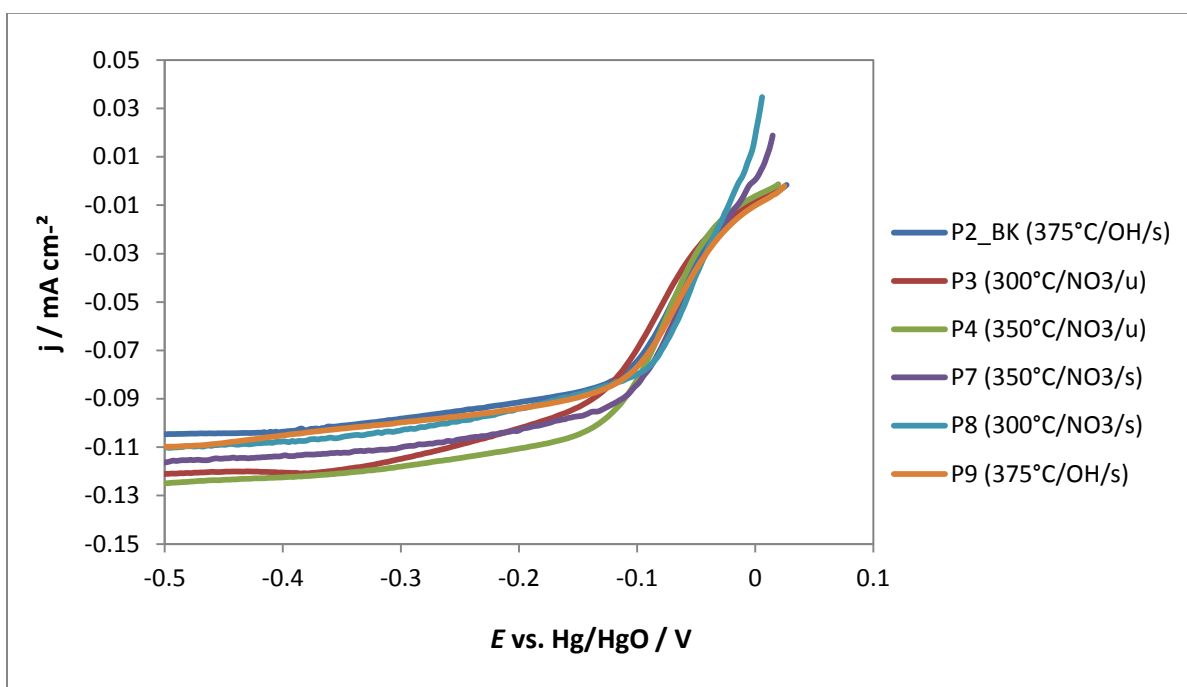


Figure 45: Comparison of the voltammograms of ORR of the different NiCo_2O_4 spinels in 8 M KOH at RT with v of 5 mV s^{-1} and ω of 1600 rpm.

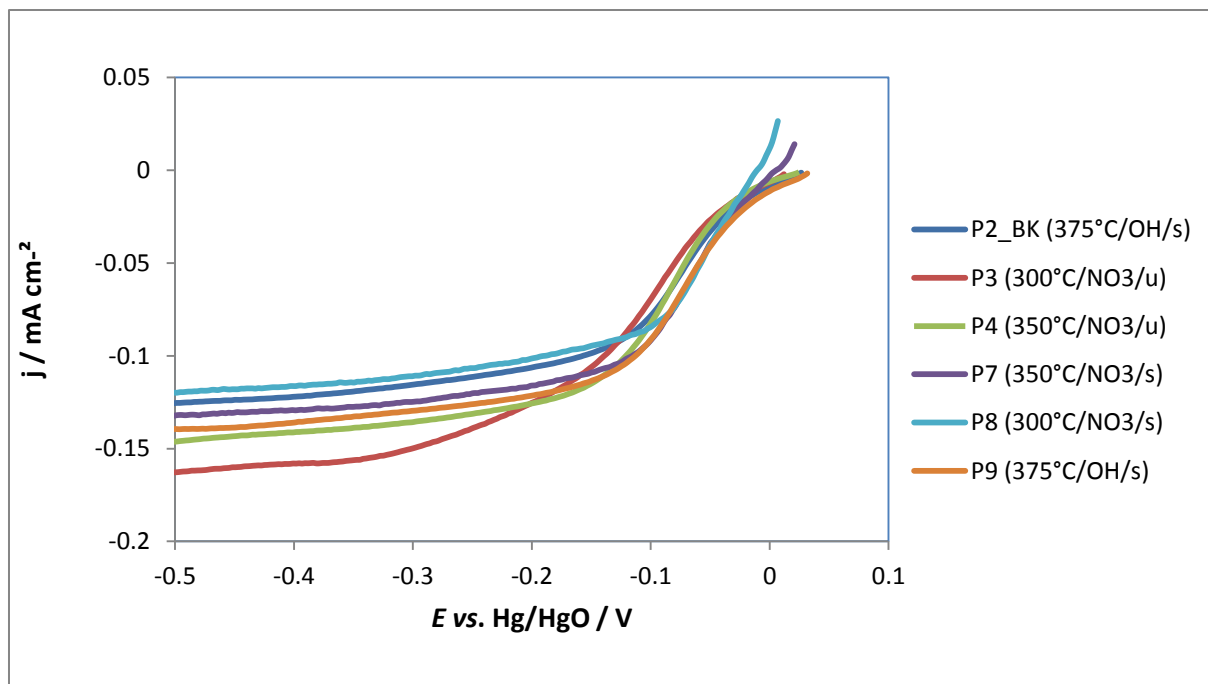


Figure 46: Comparison of the voltammograms of ORR of the different NiCo_2O_4 spinels in 8 M KOH at RT with ν of 5 mV s^{-1} and ω of 2300 rpm.

Figure 47 displays the comparison of the voltammograms of the OER of the different NiCo_2O_4 catalysts. The catalysts of the hydroxide method (P2_BK and P9) clearly show lower values of the overvoltage for OER than samples of the nitrate method. P9 has the lowest overvoltage of ~ 0.6 V vs. Hg/HgO. The samples P3, P4, P7 and P8 have an overvoltage of about 0.65 V vs. Hg/HgO.

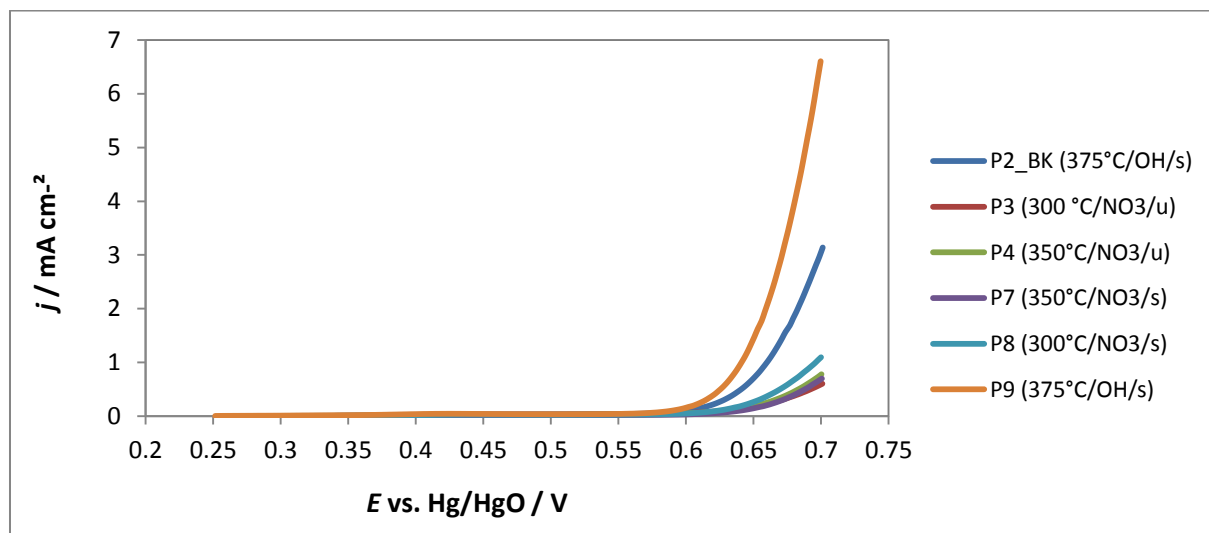


Figure 47: Comparison of the voltammograms of OER of the different NiCo_2O_4 spinels in 8 M KOH at RT with v of 5 mV s^{-1} and ω of 400 rpm.

4.1.4 Koutecky-Levich analysis

The data of the voltammograms of ORR of sample P2_BK (Figure 40), P8 (Figure 42) and P9 (Figure 43) at -0.5 V were used to draw the Koutecky-Levich plots (Figure 48 to Figure 50). The reciprocal limiting current density is plotted against the square root of the rotation rate. The straight line of all three plots is not intercepting with zero. This indicates that the ORR is mass transport and kinetically limited. Figure 51 displays the comparison of all three plots. Sample P9 shows the lowest value of intercept and is therefore less kinetically limited than the other two catalysts.

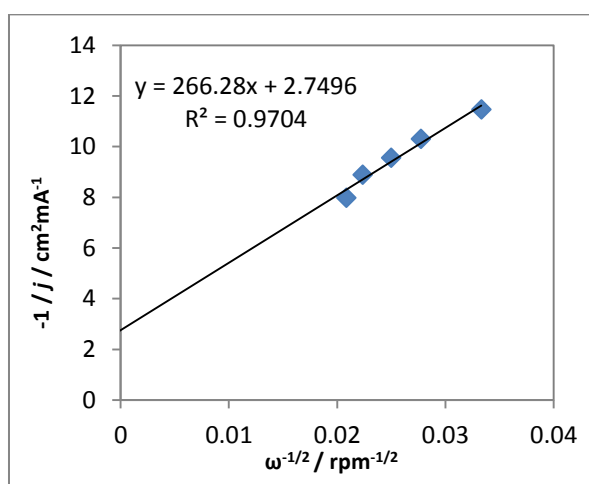


Figure 48: Koutecky-Levich plot of P2_BK (375°C/OH/s) in 8 M KOH at RT.

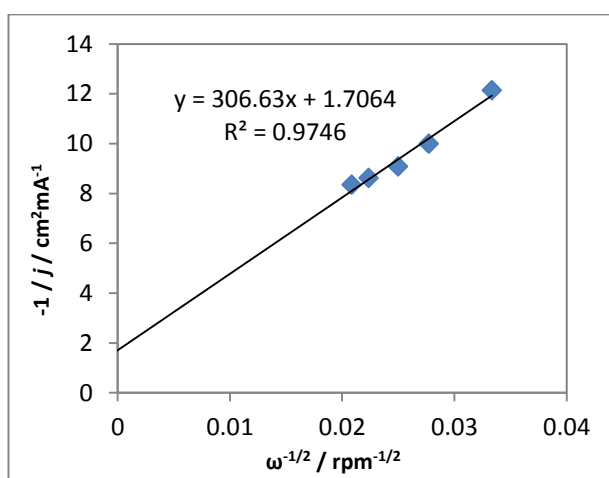


Figure 49: Koutecky-Levich plot of P8 (300°C/NO₃/s) in 8 M KOH at RT.

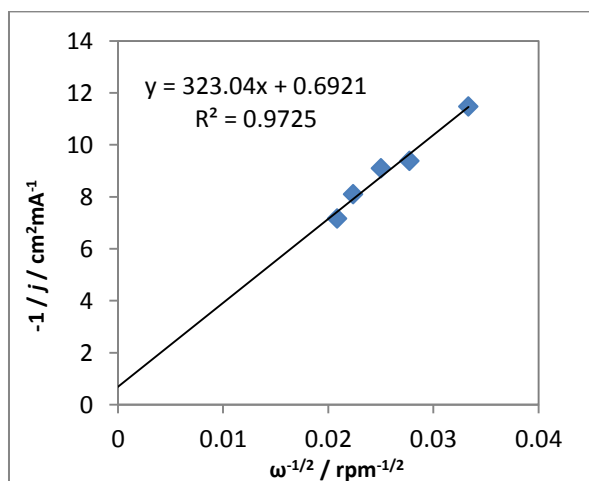


Figure 50: Koutecky-Levich plot of P9 (375°C/OH/s) in 8 M KOH at RT.

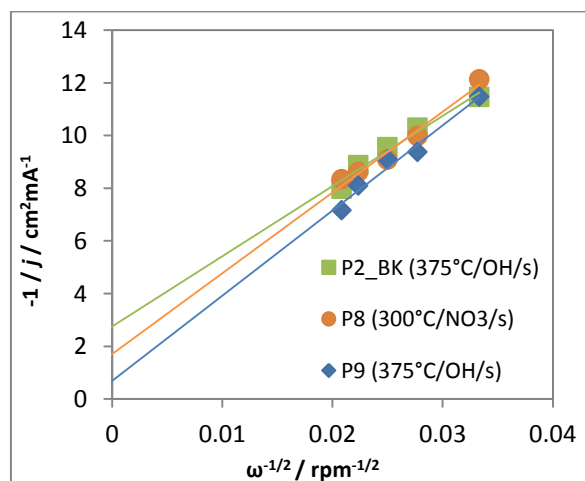


Figure 51: Comparison of the Koutecky-Levich plot of, P2_BK (375°C/OH/s), P7 (350°C/NO₃/s), P8 (300°C/NO₃/s) and P9 (375°C/OH/s) in 8 M KOH at RT.

4.1.5 ORR and OER in C-OAc, C-SO₄ and C-CO₃

In Figure 52, the voltammograms of ORR of the catalyst P7 are compared with the ones of the bare RDE in C-OAc, C-SO₄ and C-CO₃. The limiting current density of P7 in choline acetate is notably higher than for the bare RDE. In contrast, the difference in choline sulphate is much smaller. In choline carbonate, the value of the bare RDE is even higher as the one with the catalyst P7. The limiting current density in C-CO₃ is the highest, followed by C-OAc and finally C-SO₄.

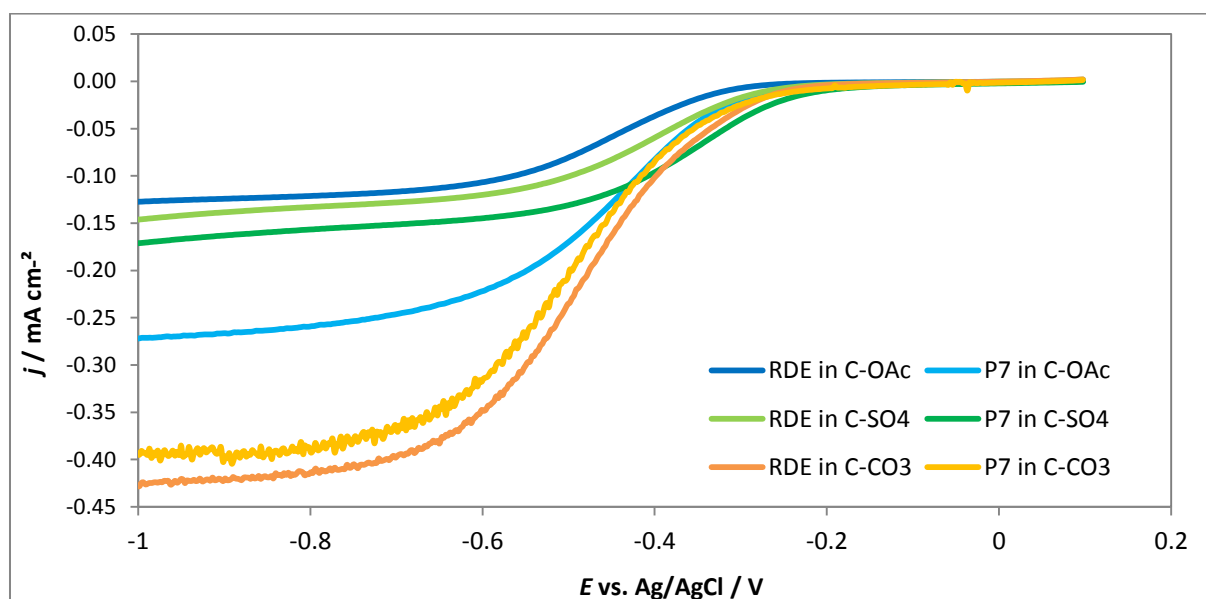


Figure 52: Comparison of the voltammograms of ORR of P7 (350°C/NO₃/s) and the bare RDE in choline acetate, - sulphate and - carbonate at RT with ν of 5 mV s^{-1} and ω of 900 rpm.

Figure 53 displays the same voltammograms with another scale. It can be seen, that the ORR of P7 in C-CO₃ and C-SO₄ starts at a lower potential followed by P7 in C-OAc. Next are the bare RDE in C-CO₃ and C-SO₄. The ORR of the bare RDE in C-OAc began at the most negative potential.

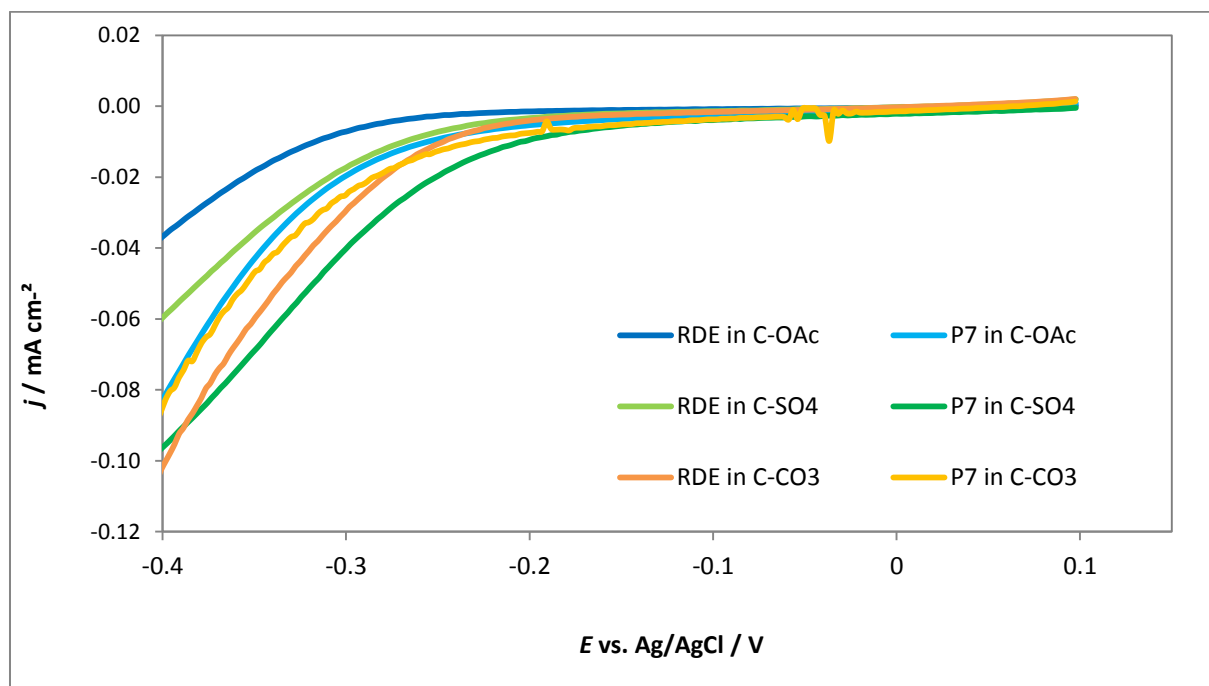


Figure 53: Comparison of the voltammograms of ORR of P7 (350°C/NO₃/s) and the bare RDE in choline acetate, - sulphate and - carbonate at RT with ν of 5 mV s⁻¹ and ω of 900 rpm in another scale.

The voltammograms of OER of P7 and the uncoated RDE in different choline electrolytes are displayed in Figure 54. In Figure 55 the same voltammograms are shown in another scale. The onset potential for the OER of P7 in C-CO₃ is about 0.9 V vs. Ag/AgCl but the difference of the voltammogram of the catalyst and the bare RDE is very small. The value of P7 in C-SO₄ is also about 0.9 V vs. Ag/AgCl but the rising is more flat as in choline carbonate. In contrast, in C-OAc the onset potential is about 1.3 V vs. Ag/AgCl. In all three electrolytes, the overvoltage of P7 is lower than for the bare RDE, especially in choline sulphate. These results indicate that P7 catalyses the OER in C-SO₄ at the lowest overvoltage. The overvoltage for the OER in the choline electrolytes in comparison to 8 M KOH (about 0.65 V vs. Hg/HgO) is considerably higher.

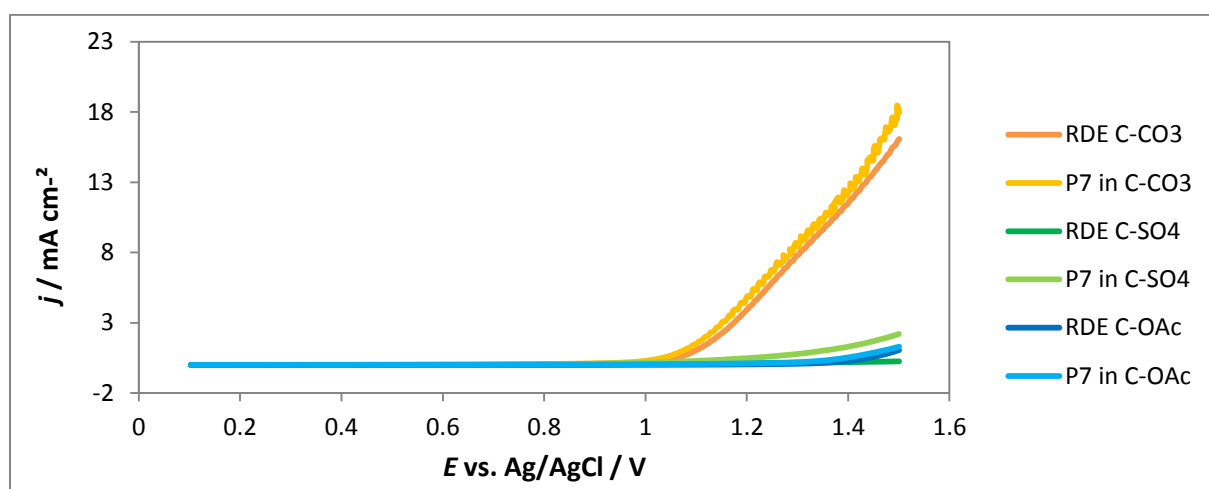


Figure 54: Comparison of the voltammograms of OER of P7 (350°C/NO₃/s) in choline acetate, - sulphate and - carbonate at RT with v of 5 mV s⁻¹ and ω of 400 rpm.

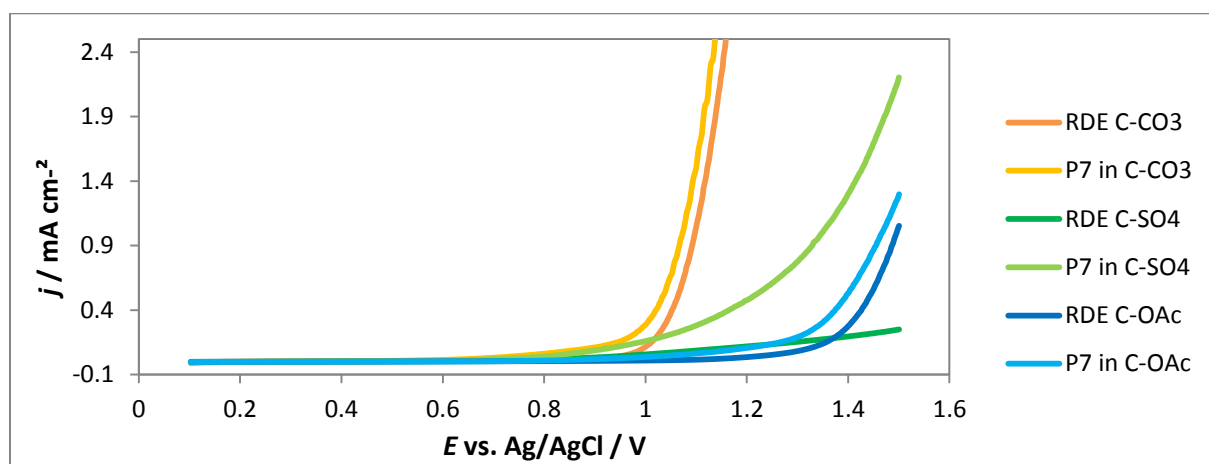


Figure 55: Comparison of the voltammograms of OER of P7 (350°C/NO₃/s) in choline acetate, - sulphate and - carbonate at RT with v of 5 mV s⁻¹ and ω of 400 rpm in another scale.

4.2 Electrochemical measurements – rotating ring-disc electrode

4.2.1 Collection efficiency

The CV of the ferrocyanide/ferricyanide redox system in 0.1 M KCl at RT is illustrated in Figure 56. After the CV measurement, voltammograms for the determination of the collection efficiency were recorded. The potential of the ring was fixed at 0.5 V vs. Ag/AgCl. At this potential the oxidation of $\text{Fe}(\text{CN})_6^{4-}$ to $\text{Fe}(\text{CN})_6^{3-}$ occurs on the Pt ring. The voltammograms of the ring and disc are shown in Figure 57. The measurements were carried out at different rotation rates of the RRDE. The limiting currents regarding ring and disc were used to calculate the collection efficiency N according to equation (29). The results of N of the different rotation rates are summarized in Table 2. The average value of the collection efficiency is 25.4 %. This value fits very well with the theoretical collection efficiency of the manufacturer (based on the geometrical values of the RDE) of 25.6% [52].

$$\frac{I_{ring}}{I_{disc}} * 100 = N\% \quad (29)$$

Table 2: Values for the determination of the collection efficiency of the RRDE.

rpm	$I_{ring} / \mu\text{A}$	$I_{disc} / \mu\text{A}$	N %
100	36	139	25.9
300	62	244	25.3
500	79	316	25.1
			25.4±0.3

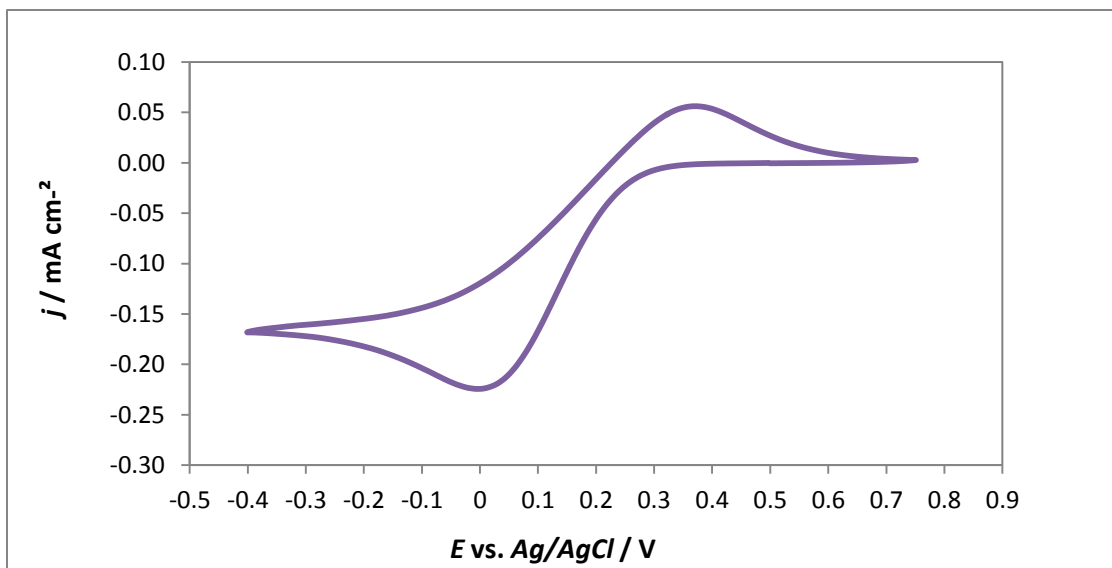


Figure 56: CV of the ferrocyanide/ferricyanide redox-pair in 0.1 M KCl at RT with v of 10 mV s^{-1} .

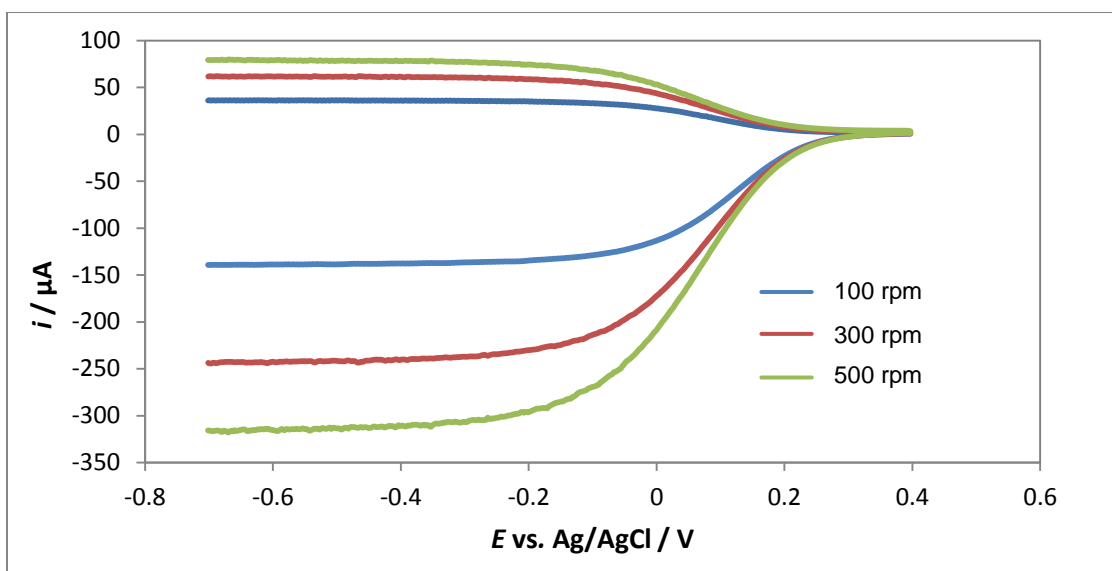


Figure 57: Voltammograms of the ring and disc of the ferrocyanide/ferricyanide system in 0.1 M KCl at RT with v of 10 mV s^{-1} and different ω .

4.2.2 Peroxide detection

The determination of the amount of formed peroxide during ORR was performed by RRDE. The catalyst P7 was examined in 8 M KOH as well as in C-OAc. The potential of the ring was fixed at 0.2 V vs. Hg/HgO, where the oxidation on Pt is mass transport controlled [50] in 8 M KOH. In C-OAc, the ring potential was held constant at 0.7 V vs. Ag/AgCl. This value was experimentally determined by preliminary tests. The voltammograms of P7 of the ring and the disc in 8 M KOH are shown in Figure 58 and Figure 59. The current of the disc increases with increasing rotation rate. The curves of 2500 rpm and 3000 rpm are more closely to each other. Corresponding to the Levich equation (17), the current density increases linearly with the square root of the rotation rate. The ring current increases with increasing rotation rate but at higher rotation rates the distance gets smaller. In the range of -0.2 to -0.5 V vs. Hg/HgO the limiting current is reached and therefore, the ORR is mass transport controlled. The values of the current at -0.5 V vs. Hg/HgO were used to calculate the percentage of peroxide formed and the number of transferred electrons (equation (30) and (31)). The results are summarized in Table 3. The percentage of H₂O₂ is between 39.4 % and 46.8%. This indicates that a notable amount of oxygen is reduced over the two-electron pathway. The number of transferred electrons during ORR is around 3.1-3.2.

$$\frac{2 * I_R / N}{I_D + I_R / N} * 100 = H_2O_2\% \quad (30)$$

$$n_{e^-} = \frac{4 * I_D}{I_D + I_R / N} \quad (31)$$

N...Collection efficiency (N= 0.254, determined in 4.2.1)

I_R...Ring current

I_D...Disc current

n_{e⁻}...Number of transferred electrons

Table 3: Percentage of formed peroxide and number of transferred electrons of P7 in 8 M KOH.

rpm	<i>I_R</i> / μA	<i>I_D</i> / μA	H ₂ O ₂ / %	<i>n e⁻</i>
100	0.628	10.07	39.37	3.21
400	1.026	13.43	46.23	3.08

900	1.232	15.90	46.75	3.07
1600	1.243	18.15	42.45	3.15
2500	1.335	20.09	41.46	3.17
3000	1.341	20.76	40.53	3.19

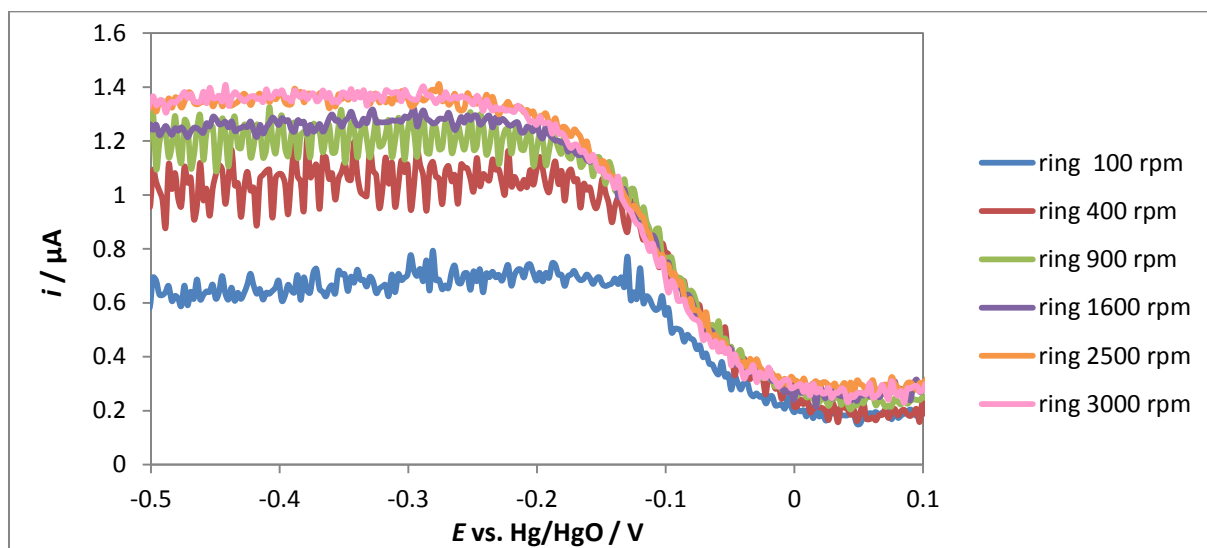


Figure 58: RRDE voltammograms (ring) of P7 (350°C/NO₃/s) in 8 M KOH at RT with v of 5 mV s⁻¹ and different ω .

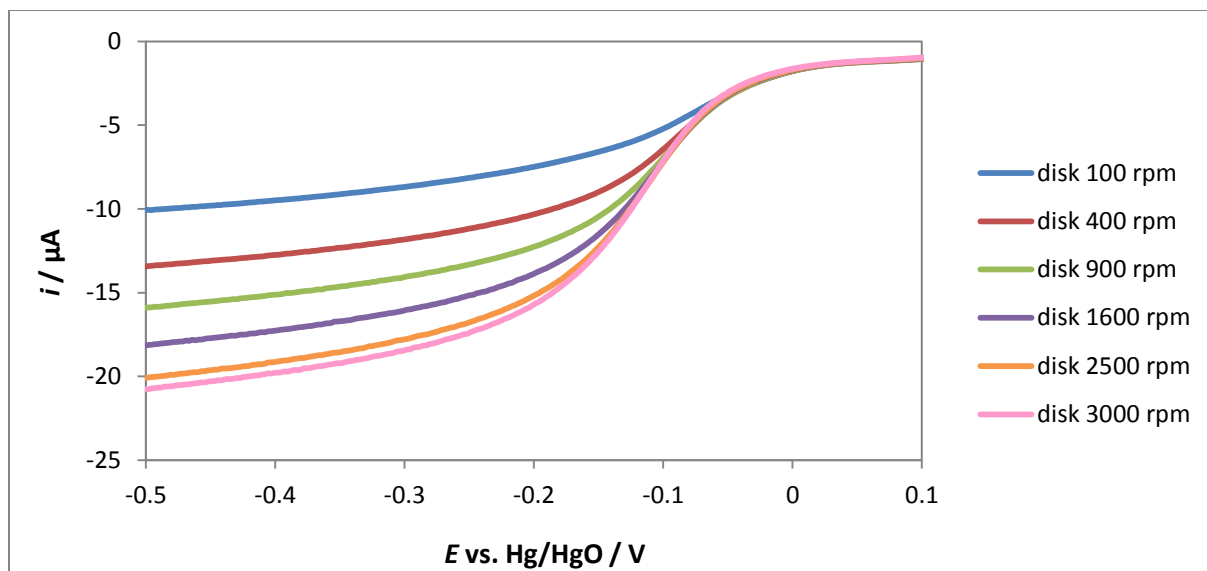


Figure 59: RRDE voltammograms (disc) of P7 (350°C/NO₃/s) in 8 M KOH at RT with v of 5 mV s⁻¹ and different ω .

In Figure 60 and Figure 61, the voltammograms of P7 in C-OAc of the ring and the disc are illustrated, respectively. The limiting current of the disc increases with increasing rotation rate up to 1600 rpm. For the ring, an increase of the current could only be observed at 100, 900 and 1600 rpm. The curve of 400 rpm shows the highest values but also the biggest scattering. An almost limiting current region was only observed at 100 and 900 rpm and therefore, the calculation of the percentage of formed peroxide was only possible for these two curves. Table 4 displays the current values, the results of formed peroxide and the number of transferred electrons. The ring current used for the calculation was averaged between 0.78-0.82 V. The percentage of formed peroxide ranges from 20.8 % to 33.2 %. The number of transferred electrons is 3.3 to 3.6. Due to the fact that the voltammograms of the ring did not show the expected behaviour, only an estimation could be made.

Table 4: Values of formed peroxide and number of electrons of P7 in C-OAc.

rpm	$I_R / \mu\text{A}$	$I_D / \mu\text{A}$	$\text{H}_2\text{O}_2 / \%$	$n e^-$
100	0.867	17.11	33.23	3.34
900	1.116	37.90	20.77	3.58

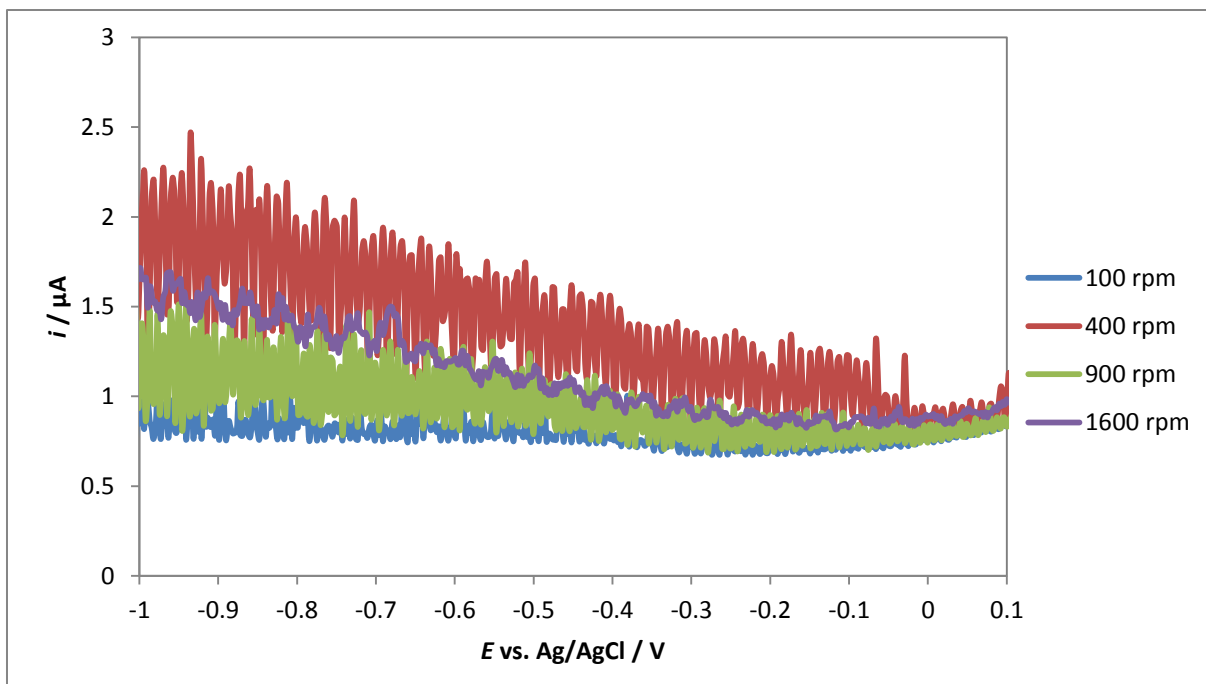


Figure 60: RRDE voltammograms (ring) of P7 (350°C/NO₃/s) in C-OAc at RT with v of 5 mV·s⁻¹ and different ω .

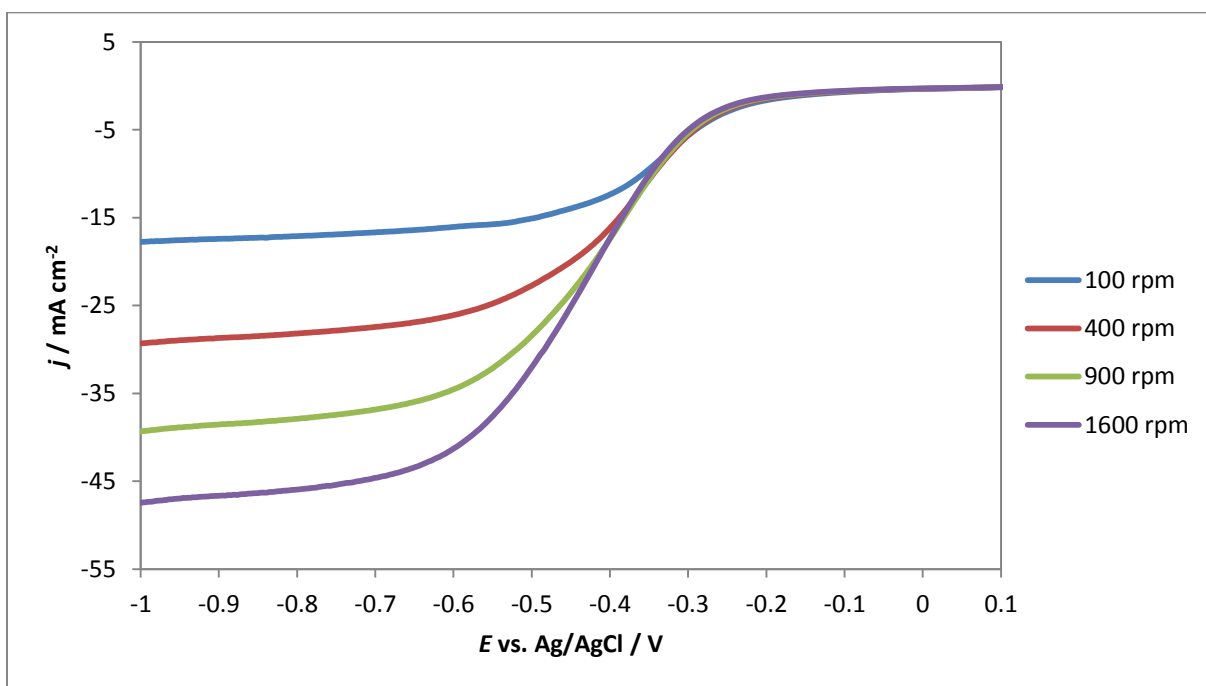


Figure 61: RRDE voltammograms (disc) of P7 (350°C/NO₃/s) in C-OAc at RT with v of 5 mV s⁻¹ and different ω .

4.3 Physicochemical characterisations

4.3.1 XRD measurements

Figure 62 to Figure 67 show the XRD diffractograms of the different catalyst samples. The patterns of reflexes show that the structure of all catalyst samples is a NiCo_2O_4 spinel. The values of the lattice constant of the different samples fit with those of the literature of the cubic unit cell of the NiCo_2O_4 [53]. The lattice constant and the crystallite size are summarized in Table 5. The crystallite size was determined with the Debye-Scherrer approximation [54,55]. The results show, that the hydroxide method leads to a lower size of crystallite. The sieving process before calcination has large influence on the resulting crystallite size. The samples P3 and P4 display higher crystallite sizes. The diffractograms of the samples prepared with the nitrate method (Figure 64 to Figure 67) show narrow reflexes. In contrast, the XRD patterns of the samples prepared with the hydroxide method (Figure 62 and Figure 63) show broad reflexes and the background signals are high which indicates that the samples have amorphous parts. These results indicate that a higher degree of crystallinity can be yielded with the nitrate method.

Table 5: Lattice constant and crystallite size of the NiCo_2O_4 spinels.

	Lattice constant / Å	Crystallite size / Å
P2_BK (375°C/OH/s)	8.115	110
P3 (300°C/ NO_3 /u)	8.119	1200
P4 (350°C/ NO_3 /u)	8.119	1080
P7 (350°C/ NO_3 /s)	8.119	330
P8 (300°C/ NO_3 /s)	8.119	820
P9 (375°C/OH/s)	8.118	90
Literature [53]	8.114	-

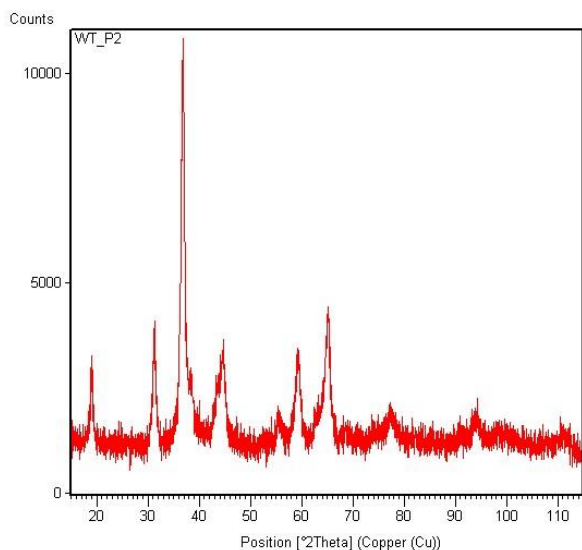


Figure 62: XRD pattern of the spinel P2_BK (375°C/OH/s).

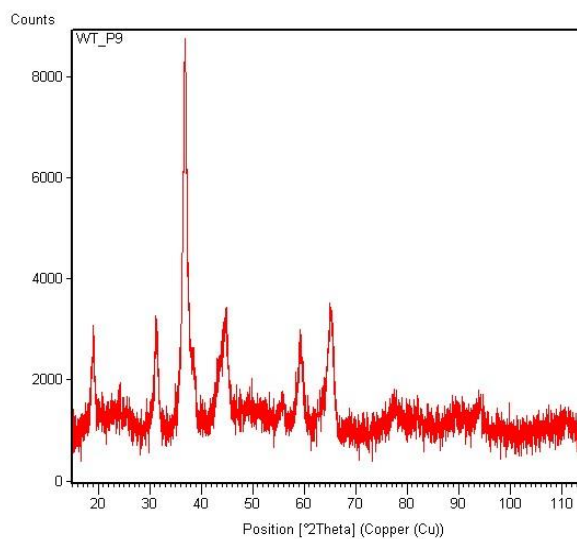


Figure 63: XRD pattern of the spinel P9 (375°C/OH/s).

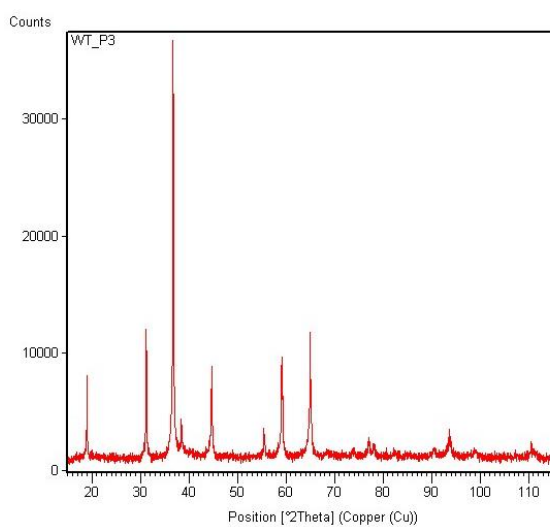


Figure 64: XRD pattern of the spinel P3 (300°C/NO₃/u).

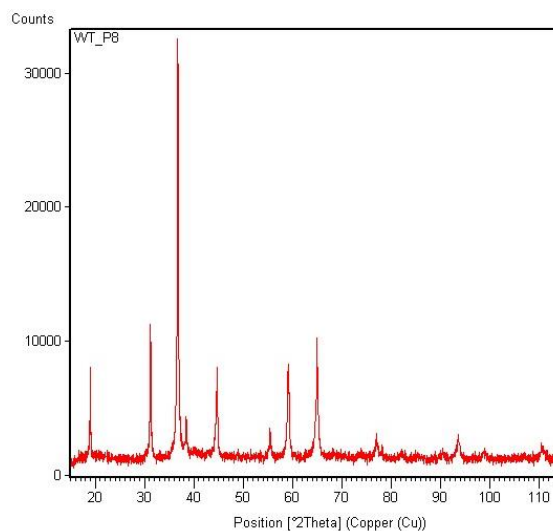


Figure 65: XRD pattern of the spinel P8 (300°C/NO₃/s).

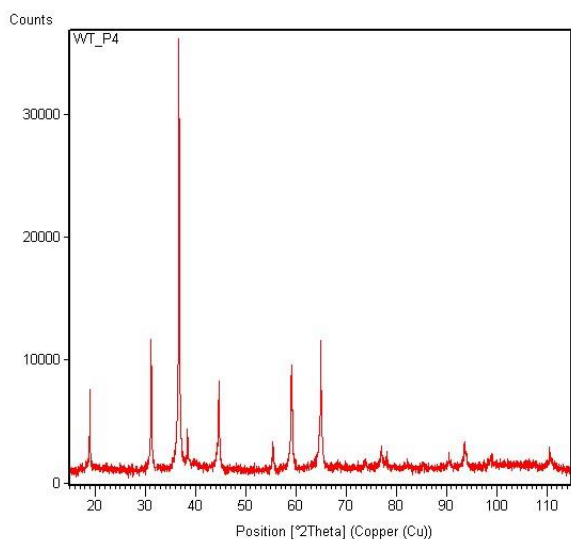


Figure 66: XRD pattern of the spinel P4 (350°C/NO₃/u).

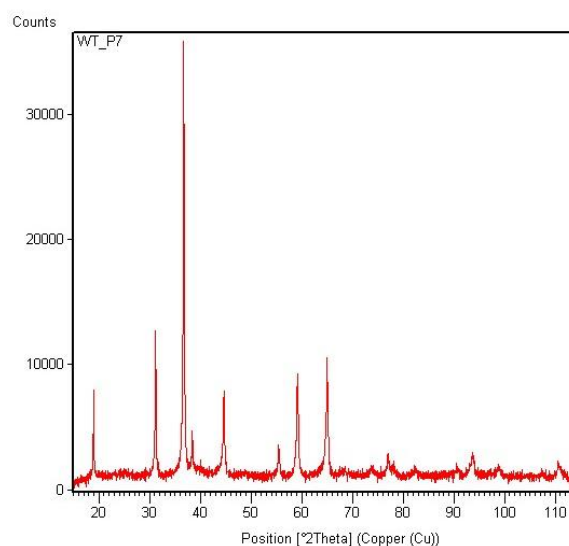


Figure 67: XRD pattern of the spinel P7 (350°C/NO₃/s).

4.3.2 BET measurements

The results of the BET measurements are summarized in Table 6. The samples P2_BK and P9, prepared with the hydroxide method, show the highest values for the BET surface area while the samples P4 and P7 show the lowest values. Comparison of the surface areas of the samples prepared with the nitrate method indicate that a lower calcination temperature (P3 and P8) results in a higher surface area. The literature also describes that samples prepared with the same method at higher preparation temperature lead to lower surface area [56]. The average particle size of the NiCo₂O₄ spinel can be calculated from the relation between the BET surface area and the theoretical density (literature value: $\rho = 5.98 \text{ g cm}^{-3}$ [53]). The particles are assumed to be spheres [57]. The results are summarized in Table 6. It can be seen that the higher the surface area the lower the particle size.

$$SSA_{\text{BET}} = \frac{\text{particle surface}}{\text{particle mass}} \left[\frac{\text{m}^2}{\text{g}} \right] \quad (32)$$

$$SSA_{\text{vol}} = \frac{\text{particle surface}}{\text{particle volumen}} \left[\frac{\text{m}^2}{\text{m}^3} \right] \quad (33)$$

$$SSA_{\text{vol}} = \frac{\pi * d^2}{\frac{\pi * d^3}{6}} = \frac{6}{d} \left[\frac{1}{\text{m}} \right] \quad (34)$$

$$SSA_{\text{vol}} = \rho_{\text{spinel}} * SSA_{\text{BET}} \quad (35)$$

$$\frac{6}{d} = \rho_{\text{spinel}} * SSA_{\text{BET}}$$

$$\text{particle surface} = \pi * d^2$$

$$\text{particle volume} = \frac{\pi * d^3}{6}$$

$$\rightarrow d = \frac{6}{\rho_{\text{spinel}} * SSA_{\text{BET}}}$$

Table 6: BET area and mean particle size of the NiCo₂O₄ spinels.

Sample	BET surface / m ² g ⁻¹	Mean particle size / nm
P2_BK (375°C/OH/s)	40	25
P3 (300°C/NO ₃ /u)	34	30
P4 (350°C/NO ₃ /u)	23	44
P7 (350°C/NO ₃ /s)	21	48
P8 (300°C/NO ₃ /s)	36	28
P9 (375°C/OH/s)	49	20

4.3.3 Particle size distribution

The particle size distribution of the different samples is shown in Figure 68 to Figure 73. The samples (P3, P4, P7 and P8) prepared with the nitrate method (Figure 69 to Figure 72) display a similar particle size distribution pattern of a polydisperse distribution with more than one peak. The sample P8 has larger particles. In contrast, the samples P2_BK and P9 that were prepared with the hydroxide method (Figure 68 and Figure 73) show only one peak and have a monodisperse distribution of the particles. A clear trend of particle size distribution related to the preparation method could be observed.

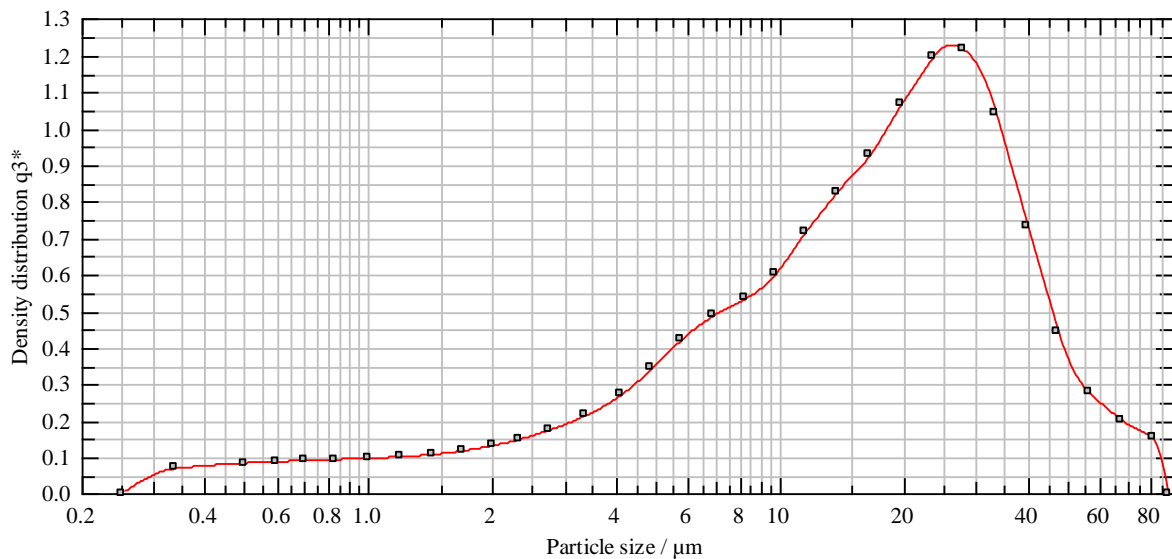


Figure 68: Particle size distribution of P2_BK (375°C/OH/s).

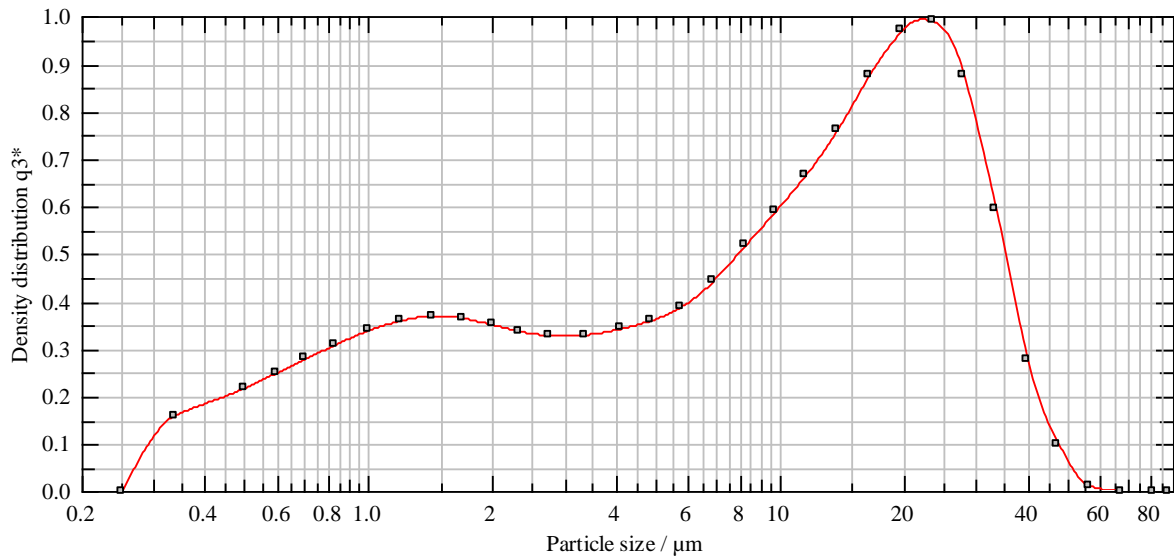


Figure 69: Particle size distribution of P3 (300°C/NO₃/u).

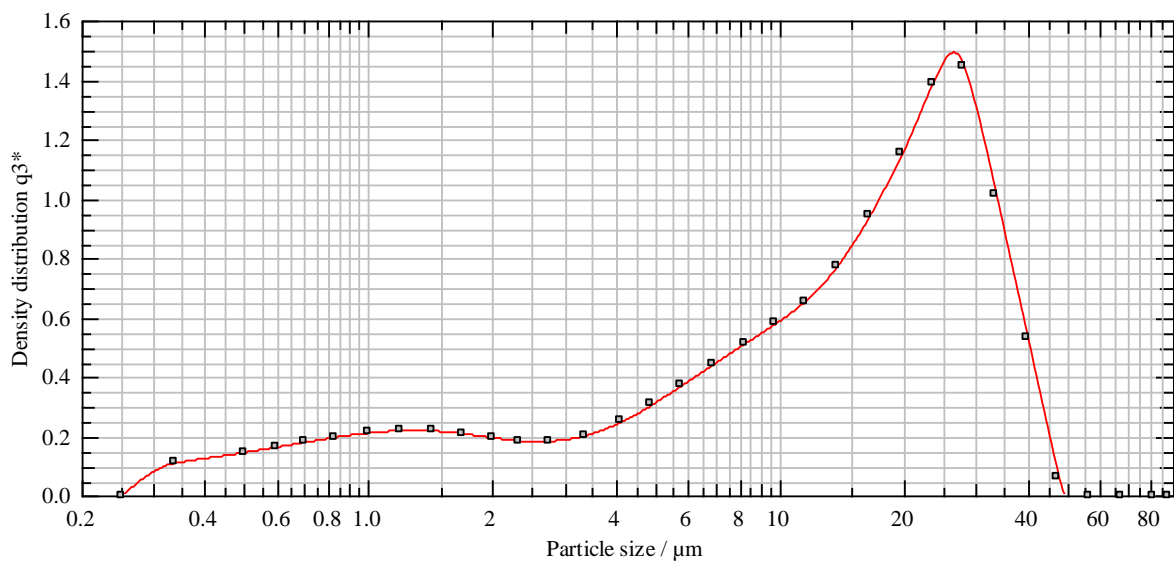


Figure 70: Particle size distribution of P4 (350°C/NO₃/u).

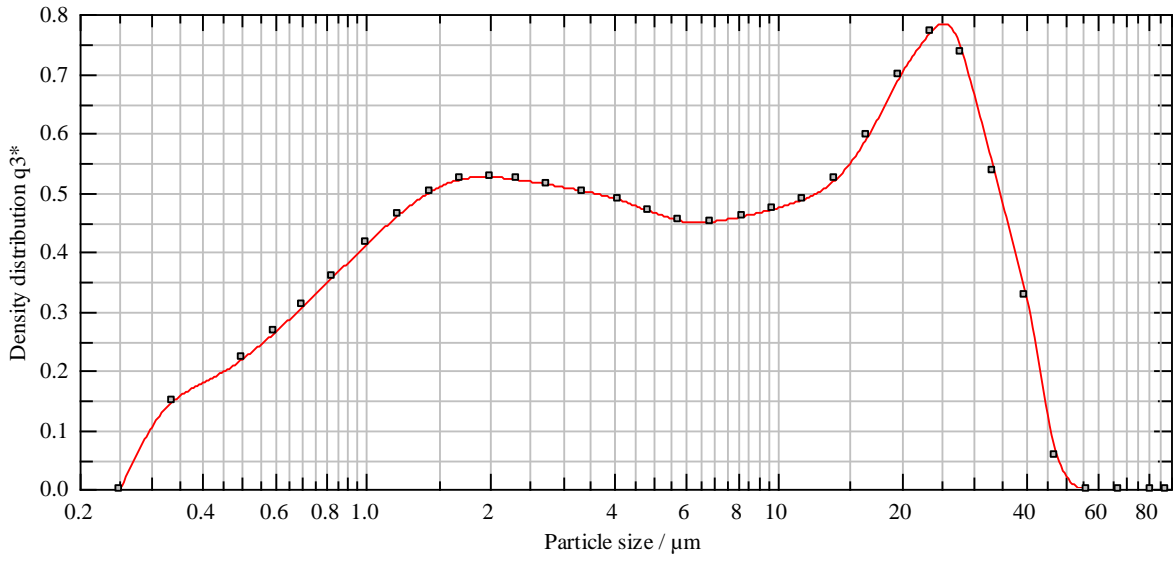


Figure 71: Particle size distribution of P7 (350°C/NO₃/s).

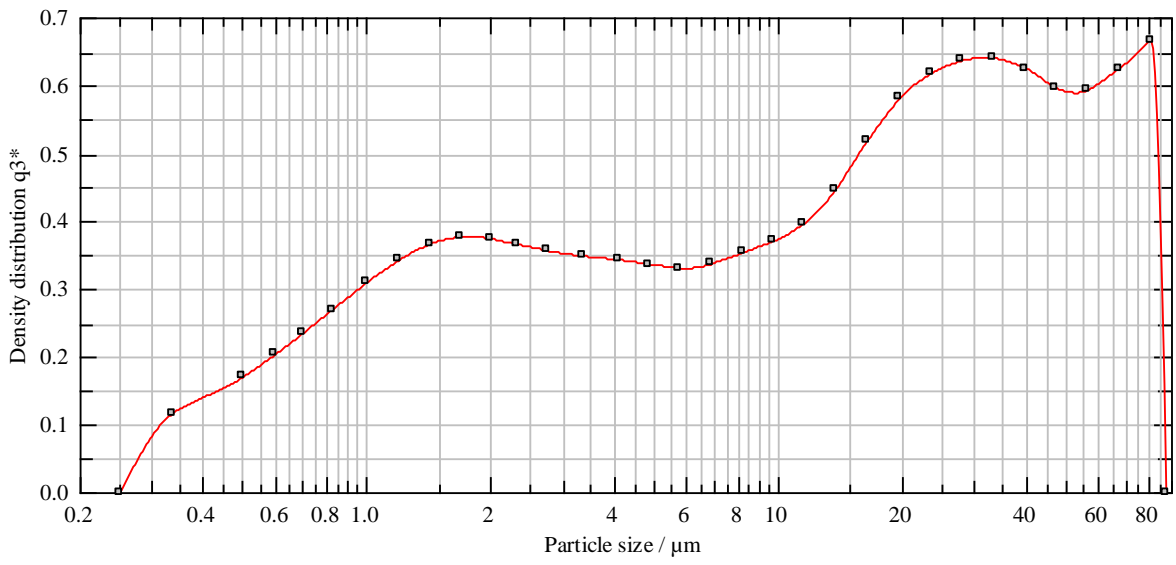


Figure 72: Particle size distribution of P8 (300°C/NO₃/s).

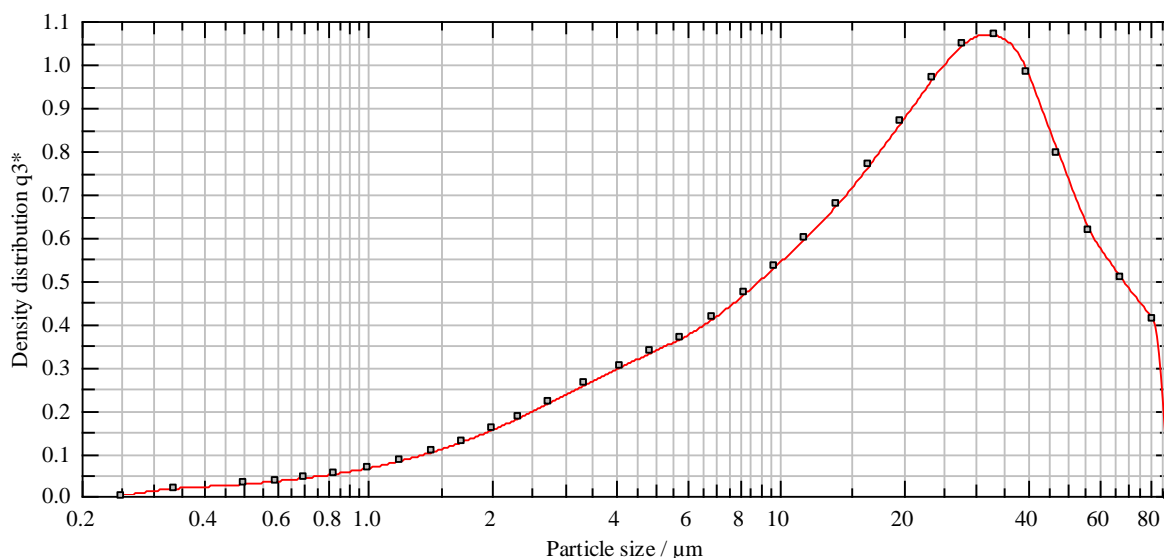


Figure 73: Particle size distribution of P9 (375°C/OH/s).

4.3.4 Scanning electron microscopy

Photographs of the different catalysts recorded with scanning electron microscopy (SEM) are shown in Figure 74 to Figure 79. The images of the sample P3 (Figure 75), P4 (Figure 76), P7 (Figure 77) and P8 (Figure 78), prepared with the nitrate method, show that these spinels have smaller, spherical particles with a size of about 1 μm . In contrast, the samples P2_BK (Figure 74) and P9 (Figure 79) of the hydroxide method are more plate-shaped with larger agglomerates. This results show the influence of the preparation method on the particle shape and size.

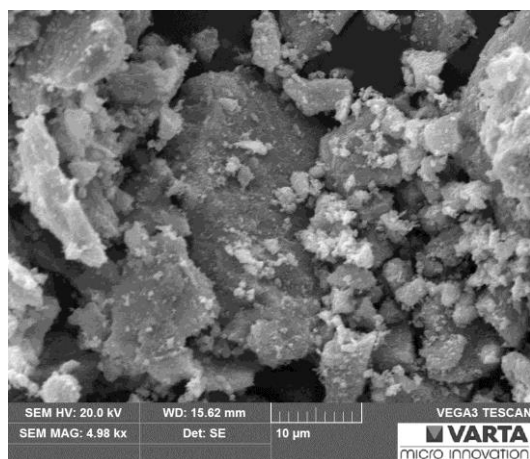


Figure 74: SEM micrograph of P2_BK (375°C/OH/s) with 5000x magnification.

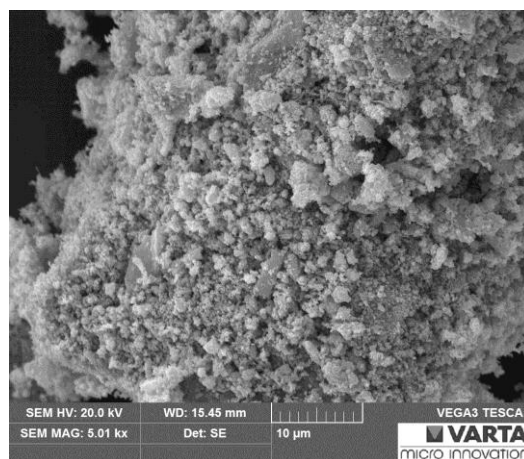


Figure 75: SEM micrograph of P3 (300°C/NO₃/u) with 5000x magnification.

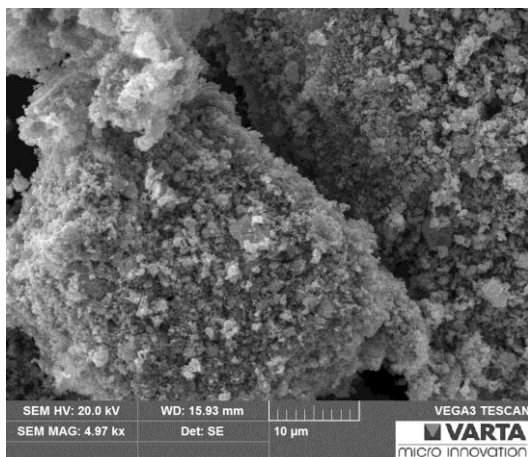


Figure 76: SEM micrograph of P4 (350°C/NO₃/u) with 5000x magnification.

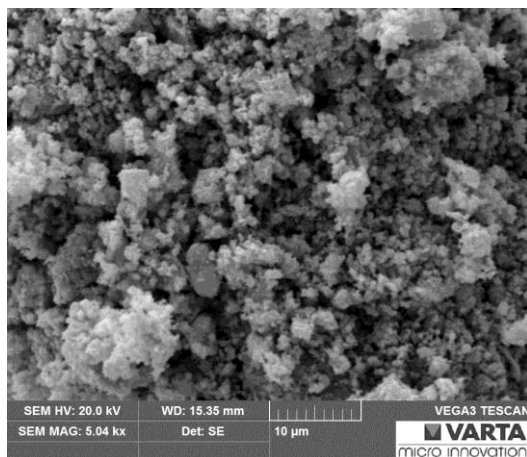


Figure 77: SEM micrograph of P7 (350°C/NO₃/s) with 5000x magnification.

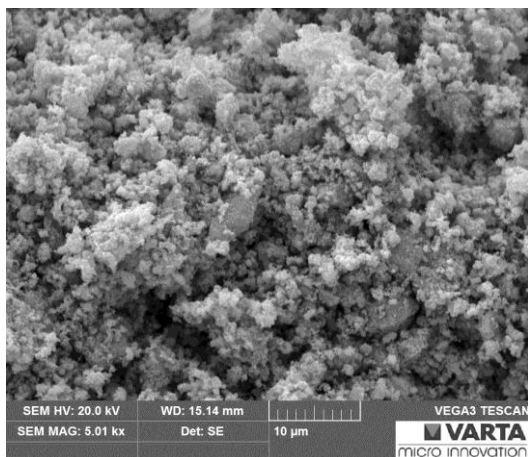


Figure 78: SEM micrograph of P8 (300°C/NO₃/s) with 5000x magnification.

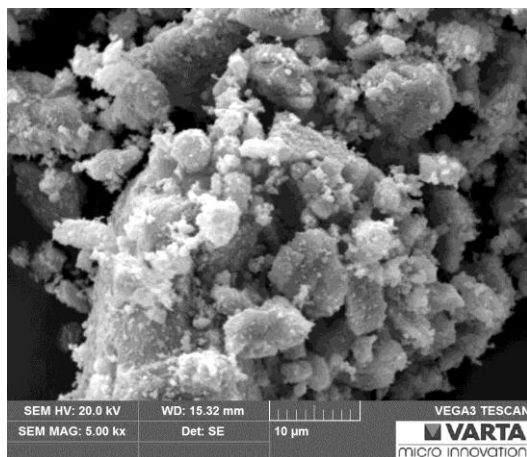


Figure 79: SEM micrograph of P9 (375°C/OH/s) with 5000x magnification.

5 Summary

The differently prepared NiCo_2O_4 spinel catalysts were investigated to determine their usability as bifunctional catalysts for the air electrode of a zinc-air redox flow battery. The catalyst samples were prepared with two different methods, the nitrate and hydroxide method. The starting materials for both were nickel and cobalt nitrate hexahydrate salts. In the case of the nitrate method, the salts were dissolved in methanol and then the solvent was evaporated. For the hydroxide method, the salts were dissolved in deionised water and precipitated with sodium hydroxide. In both methods, the resulting powder was crushed before calcination at various temperatures.

Cyclic voltammetry (CV) and rotating disc electrode experiments in order to study the oxygen reduction reaction (ORR) and oxygen evolution reaction (OER) of the catalysts were conducted in 8 M KOH. For one catalyst that was prepared with the nitrate method, the electrochemical measurements were carried out in different neutral choline based electrolytes. Furthermore, experiments with the rotating ring-disc electrode were performed to investigate the type of reduction of the ORR (two- or four-electron pathway). The amount of peroxide formation during ORR of one catalyst of the nitrate method was determined in 8 M KOH as well as in choline acetate.

The CV studies in 8 M KOH have displayed that all catalysts show Ni- and Co-oxidation-/reduction peaks. From the comparison of the CVs of the different catalysts it could be observed that the catalysts prepared with the nitrate method at the same calcination temperature (sieved/unsieved sample) show very similar peak heights. The peaks of catalysts calcined at lower temperature were much larger. One sample of the hydroxide method illustrated the highest peak current density. The cycle stability of the spinel samples was also examined by comparison of the first and the tenth cycle. One catalyst of the nitrate method (P3, 300°C) illustrated higher reductive and oxidative peaks in the tenth cycle. Other samples of the nitrate method (P4 and P7, 350°C) showed somewhat higher oxidative peaks. The reductive peaks of all catalysts were slightly higher in the tenth cycle.

For the ORR at different rotation rate, no particular catalyst showed better catalytic activity than all others, but approximate trends could be observed. The unsieved catalysts of the nitrate method show higher limiting current densities. The trend of increasing current density with increasing rotation rate could only be observed for samples of the hydroxide method and samples of the nitrate method calcined at 300°C. Koutecky-Levich plots were created for one catalyst of the nitrate method (P8, 300°C) and for the catalysts of the hydroxide method. The straight line of all three plots is not intercepting with zero which indicates that the ORR is mass transport and kinetically limited. The sample P9 of the hydroxide method shows the lowest value of intercept and is therefore less kinetically limited than the other two catalysts. The investigation of OER of the different catalysts in potassium hydroxide has shown that the catalysts prepared with the hydroxide method have a lower overvoltage of about 40 mV in comparison to that one prepared with the nitrate method.

The measurements of CVs in the three different neutral electrolytes have displayed that a reductive peak occurred only in the first cycle. A larger electrochemical window was also observed. The ORR and OER of one catalyst of the nitrate method and of the bare RDE were studied in choline acetate, choline sulphate and choline carbonate. In choline acetate, the catalyst illustrated a higher limiting current density for the ORR than for the bare RDE. In contrast, the difference between catalyst and uncoated RDE was much smaller in choline sulphate. In choline carbonate, the limiting current density of the bare RDE was even slightly higher than those of the catalyst. The overvoltage for the OER was approximately 300-400 mV larger than in the alkaline electrolyte. In choline carbonate and choline sulphate the smallest value was observed but in choline sulphate the increase of the current was more flat. In all three electrolytes, the overvoltage for OER of the catalyst was lower than those of the bare RDE.

The determination of the amount of peroxide formed during ORR was a special challenge. The voltammograms of the catalyst in 8 M KOH showed that the current of the disc electrode increases with increasing rotation rate. In choline acetate, the limiting currents of the disc also increase with increasing rotation rate up to 1600 rpm. For the ring, a limiting current like region was only observed at two different rotation rates and therefore, the formed peroxide was only determined for those curves. The

percentage of peroxide in 8 M KOH was 14-19 % higher than in choline acetate. Further experiments are required to investigate the peroxide formation in choline acetate to ensure proper characterization of the catalyst behaviour in this electrolyte.

The XRD measurements have shown that all NiCo_2O_4 catalysts have a spinel structure. The XRD patterns of the samples of the hydroxide method showed high background signals and broad reflexes which indicates that the samples have amorphous parts. In contrast, catalysts of the nitrate method showed narrow reflexes, which is an indication for crystallinity. The hydroxide method leads to a lower crystallite size. The BET results displayed that the samples of the hydroxide method show higher values for the BET surface area than samples of the nitrate method. From the BET data it can also be seen that samples prepared with the nitrate method at lower calcination temperature (300°C) have higher surface areas than those at higher calcination temperature (350°C). The particle size distribution (PSD) measurements have illustrated a clear trend of distribution that is related to the preparation method. The samples prepared with the nitrate method have a polydisperse distribution whereas samples of the hydroxide method show a monodisperse distribution of the particles. The images recorded with SEM have demonstrated that catalysts prepared by the nitrate method have smaller spherical particles of about $1\ \mu\text{m}$. In contrast, the samples prepared with the hydroxide method were more plate-shaped with larger agglomerates.

From all these results it can be seen that the preparation method and the type of electrolyte have a great influence on the properties of the bifunctional NiCo_2O_4 catalysts.

6 References

- [1] M.S. Guney, Y. Tepe, *Renewable and Sustainable Energy Reviews*, 75, (2017), 1187-1197.
- [2] N. Muralidharan, A.S. Westover, H. Sun, N. Galioto, R.E. Carter, A.P. Cohn, L. Oakes, C.L. Pint, *ACS Energy Letters*, 1, (2016), 1034-1041.
- [3] V. Fernão Pires, E. Romero-Cadaval, D. Vinnikov, I. Roasto, J.F. Martins, *Energy Conversion and Management*, 86, (2014), 453-475.
- [4] P. Alotto, M. Guarnieri, F. Moro, *Renewable and Sustainable Energy Reviews*, 29, (2014), 325-335.
- [5] J. Fu, P.Z. Cano, M.G. Park, A. Yu, M. Fowler, Z. Chen, *Advanced Materials*, 29, (2017), 1-34.
- [6] B. Gollas, W. Taucher-Mautner, B. Krenn, C. Zelger, B. Berner, V. Hacker, B. Pichler, H.J. Pauling, M. Schmuck, 2. Zwischenbericht, *LUZIFLOW Projekt*, Nr. 848933, Klima- und Energiefonds des Bundes - Abwicklung durch die Österreichische Forschungsförderungsgesellschaft FFG, (2017), 1-39.
- [7] A.Z. Weber, M. Matthew Mench, P. Jeremy Meyers, N. Philip Ross, T. Jeffrey Gostick, L. Qinghua, *Journal of Applied Electrochemistry*, 41, (2011), 1137-1164.
- [8] L.F. Arenas, C. Ponce de León, F.C. Walsh, *Journal of Energy Storage*, 11, (2017), 119-153.
- [9] Y. Li, H. Dai, *Chemical Society Reviews*, 43, (2014), 5256-5275.
- [10] V. Caramia, B. Bozzini, *Materials for Renewable and Sustainable Energy*, 3, (2014), 1-12.
- [11] O. Haas, J. Van Wesemael, in: J. Garche et al., *Encyclopedia of Electrochemical Power Sources*, Elsevier, Amsterdam, 4, (2009), 384-392.
- [12] P. Pei, K. Wang, Z. Ma, *Applied Energy*, 128, (2014), 315-324.
- [13] Y. Shuting, W.Z. Zhichao, O. Cao, M. Xinxin, S. Mengjiao, L. Yanlei, Z. Ruirui, Y. Yanhong, *Journal of Alloys and Compounds*, 721, (2017), 482-491.
- [14] J. Xiaodong, G. Shijie, L. Tongyuan, L. Dianqing, T. Pinggui, F. Yongjun, *Electrochimica Acta*, 245, (2017), 59-68.
- [15] F. Cheng, J. Shen, B. Peng, Y. Pan, Z. Tao, J. Chen, *Nature Chemistry*, 3, (2011), 79-84.
- [16] G. Zhang, Q. Wei, X. Yang, A.C. Tavares, S. Sun, *Applied Catalysis B: Environmental*, 206, (2017), 115-126.

- [17] F. Cheng, J. Chen, *Chemical Society Reviews*, 41, (2012), 2172-2192.
- [18] W. Schmickler, *Grundlagen der Elektrochemie*, Vieweg, Braunschweig, 1996, pp. 191-194.
- [19] Rudolf Holze, *Elektrochemisches Praktikum*, 1. Auflage, Teubner, Stuttgart, 2001, pp. 98-100.
- [20] K. Izutsu, *Overview of Electrochemical Techniques*, *Electrochemistry in Nonaqueous Solutions*, Wiley-VCH Verlag, 2009, pp. 111-170.
- [21] J. Wang, *Analytical Electrochemistry*, 3. Edition, John Wiley & Sons, New Jersey, 2006, pp. 29-42.
- [22] J. Nikolic, E. Expósito, J. Iniesta, J. González-García, V. Montiel, *Journal of Chemical Education*, 77, (2000), 1191-1194.
- [23] M. Prokop, R. Kodym, T. Bystron, M. Paidar, K. Bouzek, *Electrochimica Acta*, 245, (2017), 634-642.
- [24] M. Carpinella, M.I. Velasco, E.V. Silletta, J.M. Ovejero, S.A. Dassie, R.H. Acosta, *Journal of Electroanalytical Chemistry*, 750, (2015), 100-106.
- [25] C. Du, Q. Tan, G. Yin, J. Zhang, Chapter 5 - Rotating Disk Electrode Method, in: Xing W., Yin G., Zhang J., *Rotating Electrode Methods and Oxygen Reduction Electrocatalysts*, Elsevier, Amsterdam, 2014, pp. 171-198.
- [26] *Modulated Speed Rotator, User Manual*, Rotating disk electrode, Pine Research Instrumentation, (2012), 101-103.
- [27] K. Ke, T. Hatanaka, Y. Morimoto, *Electrochimica Acta*, 56, (2011), 2098-2104.
- [28] K.L. Hsueh, D.T. Chin, S. Srinivasan, *Journal of Electroanalytical Chemistry and Interfacial Electrochemistry*, 153, (1983), 79-95.
- [29] R. Zhou, Y. Zheng, M. Jaroniec, S. Qiao, *ACS Catalysis*, 6, (2016), 4720-4728.
- [30] Y. Wang, D. Zhang, H. Liu, *Journal of Power Sources*, 195, (2010), 3135-3139.
- [31] U.A. Paulus, T.J. Schmidt, H.A. Gasteiger, R.J. Behm, *Journal of Electroanalytical Chemistry*, 495, (2001), 134-145.
- [32] G. Hübschen, I. Altpeter, R. Tschuncky, H. Herrmann, Chapter 4 - X-ray diffraction (XRD) techniques for materials characterization, in: G. Hübschen, I. Altpeter, R. Tschuncky, H. Herrmann, *Materials Characterization Using Nondestructive Evaluation (NDE) Methods*, Woodhead Publishing, 2016, pp. 81-124.
- [33] D.G. Lamas, M. de Oliveira Neto, G. Kellermann, A.F. Craievich, Chapter 5 - X-Ray Diffraction and Scattering by Nanomaterials, in: O. J. Novais de Oliveira, M. Ferreira, F. de Lima Leite, A. L. Da Róz, *Nanocharacterization Techniques*, William Andrew Publishing, 2017, pp. 111-182.

- [34] Y. Leng, *Materials Characterization: Introduction to Microscopic and Spectroscopic Methods*, John Wiley & Sons, Singapore, 2008, pp. 49-51.
- [35] L. Weng, *Applied Catalysis A: General*, 474, (2014), 203-210.
- [36] T. Taniike, P. Chammingkwan, V.Q. Thang, T. Funako, M. Terano, *Applied Catalysis A: General*, 437, (2012), 24-27.
- [37] K.C. Kim, T. Yoon, Y. Bae, *Microporous and Mesoporous Materials*, 224, (2016), 294-301.
- [38] M. Naderi, Chapter 14 - Surface Area: Brunauer–Emmett–Teller (BET), in: S. Tarleton, *Progress in Filtration and Separation*, Academic Press, Oxford, 2015, pp. 585-608.
- [39] A. Legras, A. Kondor, M.T. Heitzmann, R.W. Truss, *Journal of Chromatography A*, 1425, (2015), 273-279.
- [40] M. Bohnet, *Mechanische Verfahrenstechnik*, 1. Auflage, WILEY-VCH Verlag, Weinheim, 2004, p. 64.
- [41] C. Levoguer, *Metal Powder Report*, 68, (2013), 15-18.
- [42] L. Pan, B. Ge, F. Zhang, *Journal of Quantitative Spectroscopy and Radiative Transfer*, 199, (2017), 20-25.
- [43] M. de Assumpção Pereira-da-Silva, F.A. Ferri, Chapter 1 - Scanning Electron Microscopy, in: O. J. Novais de Oliveira, M. Ferreira, F. de Lima Leite, A. L. Da Róz, *Nanocharacterization Techniques*, William Andrew Publishing, 2017, pp. 1-35.
- [44] B.J. Inkson, Chapter 2 - Scanning electron microscopy (SEM) and transmission electron microscopy (TEM) for materials characterization, in: G. Hübschen, I. Altpeter, R. Tschuncky, H. Herrmann, *Materials Characterization Using Nondestructive Evaluation (NDE) Methods*, Woodhead Publishing, 2016, pp. 17-43.
- [45] S. Henning, R. Adhikari, Chapter 1 - Scanning Electron Microscopy, ESEM, and X-ray Microanalysis, in: T. Sabu, T. Raju, Z. K. Ajesh, M. K. Raghvendra, *Microscopy Methods in Nanomaterials Characterization*, Elsevier, 2017, pp. 1-30.
- [46] K.E. Sickafus, J.M. Wills, N.W. Grimes, *Journal of the American Ceramic Society*, 82, (1999), 3279-3292.
- [47] M. Binnewies, M. Finze, M. Jäckel, P. Schmidt, H. Willner, G. Rayner-Canham, *Allgemeine und Anorganische Chemie*, 3. Auflage, Springer, Berlin, Heidelberg, 2016, pp. 470, 726.
- [48] S.Y. Tsai, C.T. Ni, K.Z. Fung, *Ceramics International*, 43, (2017), S460-S463.
- [49] created from data of ICSD-FIZ Karlsruhe with VESTA.

- [50] T. Sönmez, S.J. Thompson, S.W.T. Price, D. Pletcher, A.E. Russell, *Journal of The Electrochemical Society*, 163, (2016), H884-H890.
- [51] A.C. Tavares, M.A.M. Cartaxo, M.I. da Silva Pereira, F.M. Costa, *Journal of Solid State Electrochemistry*, 5, (2001), 57-67.
- [52] Pine Research Instrumentation Store, available at: <https://www.pineresearch.com/shop/products/electrodes/rrde/classic-ptfe-rrde/e6r1-ptfe/#documentation>, accessed 30.09.2017.
- [53] ICSD Datenbank des FIZ Karlsruhe, available at: <https://icsd.fiz-karlsruhe.de/viscalc/jsp/sliderDetailed.action>, accessed 19.04.2017.
- [54] P. Scherrer, *Nachrichten der Gesellschaft für Wissenschaft Göttingen*, 2, (1918), 96-100.
- [55] H. P. Klug, E. L. Alexander, *X-Ray Diffraction Procedures*, 2nd edition, Wiley (Interscience), New York, 1974, p. 996.
- [56] B. Chi, J. Li, Y. Han, Y. Chen, *International Journal of Hydrogen Energy*, 29, (2004), 605-610.
- [57] M. Stieß, *Mechanische Verfahrenstechnik - Partikeltechnologie 1*, 3. Auflage, Springer, Berlin, Heidelberg, 2009.

7 Chemicals

Table 7: List of used chemicals.

Chemical	Supplier	Details
Choline acetate	IOLITEC Ionic Liquids Technologies GmbH	IL-0322-HP 98%
Choline bicarbonate	SIGMA	C7519-500ML ~80% in H ₂ O CAS: 78-73-9
Choline hydroxide	Alfa Aesar	B24443 46% w/w aq.soln CAS: 123-41-1
Cobalt(II) nitrate hexahydrate	SIGMA - ALDRICH	239267-500G , ACS reagent, ≥ 98%, CAS: 10026-22-9
Nafion® perfluorinated resin, aqueous dispersion	ALDRICH	527114-25ML, 10w% in H ₂ O, CAS: 31175-20-9
Nickel(II) nitrate hexahydrate	ALDRICH Chemistry	23874-500G , 99.999%, trace metal basis CAS: 13478-00-7
Potassium hydroxide	VWR Chemicals	26669.290 86.7 % CAS: 1310-58-3
Sodium hydroxide	VWR Chemicals	28244.295 99.2 % CAS: 1310-73-2
Sulfuric acid	Fisher Scientific	> 95% CAS: 7664-93-9

8 List of symbols and abbreviations

N	collection efficiency	
i	current	μA
j	current density	mA cm^{-2}
j_L	limiting current density	mA cm^{-2}
E	potential	V
ω	rotation rate	rpm
v	scan rate	mV s^{-1}

Ag/AgCl	Silver/ silver chloride electrode
BET	Brunauer-Emmett-Teller
CE	Counter electrode
C-CO ₃	Choline carbonate
C-OAc	Choline acetate
C-SO ₄	Choline sulphate
CV	Cyclic voltammogram
deion. H ₂ O	Deionised water
e ⁻	Electron
GC	Glassy carbon
GDE	Gas diffusion electrode
GDL	Gas diffusion layer
Hg/HgO	Mercury/ mercury oxide electrode
IR	Infrared
OER	Oxygen evolution reaction
ORR	Oxygen reduction reaction
PSD	Particle size distribution
RDE	Rotating disc electrode
RE	Reference electrode
RFB(s)	Redox flow battery(ies)
RRDE	Rotating ring-disc electrode
RT	Room temperature
SEM	Scanning electron microscopy

SHE	Standard hydrogen electrode
SSA	Specific surface area
WE	Working electrode
XRD	X-ray diffraction

9 List of figures

Figure 1: Principle design of a redox flow battery [8].	3
Figure 2: A schematic diagram of a zinc-air redox flow battery [6].	5
Figure 3: Illustration of the troubles of the zinc electrode: a) dendrite formation, b) shape change, c) passivation and, d) hydrogen evolution [5].	6
Figure 4: Schematic of four different possibilities of the adsorption of O ₂ (blue) on catalyst surfaces: a) on-top end-on, b) bridge end-on, c) bridge side-on one site, and d) bridge side-on two sites [17].	8
Figure 5: Schematic of the potential course of a CV [19].	10
Figure 6: Schematic of potential course of LSV [20].	10
Figure 7: Illustration of a cyclic voltammogram [21].	11
Figure 8: Illustration of a cyclic voltammogram of an irreversible (graph A) and a quasi-reversible (graph B) redox process [21].	11
Figure 9: Schematic of the RDE [22].	12
Figure 10: Voltammograms of ORR of a Pt disk electrode in O ₂ -saturated 0.5 M H ₂ SO ₄ at 30°C with v of 5 mV s ⁻¹ and different ω [25].	14
Figure 11: Koutecky-Levich plot of the voltammograms (Figure 9) at different electrode potentials [25].	14
Figure 12: Schematic of XRD patterns of an amorphous (left) and a crystalline (right) solid [33].	17
Figure 13: Schematic of the diffraction of X-ray beam on the crystallographic planes under Bragg's law condition [34].	18
Figure 14: Schematic of a diffraction peak with a few parameters [32].	19
Figure 15: Schematic diagrams of the adsorption isotherms type II and IV [38].	20
Figure 16: Schematic of the measuring unit of a laser diffractometer with a) laser, b) optical lens, c) sample cell, d) scattered beam, and e) detector array [42].	22
Figure 17: Schematic of the compounds of a scanning electron microscope [44].	23
Figure 18: Schematic of origin and interaction volume of the different signals during SEM measurements [45].	24
Figure 19: Schematic of ions (pink: Co, green: Ni and grey: O) of a NiCo ₂ O ₄ spinel arranged in a cubic unit cell [49].	25
Figure 20: Schematic of tetrahedral (orange) and octahedral (blue) sites and ions (pink: Co, green: Ni and grey: O) of a NiCo ₂ O ₄ spinel in a cubic unit cell [49].	25
Figure 21: The spinel P8 after calcination.	26

Figure 22: Solution after metal salt addition.....	27
Figure 23: Arrangement of the filtration equipment.....	27
Figure 24: Structure of the choline cation.	28
Figure 25: Rotating ring-disc electrode with Pt ring and glassy carbon disc.	31
Figure 26: Measuring unit of RRDE experiments with the RE, CE, RRDE, gas inlet and measuring cell.	32
Figure 27: Comparison of the cyclic voltammograms of the different NiCo ₂ O ₄ spinels in 8 M KOH at RT with ν of 10 mV s ⁻¹	35
Figure 28: Cyclic voltammograms of P7 (350°C/NO ₃ /s) in 8 M KOH at RT with different scan rates.	36
Figure 29: Cyclic voltammograms of P8 (300°C/NO ₃ /s) in 8 M KOH at RT with different scan rates.	36
Figure 30: Cyclic voltammograms of P9 (375°C/OH/s) in 8 M KOH at RT with different scan rates.	36
Figure 31: Plot of peak current density vs. scan rate of P7 (350°C/NO ₃ /s), P8 (300°C/NO ₃ /s) and P9 (375°C/OH/s) in 8 M KOH at RT.....	37
Figure 32: Cyclic voltammograms of the 1 st and 10 th cycle of P2_BK (375 /OH/s) in 8 M KOH at RT with ν of 10 mV s ⁻¹	38
Figure 33: Cyclic voltammograms of the 1 st and 10 th cycle of P3 (300°C/NO ₃ /u) in 8 M KOH at RT with ν of 10 mV s ⁻¹	38
Figure 34: Cyclic voltammograms of the 1 st and 10 th cycle of P4 (350°C/NO ₃ /u) in 8 M KOH at RT with ν of 10 mV s ⁻¹	38
Figure 35: Cyclic voltammograms of the 1 st and 10 th cycle of P7 (350°C/NO ₃ /s) in 8 M KOH at RT with ν of 10 mV s ⁻¹	38
Figure 36: Cyclic voltammograms of the 1 st and 10 th cycle of P8 (300°C/NO ₃ /s) in 8 M KOH at RT with ν of 10 mV s ⁻¹	39
Figure 37: Cyclic voltammograms of the 1 st and 10 th cycle of P9 (375°C/OH/s) in 8 M KOH at RT with ν of 10 mV s ⁻¹	39
Figure 38: Comparison of the cyclic voltammograms of P7 (350°C/NO ₃ /s) in choline acetate, - sulphate and - carbonate at RT with ν of 10 mV s ⁻¹	40
Figure 39: Comparison of the cyclic voltammograms of P7 (350°C/NO ₃ /s) in choline acetate, - sulphate and - carbonate at RT with ν of 10 mV s ⁻¹ in another scale.....	40
Figure 40: Voltammograms for ORR of P2_BK (375°C/OH/s) in 8 M KOH at RT with ν of 5 mV s ⁻¹ and different ω	41

Figure 41: Voltammograms for ORR of P3 (300°C/NO ₃ /u) in 8 M KOH at RT with ν of 5 mV s ⁻¹ and different ω	42
Figure 42: Voltammograms for ORR of P8 (300°C/NO ₃ /s) in 8 M KOH at RT with ν of 5 mV s ⁻¹ and different ω	42
Figure 43: Voltammograms for ORR of P9 (375°C/OH/s) in 8 M KOH at RT with ν of 5 mV s ⁻¹ and different ω	43
Figure 44: Comparison of the voltammograms of ORR of the different NiCo ₂ O ₄ spinels in 8 M KOH at RT with ν of 5 mV s ⁻¹ and ω of 900 rpm.	44
Figure 45: Comparison of the voltammograms of ORR of the different NiCo ₂ O ₄ spinels in 8 M KOH at RT with ν of 5 mV s ⁻¹ and ω of 1600 rpm.	44
Figure 46: Comparison of the voltammograms of ORR of the different NiCo ₂ O ₄ spinels in 8 M KOH at RT with ν of 5 mV s ⁻¹ and ω of 2300 rpm.	45
Figure 47: Comparison of the voltammograms of OER of the different NiCo ₂ O ₄ spinels in 8 M KOH at RT with ν of 5 mV s ⁻¹ and ω of 400 rpm.	46
Figure 48: Koutecky-Levich plot of P2_BK (375°C/OH/s) in 8 M KOH at RT.....	47
Figure 49: Koutecky-Levich plot of P8 (300°C/NO ₃ /s) in 8 M KOH at RT.	47
Figure 50: Koutecky-Levich plot of P9 (375°C/OH/s) in 8 M KOH at RT.	47
Figure 51: Comparison of the Koutecky-Levich plot of, P2_BK (375°C/OH/s), P7 (350°C/NO ₃ /s), P8 (300°C/NO ₃ /s) and P9 (375°C/OH/s) in 8 M KOH at RT.....	47
Figure 52: Comparison of the voltammograms of ORR of P7 (350°C/NO ₃ /s) and the bare RDE in choline acetate, - sulphate and - carbonate at RT with ν of 5 mV s ⁻¹ and ω of 900 rpm.....	48
Figure 53: Comparison of the voltammograms of ORR of P7 (350°C/NO ₃ /s) and the bare RDE in choline acetate, - sulphate and - carbonate at RT with ν of 5 mV s ⁻¹ and ω of 900 rpm in another scale.	49
Figure 54: Comparison of the voltammograms of OER of P7 (350°C/NO ₃ /s) in choline acetate, - sulphate and - carbonate at RT with ν of 5 mV s ⁻¹ and ω of 400 rpm.	50
Figure 55: Comparison of the voltammograms of OER of P7 (350°C/NO ₃ /s) in choline acetate, - sulphate and - carbonate at RT with ν of 5 mV s ⁻¹ and ω of 400 rpm in another scale.	50
Figure 56: CV of the ferrocyanide/ferricyanide redox-pair in 0.1 M KCl at RT with ν of 10 mV s ⁻¹	52
Figure 57: Voltammograms of the ring and disc of the ferrocyanide/ferricyanide system in 0.1 M KCl at RT with ν of 10 mV s ⁻¹ and different ω	52

Figure 58: RRDE voltammograms (ring) of P7 (350°C/NO ₃ /s) in 8 M KOH at RT with v of 5 mV s ⁻¹ and different ω	54
Figure 59: RRDE voltammograms (disc) of P7 (350°C/NO ₃ /s) in 8 M KOH at RT with v of 5 mV s ⁻¹ and different ω	54
Figure 60: RRDE voltammograms (ring) of P7 (350°C/NO ₃ /s) in C-OAc at RT with v of 5 mV·s ⁻¹ and different ω	56
Figure 61: RRDE voltammograms (disc) of P7 (350°C/NO ₃ /s) in C-OAc at RT with v of 5 mV s ⁻¹ and different ω	56
Figure 62: XRD pattern of the spinel P2_BK (375°C/OH/s).....	58
Figure 63: XRD pattern of the spinel P9 (375°C/OH/s).....	58
Figure 64: XRD pattern of the spinel P3 (300°C/NO ₃ /u).....	58
Figure 65: XRD pattern of the spinel P8 (300°C/NO ₃ /s).....	58
Figure 66: XRD pattern of the spinel P4 (350°C/NO ₃ /u).....	59
Figure 67: XRD pattern of the spinel P7 (350°C/NO ₃ /s).....	59
Figure 68: Particle size distribution of P2_BK (375°C/OH/s).....	61
Figure 69: Particle size distribution of P3 (300°C/NO ₃ /u).....	62
Figure 70: Particle size distribution of P4 (350°C/NO ₃ /u).....	62
Figure 71: Particle size distribution of P7 (350°C/NO ₃ /s).....	63
Figure 72: Particle size distribution of P8 (300°C/NO ₃ /s).....	63
Figure 73: Particle size distribution of P9 (375°C/OH/s).....	64
Figure 74: SEM micrograph of P2_BK (375°C/OH/s) with 5000x magnification.	64
Figure 75: SEM micrograph of P3 (300°C/NO ₃ /u) with 5000x magnification.	64
Figure 76: SEM micrograph of P4 (350°C/NO ₃ /u) with 5000x magnification.	65
Figure 77: SEM micrograph of P7 (350°C/NO ₃ /s) with 5000x magnification.....	65
Figure 78: SEM micrograph of P8 (300°C/NO ₃ /s) with 5000x magnification.....	65
Figure 79: SEM micrograph of P9 (375°C/OH/s) with 5000x magnification.	65

10 List of tables

Table 1: Preparation details of the catalysts.	28
Table 2: Values for the determination of the collection efficiency of the RRDE.	51
Table 3: Percentage of formed peroxide and number of transferred electrons of P7 in 8 M KOH.	53
Table 4: Values of formed peroxide and number of electrons of P7 in C-OAc.	55
Table 5: Lattice constant and crystallite size of the NiCo ₂ O ₄ spinels.	57
Table 6: BET area and mean particle size of the NiCo ₂ O ₄ spinels.	60
Table 7: List of used chemicals.	73